Master's thesis

NTNU
Norwegian University of Science and Technology
Faculty of Information Technology and Electrical Engineering
Department of Electric Power Engineering

Eivind Krakk

Back-to-Back Based Voltage Control of an Isolated Grid Supplied by a Hydro Turbine Driven Induction Generator

Master's thesis in Energy and Environmental Engineering

Supervisor: Jonas Kristiansen Nøland

June 2020

NTNU
Norwegian University of Science and Technology

Abstract

Today's society is totally dependent on supply of electric power. Interconnected transmission grids are widely available all over the world. However, in rural areas without any existing grid infrastructure, an isolated system can be an option for power supply. This is especially relevant for developing countries, where the availability of grid infrastructure is more limited. Utilization of a local renewable energy resource, can by itself be another motivation for applying an isolated power system.

The topic of this Master's Thesis has been to utilize common available products and design a proper control system for an isolated hydro power system. The squirrel cage induction machines are the most commonly used electric machine for drives applications worldwide and is thus easily available in all power ranges. Their simple construction makes them cheap compared to alternatives such as the synchronous machine at the same power rating. Maximum load demand of the system is set to be 1.5 kW in this analysis. The investigation strives to find the best solution with respect to load voltage quality in the case of using a squirrel cage induction machine rather than the most cost effective solution. Thus, a back-to-back topology is used to decouple the mechanical speed from the load frequency. At the load side of the converter, a tuned passive LCL-filter is used to filter out higher order harmonic components.

The system containing the induction machine, back-to-back converter and the passive LCL-filter, should be able to deliver a good voltage quality. The resulting load voltage should satisfy the Norwegian quality requirements for low voltage grids, given in *Forskrift om leveringskvalitet i kraftsystemet*. The requirements are 230 V ± 3.0% in RMS-value and < 5.0% total harmonic distortion (THD) at 50 Hz. Even though these requirements are very strict, they are chosen as a basis for comparing the voltage quality.

The operation of the induction generator is controlled to keep the current and power within the rated limits. The investigated control methods for a squirrel cage induction machine are V/f-control (scalar method) and indirect vector control (IVC). These schemes have been build from scratch, and their performance is tested in Simulink. In addition, the Simulink model contains the control systems of the hydro turbine governor and the load voltage controller.

A per unit model of a squirrel cage induction machine is build, based on a set of lab-measurements. This model is scaled to fit five different power ratings between 1.5 kW and 11 kW. The nominal current is increasing with the power rating, and hence the machine can produce a larger electromagnetic torque to handle sudden load steps. The influence of total moment of inertia at the shaft is also investigated. The effect of adding a flywheel to increase the size of allowed load steps (disturbances) while keeping stable system operation, is also investigated. It is recommended to use a generator with a rated power of 2.2 kW or 3.0 kW, preferably with an additional flywheel.

Results from five different simulation tests have highlighted several characteristics of the system and its control. The main conclusions are: Larger moment of inertia allows application of larger load steps (i.e. the increased moment of inertia achieves better stability). With a proper LCL-filter design and assuming the DC-link voltage in the converter is maintained at its reference, the simulations produced a very good load voltage quality. The THD is in the range of 1 % and phase-to-neutral RMS voltage is 230 V (± 0.15% voltage deviation). Thus, operating the system in a way that maintains the DC-link voltage, makes the system able to achieve a very good voltage quality at the load side.

Samandrag

Dagens samfunn er heilt avhengig av elektrisitetsforsyning. Samankopla transmisjonsnett er lett tilgjengelege over heile verda. Likevel, i rurale områder utan nokon form for eksisterande nettinfrastruktur, kan eit isolert nett vere ei moglegheit for elforsyning. Dette gjeld særleg i utviklingsland der eksisterande nettinfrastruktur gjerne er avgrensa. Utnytting av ei lokal fornybar energikjelde kan i seg sjølv vere ein annan motivasjon for å bygge eit isolert nett.

Utfordringa som denne masteroppgåva tar tak i er å designe eit kontrollsystem for eit isolert nett som er drive av ein induksjonsmaskin med kortslutningsrotor. Vasskraft er primærkjelda til dette systemet. Induksjonsmaskinen er svært mykje brukt som elektrisk motordrift til ulike føremål over heile verda. Den er lett tilgjengeleg i alle effektytingar. Maskinen sin enkle, men likevel robuste konstruksjon, gjer den billig samanlikna med alternativ slik som synkronmaskinen ved same effektyting. Maksimal last for systemet er sett til å vere 1.5 kW i denne analysen. Det er forsøkt å finne den løysinga med ein induksjonsgenerator som gir best spenningskvalitet på lastsida, framfor å finne den mest kostnadseffektive metoden. Dermed er ein back-to-back omformar topologi brukt til å kople det mekaniske generatorturtalet og -frekvensen frå den elektriske frekvensen på lastsida. Mellom lasta og omformaren er det brukt eit passivt LCL-filter til å filtrere ut høgare ordens harmoniske komponentar.

Hensikten med systemet som inneheld induksjonsgeneratoren, back-to-back omformaren og det passive LCL-filteret er å vere i stand til å levere god spenningskvalitet. Den resulterande lastspenninga skal tilfredsstille dei norske krava til spenningskvalitet i lågspente nett gjeve i *Forskrift om leveringskvalitet i kraftsystemet*. Krava er 230 V ± 3.0 % i RMS verdi og < 5.0 % total harmonisk forvrenging (THD) ved 50 Hz. Sjølv om desse krava er veldig strenge er dei valde som eit samanlikningsgrunnlag for spenningskvalitet.

Drifta av induksjonsgeneratoren er regulert til å halde straumen og effekten innanfor dei nominelle grensene. Dei kontrollmetodane for induksjonsmaskin (med kortslutta rotor) som er undersøkte her er V/f-kontroll (skalarmetoden) og indirekte vektorkontroll (IVC). Desse kontrollordningane har vorte bygde opp frå botn av og testa i Simulink. I tillegg inneheld Simulinkmodellen reguleringsystem for vassturbinen og lastside omformaren.

Ein einingsmodell (per unit) av ein induksjonsmaskin er laga, basert på eit sett av laboratoriemålingar på ein reell 1.5 kW induksjonsmaskin. Denne modellen er skalert til fem ulike effektytingar mellom 1.5 kW og 11 kW. Den nominelle straumen aukar med effektytinga på maskina. Dermed kan maskinen produsere større elektromagnetisk moment til å handtere plutselege laststeg. Innverknaden av totalt tregleiksmoment på akslingen er også undersøkt. Verknaden av å kople på eit svinghjul for å auke den tillate storleiken på laststega er også undersøkt. Basert på simuleringane er det anbefalt å bruke ein generator med nominell yting på 2.2 kW eller 3.0 kW, helst med eit ekstra svinghjul.

Resultata frå fem ulike simuleringstestar har vist fleire eigenskapar ved systemet og reguleringa av det. Hovudkonklusjonane er: Større tregleiksmoment vil tillate større laststeg i systemet, og dermed er betre stabilitet oppnådd. Ved å tilpasse LCL-filterdesignet til nominell lasteffekt og holde likestraumspenninga i omformaren konstant på referenasen sin, viser simuleringane at ei veldig god spenningskvalitet ved lasten er oppnådd. THD er rundt 1% og fase-nøytral RMS-spenninga er målt til 230 V (± 0.15% spenningsavvik). Dermed, ved ei drift av systemet som opprettheld likestraumspenninga, er systemet i stand til å levere ei høg spenningskvalitet til lasta.

Preface

The spring semester of 2020 has been an extraordinary semester all over the world. After the outbreak of covid-19 in the middle of March, students and employees at NTNU and other universities had to work from home for a while, and consequently the student access to campuses and laboratories has been temporary closed. For my work on this Master's Thesis, the extraordinary circumstances due to covid-19 have changed the objective of work from achieve a physical laboratory set-up containing an induction generator supplying an isolated load, to be a more theoretical and a pure simulation task. Initially the main purpose was to develop a proper control system in FPGA that could have been tested on the back-to-back converter arrangement in the setup. Unfortunately the circumstances have not allowed this work to be done. Instead of using FPGA to make the control script, a detailed model of the isolated system and its control system has been made in MATLAB/Simulink and used to study the details of the control system behavior.

The new guidelines has changed the objective of the Master Thesis from a task of programming to a pure simulation task which consider all parts of the system. Furthermore the power rating of the generator, total moment of inertia and different control approaches of the generator are considered. Some of the laboratory results from my Project Work [3], Fall 2019 have been used as a basis to build the induction machine model in the Simulink model.

Eivind Krakk
June 2020 - Trondheim

Acknowledgments

I want acknowledge my supervisor and associate professor at NTNU, Jonas Kristiansen Nøland for his contribution with and his feedback on my work.

A great acknowledgment is given to my co-supervisor and docent emeritus at NTNU, Trond Leiv Toftevaag, whose had the idea of studying the control systems for an isolated operated induction generator. He has been my closest collaborator during this work and lined up for digital meetings and feedback sessions throughout this extraordinary semester. His professional guidance and help have been valuable.

I will also acknowledge professor Kjetil Uhlen for sharing his expertise on the design and tuning of control system.

I have missed fellow students during the period of working from home. The daily value of joint breaks with professional and social discussions with the fellow students are among what I have missed. The laboratory work in cooperation with fellow student Ragnhild P. Mo during the project work in fall semester 2019, was an exciting and mutually educational process.

From my heart I will give a great honor to Trine for her unconditional love and support to me. She has helped me to stay motivated during the work of my Master Thesis.

Table of Contents

List of Figures

List of Tables

Abbreviations

SCIM Squirrel Cage Induction Machine

SCIG Squirrel Cage Induction Generator

IM Induction Machine

DFIG Doubly Feed Induction Generator

SG Synchronous Generator

PM Permanent Magnet

DC Direct Current

AC Alternating Current

VSC Voltage Source Converter

VSI Voltage Source Inverter

2L-3Φ Two level, three phase

IGBT Insulated-Gate Bipolar Transistor

PWM Pulse Width Modulation

S-PWM Sinusoidal Pulse Width Modulation

SV-PWM Space Vector Pulse Width Modulation

LCL Inductor-Capacitor-Inductor

V/f Voltage/Frequency Control

FOC Field Oriented Control

IVC Indirect Vector Control

DVC Direct Vector Control

DTC Direct Torque Control

THD Total Harmonic Distortion

RMS Root Mean Square

1 Introduction

1.1 Background

Today, our society is totally dependent on electric power supply. Traditionally, most consumers of electric power such as households and technical or industrial plants get their electric supply from the local distribution grid that is interconnected to the national transmission grid. This is still the main picture of electric power supply. However, the use of self-standing isolated grids can be useful for certain applications as a supplement to the existing interconnected grid infrastructure:

- Areas without existing grid infrastructure
- Self-supply mentality
- Utilization of a local renewable resource

In the developing countries today, many people are living their lives in rural areas far away from existing grid infrastructure. For many of those cases, grid connection is not applicable due to too large investment costs. An isolated grid can be a better solution. When building an isolated system at such sites, the most important considerations are: Keeping the system simple to operate, lowering the investments costs while maintaining high voltage quality and reliability of the system (it might have to be lower than what used in interconnected grids).

Self-supply mentality is a growing mentality in our society today. Several pilot projects have been done where relatively large consumers such as farmers (or just single households) want to be supplied from their own power plant. Many of those have an overall goal of being independent of supply from the grid operator.

Utilization of a local renewable resource has been an extra motivation for many of these pilot projects on being self-supplied. Hydro power (from a local river), wind power and photovoltaics are among the options for power generation. Some of those renewable resources are usually available when building an isolated grid in developing countries.

Knowledge of system behavior and whether it is fragile at certain operation conditions is important when designing an isolated grid. Several system configurations and topologies exist. This Master's Thesis proposes and evaluates a system containing a hydro driven squirrel cage induction generator that supplies an isolated load demand at up to 1.5 kW. A back-to-back converter is used to decouple the load frequency from the mechanical shaft speed. The intention is to keep the system performance in terms of high quality of load side voltage while using an induction generator rather than make a cost effective system.

1.2 Issue and Objective

This Master's Thesis is motivated and inspired by the Master's Theses [1, 2] at Department of Electric Power Engineering at NTNU spring semesters 2019 and 2016 working on isolated operation of squirrel cage induction generators (SCIG). Self excitated induction generator (SEIG) is another commonly used term of SCIG. It is also a continuation of the Project Work [3] of fall 2019. All of those works are considering the use of a hydro driven squirrel induction generator that supplies clean hydro power to an isolated load. The squirrel cage induction machine is chosen because of its robust and simple construction that makes it cheap, relative to the power rating. Further, it has no slip rings and thus no additional circuit for field current. This have made the SCIM widely used in industrial motor and drives applications worldwide. The widespread usage makes it available in all power ranges. Those benefits of the generator are favorable when designing an isolated system at a remote area.

The issue or objective with this Master's Thesis has been to develop control systems for the isolated induction generator system driven by hydro power. Achieving high voltage quality at the load side is emphasized, rather than pure cost reduction. A back-to-back converter topology has been used with two independently controllable voltage source converters (VSCs), one at each side of the DC-link. The control of the generator side VSC has been given most attention, however the hydraulic turbine governor performance and load side performance is also developed and discussed. The impact from other characteristics such as generator power rating and total moment of inertia are included in the study. The maximum system load demand is set to 1.5 kW. To do this, laboratory measurements from the project work [3] have been used as a basis to create a scalable model of the induction machine. Figure 1.1 shows the components associated with the control system investigated.

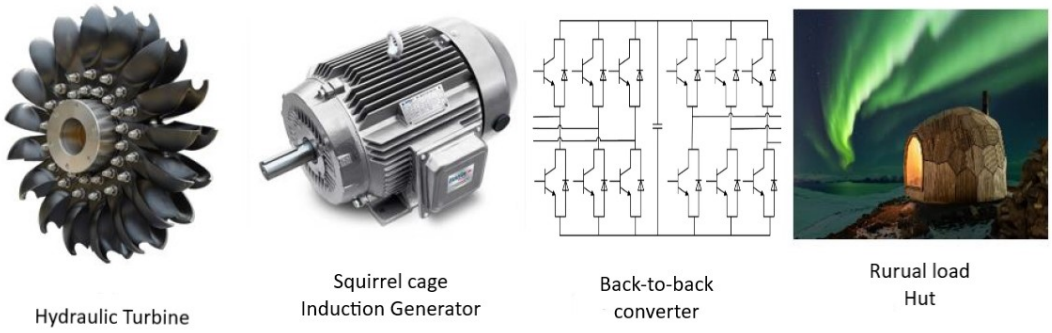

Figure 1.1: Overview of main physical components investigated. It is a hydraulic turbine, an induction generator, a back-to-back converter and a rural load, depicted here as a hut with light.

1.3 Scope of Work

A literature research was initially deducted when starting to work. Mainly, it focused on control techniques of induction machines, but literature discussing filter and load controller performance, in addition to hydraulic governor have also been useful. A Simulink model of the whole isolated system have been made. In addition Simulink models containing only parts of the system have been made and are considered when only parts of the system are investigated. The size (nominal power) of the induction generator are scaled to six sizes between 1.5 kW and 15 kW indicated by #IM1, #IM2, #IM3,#IM4 and #IM5. The generator size and all parameters and constants used in the Simulink model is initialized by a nested MATLAB-script. The script needs to run before the Simulink simulation is run. The control systems have been build from scratch and are based on the literature. Five simulations tests have been done to investigate different characteristics of the system and its behavior.

1.4 Simulator

The work presented in this Master's Thesis is based on a Simulink model of an isolated system with a rated of 1.5 kW supplied by a hydro driven squirrel cage induction generator. The generator is modeled by the *Asynchronous Machine block* found in Simspace. The functionalities of the VSCs are achieved by using universal bridge with IGBT/diode as power switching device. The control system structures (i.e. governor, generator controller and load controller) are included in the Simulink model based equations and relations describing their basic functionality.

1.5 Limitations

The task has been limited to developing a simulation model that will give a satisfying system performance. The Norwegian requirements for low voltage grid in *Forskrift om leveringskvalitet i kraftsystemet* [4] are very strict and are used to get an indication of how well the system behaves. In some tests only parts of the system is investigated and assumptions are made and pointed out. In the final simulation test (Test 5) all parts of the system are interconnected and the system performance are tested.

Some important notes are among others: The turbine power is not varied but kept at 2.2 kW. It is modeled by the linear hydraulic transfer function. Further, tuning of several controller parameters could improve the performance of the system. The control systems have limitations in the control loop both in achieving stability and protect fragile components from different kinds of overloading that can be damaging (i.e over-current or over-pressure).

1.6 Structure of Content

In chapter 2 the characteristics of the hydraulic turbine model and the hydraulic governor are discussed. Chapter 3 introduces the characteristics of the induction machine that are most relevant to the control systems. Further, in chapter 4 the converter behavior and considerations of the DC-link are discussed. Methods for gate signal generation for the 2L-3Φ VSCs are the topic in chapter 5. Chapter 6 proposes the passive filter design. The load model that varies the system load demand is explained in chapter 7. The control techniques of induction machines and their background are introduced in chapter 8. While chapter 9 explains the scalar control scheme of induction generators. In chapter 10 vector control of induction machines are discussed and the control scheme of indirect vector control is explained. The structure of the load voltage controller is discussed in chapter 11. The tuning process of the components and parameters in the physical system and the control system is discussed in chapter 12. Chapter 13 presents the simulation results from five different tests. Characteristics of generator rating, shaft inertia, scalar control vs. vector control are among what was investigated. Chapter 14 summarizes the most important findings in the simulations and draws some conclusions and recommendations based on the findings. Finally, some suggestions for further work on control of isolated hydro driven induction generators are presented.

2 Hydraulic Turbine and Governor

A hydraulic turbine converts potential energy and/or kinetic energy in water into rotating mechanical energy. The rotating mechanical energy received from hydraulic turbines have historically been used for several purposes such as sawmills and grain mills. However, in today's society, hydro turbines are now almost exclusively used in hydro electric power production.

2.1 Impulse and Reaction Turbines

Hydraulic turbines can generally be assigned to one of two categories [5, 6]:

- Impulse turbine
- Reaction turbine

The most common impulse turbine is the Pelton wheel. However, there also exist other types of impulse turbines designed for special applications. An example is the turgo turbine.

Impulse turbines have one or more fixed nozzles located in the periphery of the wheel. The nozzles convert the potential energy in pressurized water to high velocity water jets. The kinetic energy in the jet is applied to the spoon shaped buckets on the wheel. An important note regarding the classification of impulse turbines is that the pressure drop occurs in the nozzles and not on the runner (turbine) itself. Thus, the runner is always operating at atmospheric pressure. The spoon shaped buckets are equipped with a ridge that splits the incoming water jets into two equal portions at the Pelton wheel. The portions of water follow the inner surface of the bucket and is deflected about 160° with respect to the incoming angle. This makes a lot of momentum changes on the wheel which provides the mechanical torque on the shaft. According to [7], the discussion of characteristics and performance of turgo turbines is often included in the discussion of Pelton wheel. While Pelton wheels mostly are used for high hydraulic heads (> 300 m) and with a lower flow rate, turgo turbines are able to handle a significantly higher flow rate. This makes them more suitable for lower water heads and thus suitable for pico-hydro power plants. The maintenance costs associated with impulse turbines are low and their reliability and efficiency are high ($\eta > 90\%$). Figure 2.1 shows a schematic impulse turbine with a nozzle. The splitter ridge at the bucket belongs to the Pelton design. Turgo buckets are differently shaped to handle a larger hydraulic flow. The turbine used as a basis for the model and simulation is a turgo turbine equipped with one single nozzle [7].

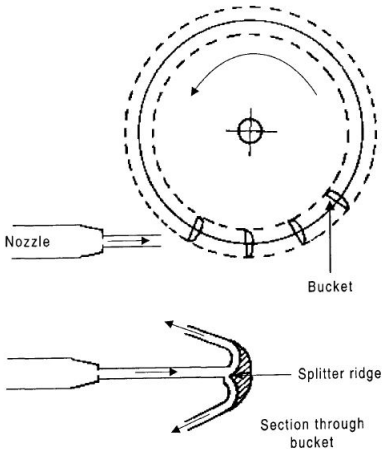

Figure 2.1: Impulse turbine and its nozzle. Figure 2.2 in [6]

Reaction turbines are characterized by a pressure drop which occurs across the turbines in the direction of water flow. Thus, they are supplied with both potential and kinetic energy from the water flow. Based on the predominant direction (radial or axial) of water inlet flow with respect to the axis of rotation, mainly three categories of reaction turbines for hydro power exists [6]:

- Francis turbine
- Kaplan/Propeller turbine
- Pump As Tubrine (PAT)

A Francis turbine has a radial water inlet. The inlet water is fed through a spiral casing to ensure uniform distribution of water supplied around the turbine circumference. Stay vanes help to ensure this. The amount of water flowing into the runner is controlled by a ring of guide vanes (gates), which is controlled by the governor. The governor calculates the gate position based on the speed deviation, which again depends on the load demand and deviation [6, 8].

In a radial flow turbine, whose the Francis turbine is among, the water enters the turbine at one radius and leaves at a greater radius. Even though the flow enters radially in a Francis turbine, it leaves axially due to the shape of the turbine blades. The forces applied on the turbine blades consist of two components: One components is due to the pressure and the other component is due to the velocity of water. The latter one causes an impulse force on the blades, but it is of less importance than the other component. Thus it is considered as a reaction turbine. To ensure that the reaction turbine is always filled with water, a draft tube is submerged into the water level in the tailrace. Figure 2.2 shows the arrangement of a Francis turbine. The continuous water path makes Francis turbines suitable for pumped hydro power plants [6, 8].

A *Kaplan turbine* or *propeller turbine* are axial flow turbines. The turbines can be oriented either horizontally or vertically. A Kaplan turbine is a propeller turbine that is able to control the blade pitch to optimize the efficiency over a wide range of flow rates. Similar to the Francis turbine, a Kaplan turbine and a propeller turbine have a controllable arrangement of guide vanes to control the flow rate and thus also the power delivered [6].

A *pump as turbine (PAT)* is simply feeding water in reverse direction of a water pump. The water pump is usually used to increase the pressure in water systems. In the same way as for other reaction turbines, the PAT is suitable for relatively low water heads and relatively high flow rate (with respect to power demand). The efficiency of a PAT is not very high, and thus PAT applications are mostly limited to cases where the simplicity and costs are more important than the efficiency of the turbine (i.e. there is more water available than needed to accommodate the power demand).

Among the reaction turbines the Francis turbine is suitable for a wide range of hydraulic heads, from 40 meters and up to 360 meters. The flow rate range of this turbine is also wide. Kaplan and propeller turbines are most efficient for low hydraulic heads (< 45 meters) and high flow rates (e.g river power plants). PATs becomes an option only for low power generation.

For this thesis the maximum power demand supplied by the hydro turbine and the generator is 1.5 kW, and thus the turgo turbine and the PAT are suitable options. The nominal speed of the generator is 1500 rpm and no gear is desired to use (it will increase the costs). It is further assumed that the head and water flow at the actual plant site, fits the ratings of a turgo turbine. However, the details regarding the turbine are not the most important characteristics in this thesis. What is required is a realistic mathematical model of the hydro turbine and its governor. The governor controls the

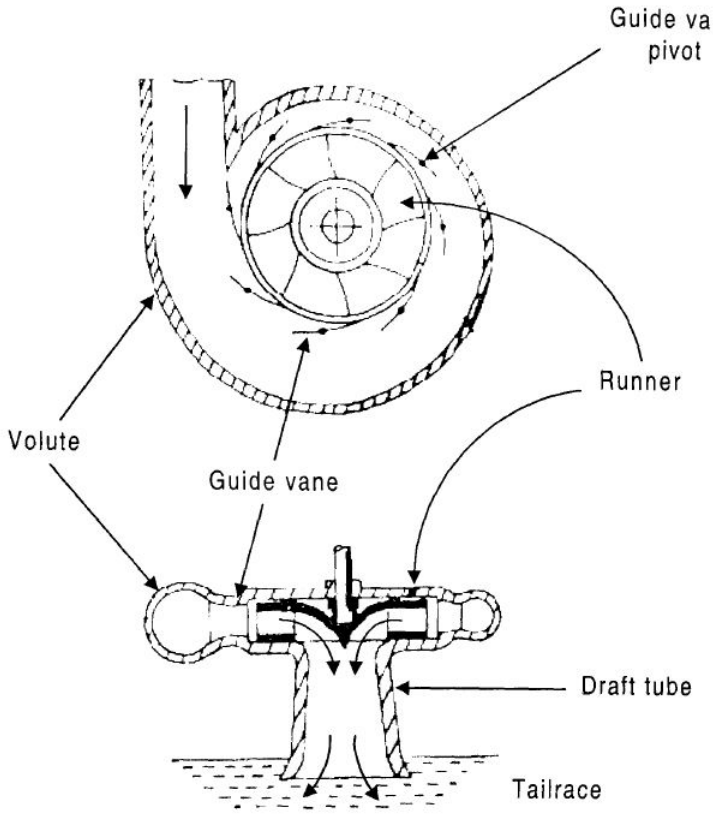

Figure 2.2: A Francis turbine is a reaction turbine. Here, its volute, gates and draft tube are shown. Figure 2.3 in [6]

the water inlet such that the speed achieves its reference value as the system load demand varies. This mathematical model with its simplifications is independent of the type of turbine (impulse or reaction) and is presented in the following subsection.

2.2 Linear Hydraulic Turbine Model

For both impulse and reaction turbines the control of the mechanical power or torque is done by adjusting the opening in the nozzle (impulse turbine) or wicket gates (reaction turbine). The model requires no detailed description of how the water acts on the turbine. What is needed for the model is a mathematical representation of how the output power changes when these gates are adjusted. In addition, a governor for controlling the gates in order to obtain the desired speed or power is needed. [5, 8, 11] derive this hydro-governor representation commonly used in stability studies. In the following only the classical transfer-function of an ideal, lossless turbine is derived. The approximated linear model is considered to be sufficient for this task, since these details is out of the main scope of this Master's Thesis. [5, 11] also derives a non-linear model assuming an inelastic water column which causes an oscillation of pressure waves in the penstock. This phenomenon is called water hammer.

According to [5] the representation of a hydraulic turbine and water column in stability studies is based on the following assumptions:

- The hydraulic resistance is negligible

- The water is incompressible and the pipe is inelastic
- The velocity of the water varies directly with the gate opening and with the square root of the net head.
- The turbine output power proportional to the product of the head and volume flow.

Based on these assumptions and equations relating to the flow of water in the pipe, turbine mechanical power and the acceleration in the water column, the classical linear transfer function 2.1 for a hydraulic turbine is derived in [5]:

$$\frac{\Delta P_m}{\Delta G} = \frac{1 - T_w s}{1 + \frac{1}{2} T_w s} \tag{2.1}$$

where ΔP_m is the change of turbine mechanical power and ΔG the change of guide vanes opening. T_w is the water starting time, and s is the Laplace operator. The water staring time, T_w represents the time required for the water in a pipe at length L, cross section A and a head H_{base} to accelerate from standstill to a flow rate at Q_{base}. T_w is defined by equation 2.2

$$T_w = \frac{L}{A} \cdot \frac{Q_{base}}{g \cdot H_{base}} \tag{2.2}$$

where g is the acceleration due to gravity. The Simulink implementation of the hydraulic turbine is shown in Figure 2.3:

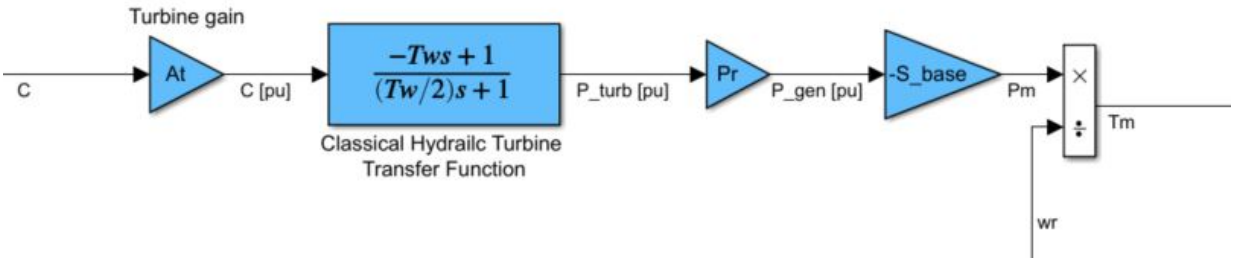

Figure 2.3: Simulink implementation of the linear hydraulic turbine model

The turbine gain, A_t is given by

$$A_t = \frac{1}{G_{max} - G_{min}} \tag{2.3}$$

where G_{max} and G_{min} are maximum and minimum gate position of the turbine, respectively. P_r is the ratio between turbine power rating and the nominal generator apparent power, S_{base}. P_r is used for converting between the turbine and generator per unit power quantities.

$$P_r = \frac{P_{turb,nom}}{S_{base}} \tag{2.4}$$

The mechanical shaft torque is found by the power and instantaneous mechanical speed w_r as shown in Figure 2.3.

Typical values for the water starting time T_w at maximum load are considered to be between 0.5 s and 4.0 s [5]. However, the values of T_w used in the simulation is 0.175 s. This value is based on calculations for rated operation of the turgo turbine used in the model. The length of pipe, L is set to be 45 m. By using equation 2.2 and varying the flow Q_{base} and water head H_{base} within the

turbine's rated ranges (see Table B.1), the resulting water starting times T_w are shown in Table B.1. $T_w \approx 0.175$ s corresponds to a turbine power of ≈ 2.2 kW. This turbine power rating is assumed to compensate for rotational losses and stator losses. It seems logical that a T_w for a hydraulic turbine that only supplies a load of 1.5 kW should be minor compared to larger commercial hydraulic turbines. Since the water flow rate, Q, changes during operation at different loads, and thus apparent generator and turbine power is less than the nominal apparent power, the water starting time will change with the turbine power and flow (i.e. loading). This simplification is assumed sufficient for this analysis. Implementing the non-linear turbine model accommodate the changes in T_w and is thus recommended by [11] when the turbine behaviors are significant for the analysis. Since turbine behaviors are of minor interest for this analysis, the linear model is sufficient for the mechanical torque control. The values used in the turbine model are given in Table 2.1

Table 2.1: Parameters used in the hydraulic turbine model

$\mathbf{A_t}$	Turbine gain	1.0265
$\mathbf{P_{turb}}$	Turbine power rating	2.2 kW
$\mathbf{P_r}$	Ratio between turbine and generator power ratings	$\frac{P_{trub}}{S_{base}}$
$\mathbf{T_w}$	Water starting time	0.175 s
$\mathbf{G_{min}}$	Minimum gate opening	0.001 pu
$\mathbf{G_{max}}$	Maximum gate opening	0.975 pu
$\mathbf{G_{init}}$	Initial gate opening	0.25 pu
$\mathbf{v_{g,lim}}$	Maximum gate speed	± 0.216 pu/s

The numerator of the hydraulic turbine linear transfer function shown in equation 2.1 has a zero in the right half-plane, ($s = \frac{1}{T_w}$). This zero makes the penstock-turbine system to be a *non-minimum phase system*. A non-minimum phase system is characterized by: When the system reference is doing a step, the system's response will initially be in the opposite direction than the applied step change [15]. Thus, a non-minimum phase systems in general have some more difficulties in obtaining stable control than minimum phase systems. For the case of a hydraulic turbine this means that a positive per unit step change in the gate position will initially cause a -2 pu step change in the output power. This is seen by applying the initial value theorem on equation 2.5: The steady state output will be 1 pu and is seen if the final value theorem is applied on equation 2.5. The complete step response in the time domain for $T_w = 0.175$ s is shown in Figure 2.4 and is given by 2.5:

$$\Delta P_m = [1 - 3e^{-t/\frac{T_w}{2}}] \cdot \Delta G \tag{2.5}$$

The physical understanding of this peculiar characteristics of the turbine-penstock system is caused by the water inertia. Supposing a sudden slightly closing of the gate (or nozzle) opening, the constant flow rate will initially cause an increase of the velocity through the turbine and thus the turbine output power P_m. The flow rate is reduced after a short delay and so will the power. Similarly, if the step change is positive, the velocity of the flow through turbine and the output power change will initially decrease before the flow rate increases and then they increase to the new steady value. This effect is mathematically reflected by the negative sign in the numerator of 2.1, which causes the non-minimum phase system.

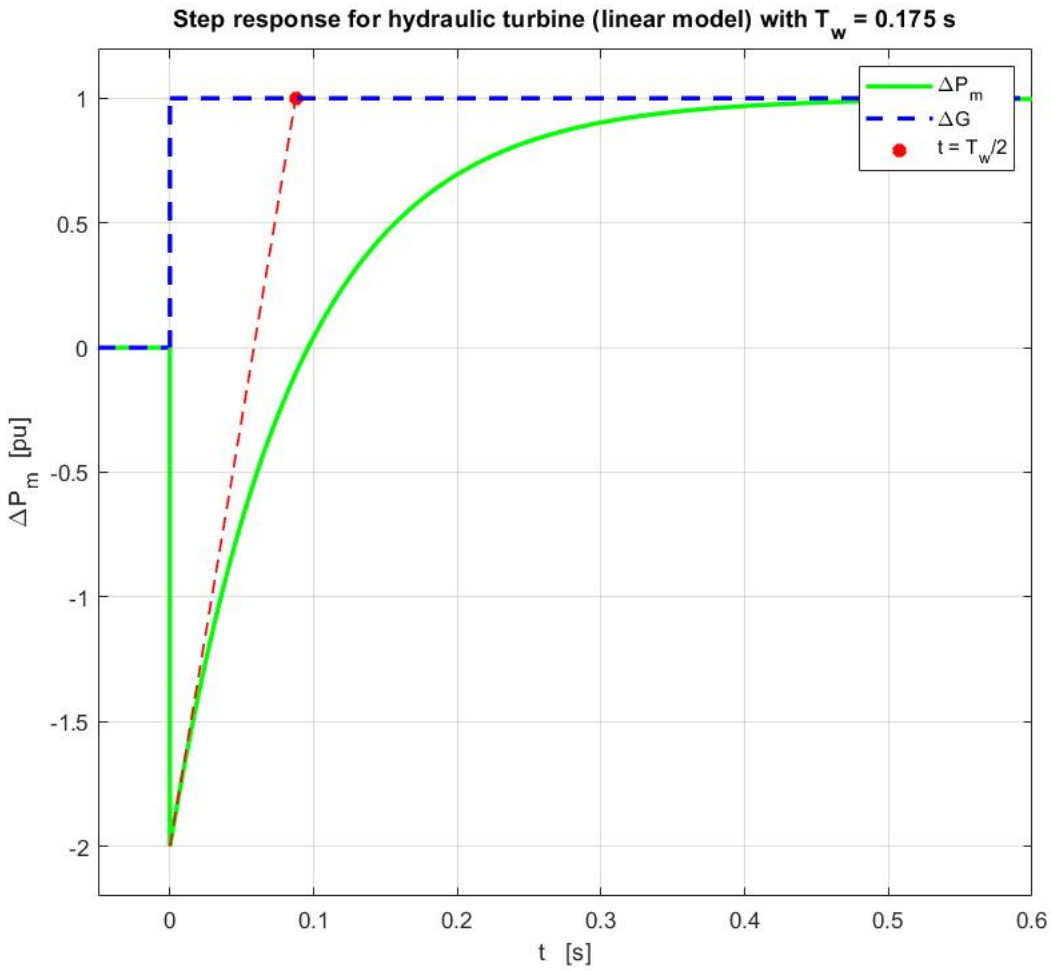

Figure 2.4: Step response for a linear hydraulic turbine with $T_w = 0.175$ s

The turbine model used in the Simulink model is based on data from the SUNECO 2.2 kW turgo turbine from [12]. The data are given in Table B.1. In Appendix B the procedure of determining the water starting time, T_w is discussed based on the given data.

2.3 Governor Model

The governor (i.e. control system) of a hydraulic turbine has the basic function of controlling the mechanical speed and/or the mechanical load based on the speed deviation. The control is done by adjusting the gate or nozzle opening of the turbine. The peculiar time response of the hydraulic turbine, which initially changes in the opposite direction of what is intended, must be compensated for by the governor. This is typically done by the *transient droop* which exhibits large droop (i.e low gain) for fast speed deviation and normal low droop (high gain) in the steady or permanent operation. The movement of the wicket gates (or nozzle openings) requires a relatively high force due to high hydraulic pressure and friction forces. In governing systems for hydraulic turbines with high power ratings, this consideration of forces applied to the gates is significant. It should be noted that a fast or sudden closure of the gates would lead to high pressure (due to the inertia of water) in the penstock and potentially damage the penstock, turbine or othe,r equipment. Thus limitations in the gate change rate is needed.

The functionality of a hydraulic governor system can be understood by studying the mechanical-hydraulic governor, which was commonly used to achieve the governing control at older hydro turbines. Figure 2.5 from [11] gives a schematic overview of the main components in the mechanical-hydraulic governor: It consists of a two stage hydraulic piston servo system to overcome the relatively high forces needed to adjust the gate position. The actual speed n_s is compared to the speed reference n_r with a modification of the permanent droop multiplied by the gate position (or output power of the generator). A fast change in the position generates a transient droop signal through a dashpot, illustrated by c in the upper right-hand corner of Figure 2.5. This transient droop signal is added to the modified speed error and is used as an input for the pilot valve. The servo system (pilot valve and servo and gate servomotor) works as an amplifier to obtain the force needed to adjust the desired gate position. The servo system gain is K_s.

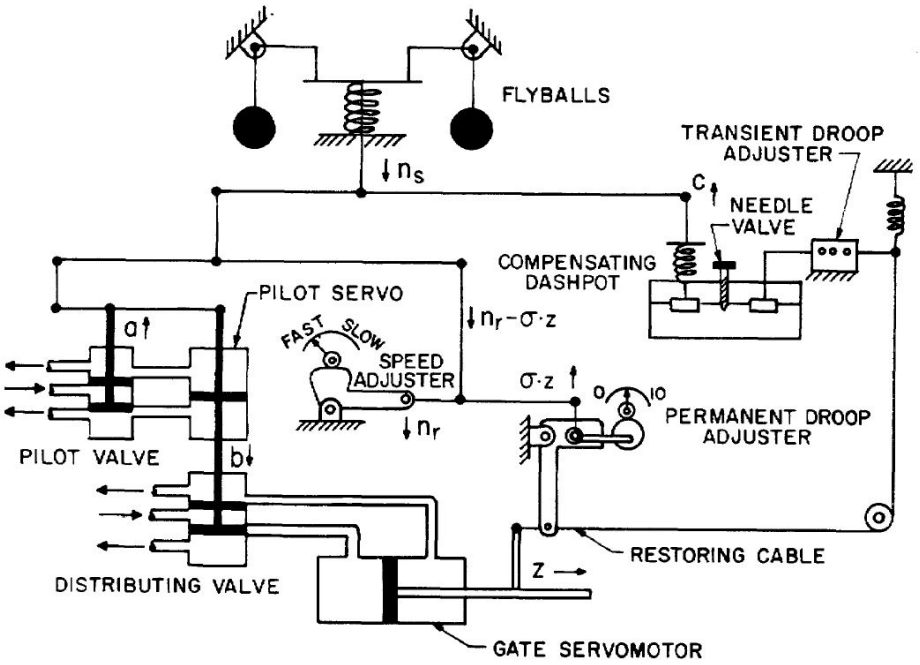

Figure 2.5: Simplified schematic overview of mechanical hydraulic governor. Figure 1 in [11]

In [11], Ramey and Skooglund derives the transfer function of the hydraulic governor in Figure

2.5. The transfer function of the two servo systems is derived to be:

$$\frac{z}{a} = \frac{K_1 K_2}{s(1 + T_p s)} = \frac{K_s}{s(1 + T_p s)} = \frac{1}{sT_s(1 + T_p s)} \tag{2.6}$$

where $K_1 K_2 = K_s = \frac{1}{T_s}$ is the open-loop gain of the servo system and T_p is the pilot valve time constant. The transient feedback transfer function 2.7 is obtained by assuming the dashpot water flow though the gate opening to be proportional to dashpot pressure:

$$\frac{c}{z} = R_t \cdot \frac{T_r s}{1 + T_r s} \tag{2.7}$$

where the transient droop, R_t, is based on the selection of pivot point on the piston. The reset time, T_r, is determined by the valve settings. In addition, the feedback loop of the permanent droop is added as a separate feedback. In [11], a detailed third order transfer function of the hydro governor is derived. This function is reduced to the second order function in 2.8 by neglecting the minor time constant of pilot valve and servo, T_p. This approximation is valid for the lower frequencies. For the higher frequencies it will indicate a larger phase margin and the more accurate transfer function should be used to ensure sufficient phase margin [10].

$$G(s) = \frac{\frac{1}{R_P} \cdot (1 + T_r s)}{\frac{T_r T_g}{R_p} s^2 + \frac{T_g + T_r \cdot (R_t + R_p)}{R_t} s + 1} \tag{2.8}$$

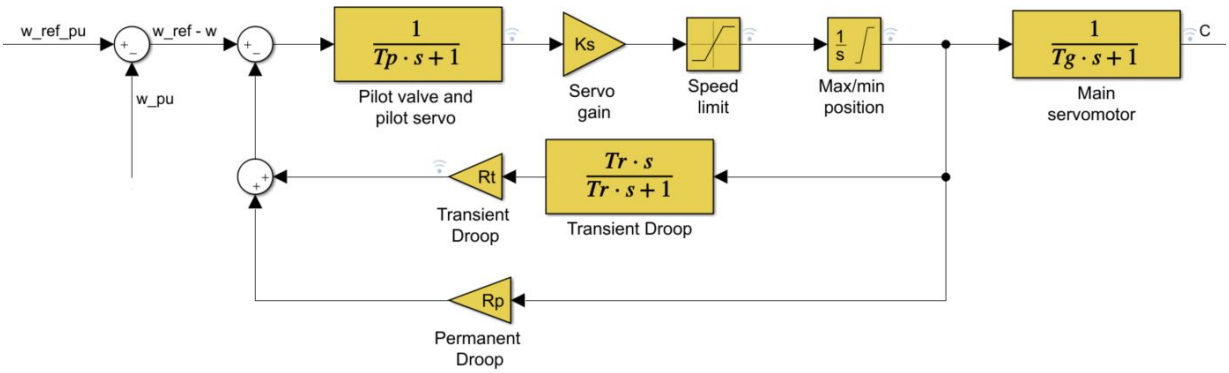

Figure 2.6: Block diagram of the governor control loop with transient and permanent droop. Delays of pilot and main servo motor are included.

Figure 2.6 shows a block diagram of the governor Simulink implementation based on equations 2.6 - 2.7 as showed. A direct implementation of equation 2.8 not done since equations 2.6 - 2.7 improves visibility and makes it easier to understand each parts functionality. It expresses the same functionality and relationships as the mechanical hydraulic governor in Figure 2.5 does. At the left side, the permanent and transient droop actions are subtracted from the per unit speed error. The pilot valve and servo time constant, T_p, is included even though it does not matter much for the turbine control. The servo gain, K_s, is equivalent to a proportional gain. Due to the physical constraints in gate opening speed and gate position, G, limitations for those are included. The integrator in 2.6 is

needed to obtain the desired gate position. It is fed into the closed loops with permanent droop, R_p, and transient droop given in 2.7. This control algorithm of the governor is called proportional control with transient droop. Today, these calculations and relationships are performed by a digital processor, the desired gate position is feed into the main servo motor, which has a time delay of T_g before the turbine recognizes the change.

In [13], Johan Björstved has simulated and done some laboratory work of a hydro power driven induction generator. He easily explain the concept of control by using the droop function: *A permanent droop is a permanent control error proportional to the power generator output or gate position.* A problem with this kind of generator is that in an island grid large load steps may result in a to large output of the controller, which can lead to large overshoots and instability in the gate opening. Therefore, an additional droop is added to the loop, which is only active during a fixed time after a step change.

Another way to explain the functionality of permanent and transient droop in the governor control loop can be: The permanent droop loop feeds a permanent control "error" into the speed error. This additional error from permanent droop is proportional to the output power of either the turbine (i.e. gate opening in pu) or the generator (generated electrical power pu). Thus, the signal fed to the governor gain, K_s, which in principle is a proportional gain, sees a larger speed "error" than the actual one. If the speed error is zero, the proportional controller sees an "error" sufficient to produce the steady state output signal to obtain the speed reference. An issue with the permanent droop controller, especially in island grids, is that large load steps will cause large output signals in the controller. Due to the peculiar response of the water turbine, these large output signal causes an overshoot in the gate opening and thus also the generator frequency. Large overshoots can lead the turbine into instability. This is the motivation for introducing the second feedback loop with transient droop. The transient droop introduces a high droop (i.e. low gain) a fixed time after a rapid change in speed (frequency). If the electrical load is increased, the frequency decreases. The transient droop obtains a positive value very fast and this value reduces the speed error fed into the controller. Hence, the output signal is reduced and the overshoot is avoided. The reset time, T_r, is a function of the water starting time and determines how long the transient droop signal is active. The limitations in gate opening rate and minimum and maximum gate opening must be added to the control loop. If the servo system's delay is included their time constants can be added, as done in Figure 2.6. Oftentimes, their significance is minor if the servo system is fast compared to T_w and other time constants in the system. The closed loop functionality of the permanent and transient droop functions can be explained by considering the forward transfer functions of the controller with permanent droop, $g_1(s)$, and the inverse transfer function of transient droop $\frac{1}{h_1(s)}$ given by

$$g_1(s) = \frac{K_s/s}{1 + R_p \frac{K_s}{s}} = \frac{1/R_p}{1 + s\frac{1}{K_s R_p}} \tag{2.9}$$

$$\frac{1}{h_1(s)} = \frac{1 + T_r s}{s R_t T_r} \tag{2.10}$$

The closed loop becomes

$$h_0(s) = \frac{g_1}{1 + g_1 h_1} \tag{2.11}$$

For low frequencies ($<3 \cdot 10^{-3}$ rad/s): $g_1(s) >> \frac{1}{h_1(s)}$, and hence $h_0(s) \approx g_1(s)$. For high frequencies ($>3 \cdot 10^{-3}$ rad/s): $g_1(s) << \frac{1}{h_1(s)}$, and hence $h_0(s) \approx \frac{1}{h_1(s)}$. This is visualized in the Bode diagram in Figure 2.7. It is seen that h_0 follows approximately the lowest gain of g_1 and $\frac{1}{h_1}$ at any time. The closed loop governor control function h_0, has a low gain of $\frac{1}{R_t}$ in the frequency range above reset time $\frac{1}{T_r}$ and a gain $\frac{1}{R_p}$ in the steady state. The second intersection at $\omega = K_s \cdot R_t = 35$ rad/s is of minor

importance for the control. The time constants of any servo system is assumed to be minor and thus neglected in the Bode diagram in Figure 2.7. It shows $g_1(s)$, $\frac{1}{h_1(s)}$ and $h_0(s)$ based on equations 2.9, 2.10 and 2.11, respectively, with $K_s = 5$, $R_p = 0.02$, $R_t = 7$ and $T_r = 0.20$ s.

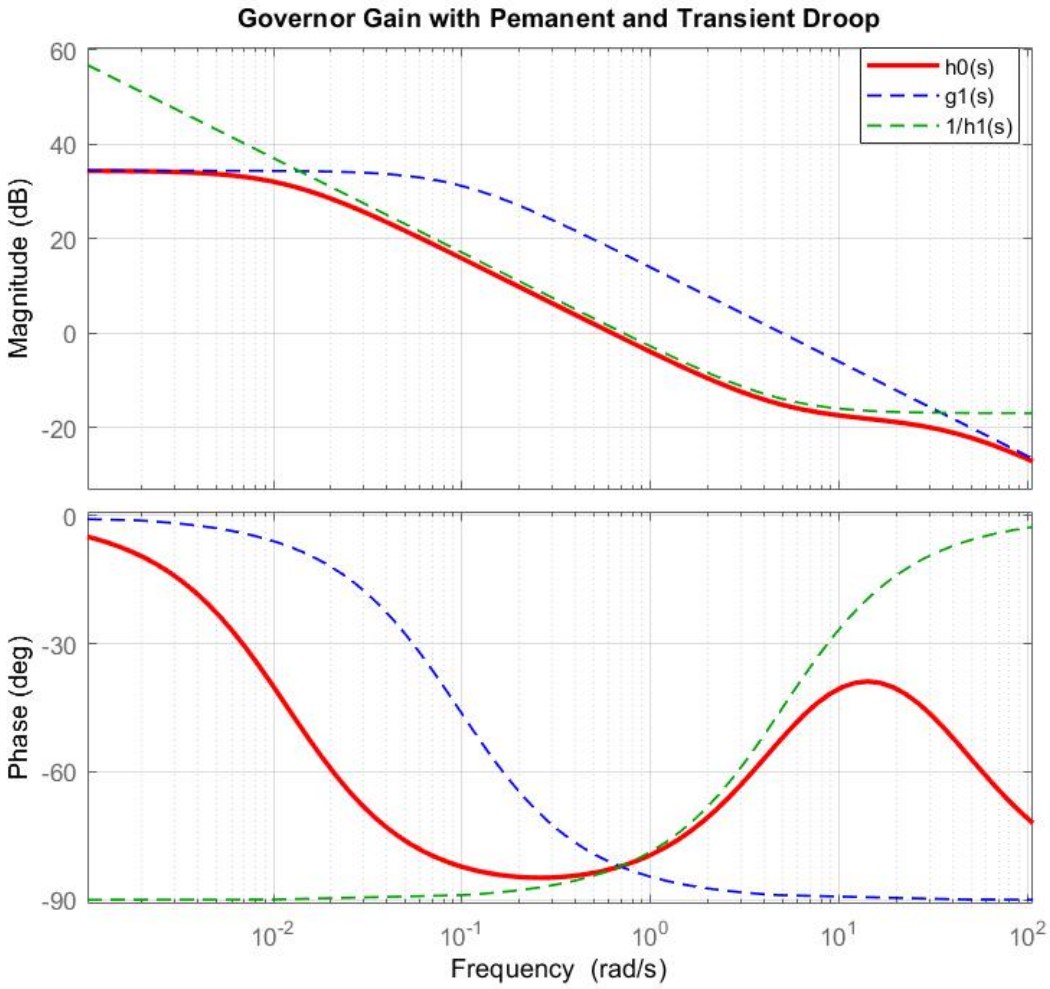

Figure 2.7: Bode diagram for h_0, g_1 and $\frac{1}{h_1}$. $K_s = 5$, $R_p = 0.02$, $R_t = 7$ and $T_r = 0.20$ s

2.3.1 Tuning of Governor Parameters

Several authors have proposed estimation techniques for parameters of the hydraulic turbine governor [5, 10, 11]. There are two important considerations regarding the tuning of governor parameters pointed out by [5]:

- The operation must be stable during isolated operation or conditions of system islanding.
- The response to loading and unloading during normal interconnected operation must be acceptable.

It is the stable operation during isolated operation that will be of significance in this task. For the general case, the requirements of these two considerations are conflicting. The latter requirement usually conflicts the first requirement by a to slow response. For a interconnected operation, a dashpot bypass arrangement can be made to secure stable operation with a reduced reset time, T_r, during loading and unloading.

The authors of [10, 5] states the relationships in 2.12 and 10.9 as the optimum choice of transient droop, R_t, and reset time ,T_r, during isolated operation. These are functions of the water starting time, T_w, and inertia constant, H.

$$R_t = \frac{T_w}{H} \cdot [1.15 - (T_w - 1) \cdot 0.075] \tag{2.12}$$

$$T_r = T_W \cdot [5 - (T_w - 1) \cdot 0.5] \tag{2.13}$$

Inserting T_w = 0.175 s and H = 0.2512 in 2.12 and 2.13 gives R_t = 1.685 and T_r = 0.9472 s. These values have been used as a starting point in order to tune the governor droop parameters properly. For this case, the low value of the water starting time has an influence on the governor tuning process: Initially, the permanent droop, R_p, was set to 0.04 based on [5]. These values will give a underdamped speed response to load step changes. To avoid these speed oscillations, a higher gain in the transient period is desired. In [13], the transient droop, R_t, is set to be 7 and the reset time is set to 2 s. Further investigation of the trade-off between a good steady state performance and a good transient performance has been made by using the trial and error method. In this case, the steady state has been favored, such that large overshoots or oscillations is avoided and stability is achieved. The response might be slower which can leads to temporary larger speed deviations. As stated in Table 2.2, the transient parameter droop was kept at 7 and the reset time was reduced to 0.2 s. In this case, the reduction of the reset time makes the controller able to act on the speed difference at an earlier stage after a disturbance and thus minimize the speed deviation. The non-minimum phase characteristic of the turbine with T_w= 0.175 s becomes minor when the limitations in the gate opening rate is included.

This large speed deviations could be allowed in this case since the electrical load frequency is decoupled form the generator speed and frequency by the DC-link in the back-to-back converter. Thus, there are no speed requirements for the turbine-generator set as long as the speed is kept stable and is sufficient to maintain the generator magnetization and the DC-voltage reference. Large load steps that causes speed drops up to -500 rpm (-0.33 pu.) for a short time can be allowed. The allowed size of the load step is dependent on the generators loading and the total shaft inertia in addition to the turbine response.

Since T_w is less than usual, the effect given by the non-minimum phase characteristics does not have any large significance. According to [10], the reset time, T_r, proposes to be 4 to 5 times T_w. It could also be estimated by 2.13. Skooglund and Ramey [11] are among those who state 5 times T_w would be a good choice. Common for all proposals is that they will give a crossover frequency ω_c in

a Bode diagram close to $\frac{1}{2T_w}$. Equations 2.12 and 2.13 are stated as tuning alternatives in [5]. The working group in [10] states the following requirements for stability in the speed control loop:

- The transient gain, $\frac{1}{R_t}$ does not exceed:

$$\frac{1}{R_t} \leq 1.5\frac{H}{T_w} \tag{2.14}$$

- The crossover frequency, ω_c, satisfies $\frac{1}{T_r} \leq \omega_c \leq K_s R_t$ where:

$$\omega_c \approx \frac{1}{2HR_t} \tag{2.15}$$

Table 2.2: Parameters used in the governor model

$\mathbf{K_s}$	Servo/Proportional gain	5.0
$\mathbf{T_p}$	Pilot valve and servo time constant	0.0002 s
$\mathbf{T_g}$	Main servo time constant	0.0005 s
$\mathbf{R_p}$	Permanent droop	0.02
$\mathbf{R_t}$	Transient droop	7
$\mathbf{T_r}$	Reset time	0.20 s
$\mathbf{T_w}$	Water starting time	0.175 s
$\mathbf{T_m = 2H}$	Mechanical starting time	0.252 s

Those requirements are satisfied for the values given in Table 2.2. The effect of the pilot servo time constant, T_p, is usually negligible when considering the system [11]. Even though it does not have any significant influence on the governor's performance, T_p is included in the governor model in Figure 2.6. The delay of the main servomotor, T_g (gate), is included in the governing control (Figure 2.6) since the control is performed by digital processors and there is a short delay in the piston movement before the actual gate change occurs. It is thus placed outside of the control loop. The effect of the servomotor time constants (T_p and T_g) is only important for the stability if their poles occur before the crossover frequency, ω_c.

2.3.2 Alternative Governor Schemes

Even though the functionality of digital droop controlled hydro governor is good, the use of other types of hydro governors such as PID-controllers (i.e. Proportional, integral and derivative) are widely used for governing purposes of hydraulic turbines. The functionality of those is described in Appendix D. PID-controllers allow the possibility of higher response speeds by providing both transient gain reduction and transient gain increase. The derivative action is beneficial for isolated operation, particular for plants with large T_w. However, the use of a high integral and derivative gains K_i and K_d for transient gain increase, will result in excessive oscillations and possibly instability when the generating unit is strongly connected to an interconnected system. Thus, the derivative gain can be excluded from the controller. Without the derivative action, the resulting PI-controller is equivalent to that of the mechanical-hydraulic governor. The proportional and integral gains may be selected in a way that result in result in the equivalent controller parameters corresponding to the temporary droop, R_t, and reset time, T_r. Another common way of reducing the steady state error is by incorporating integral action into the controller.

3 Characteristics of the Squirrel Cage Induction Generator

The discussion in this chapter makes a foundation for describing the SCIG-control techniques: V/f-method (scalar control), Direct and Indirect Vector Control, which are discussed in the later chapters. The most common fundamental characteristics of induction generators have been discussed in [3], and consequently the discussion here is taken a step further and it is assumed that the reader is familiar with these fundamentals.

3.1 Torque-Speed Characteristic

Figure 3.1 a) is oftentimes used as a single phase equivalent circuit for analysis of the squirrel cage induction machine. In Figure 3.1 b) the core losses, due to R_i, are also included, these losses are as usual neglected here.

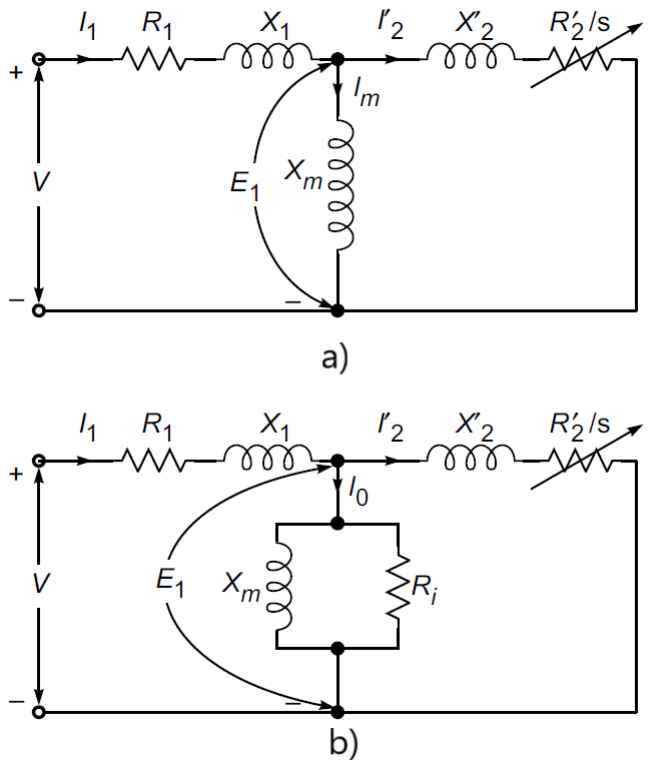

Figure 3.1: Single phase equivalent model of a squirrel cage induction machine. Figure 9.7 in [21]

In equations 3.1, 3.3 and 3.5 the air-gap power, (i.e power transferred from rotor to stator), the converted power (from mechanical to electrical power), and the converted torque, are given respectively

$$P_g = \frac{3I_2^2 R_2}{s} = \frac{3V_\phi^2 R_2/s}{(R_1 + R_2/s)^2 + (X_1 + X_2)^2} \tag{3.1}$$

where the latter equality is based on the assumption that $I_m = 0$ in Figure 3.1a), which makes

$$I_2 = \frac{V_\Phi}{(R_1 + R_2/s)^2 + (X_1 + X_2)^2} \tag{3.2}$$

The converted power, P_{conv}, includes the electrical power dissipation in rotor and is equal to the mechanical power, P_{mech}:

$$P_{mech} = P_g(1-s) = 3I_2^2 R_2 \cdot \frac{1-s}{s} \tag{3.3}$$

The mechanical torque converted to electrical torque is given by the ratio

$$\tau_{conv} = \frac{P_{mech}}{\omega_r} \tag{3.4}$$

and by multiplying the ratio by (1-s) one obtaines:

$$\tau_{conv} = \frac{P_g}{\omega_s} = \frac{1}{\omega_s} \cdot \frac{3V_\phi^2 R_2/s}{(R_1 + R_2/s)^2 + (X_1 + X_2)^2} \tag{3.5}$$

Equations 3.1, 3.3 and 3.5 are plotted in Figure 3.2 below, to obtain the torque-speed characteristic and power speed characteristics of #IM1, the 1.5 kW induction machine. The parameter values used are given in Table A.3.

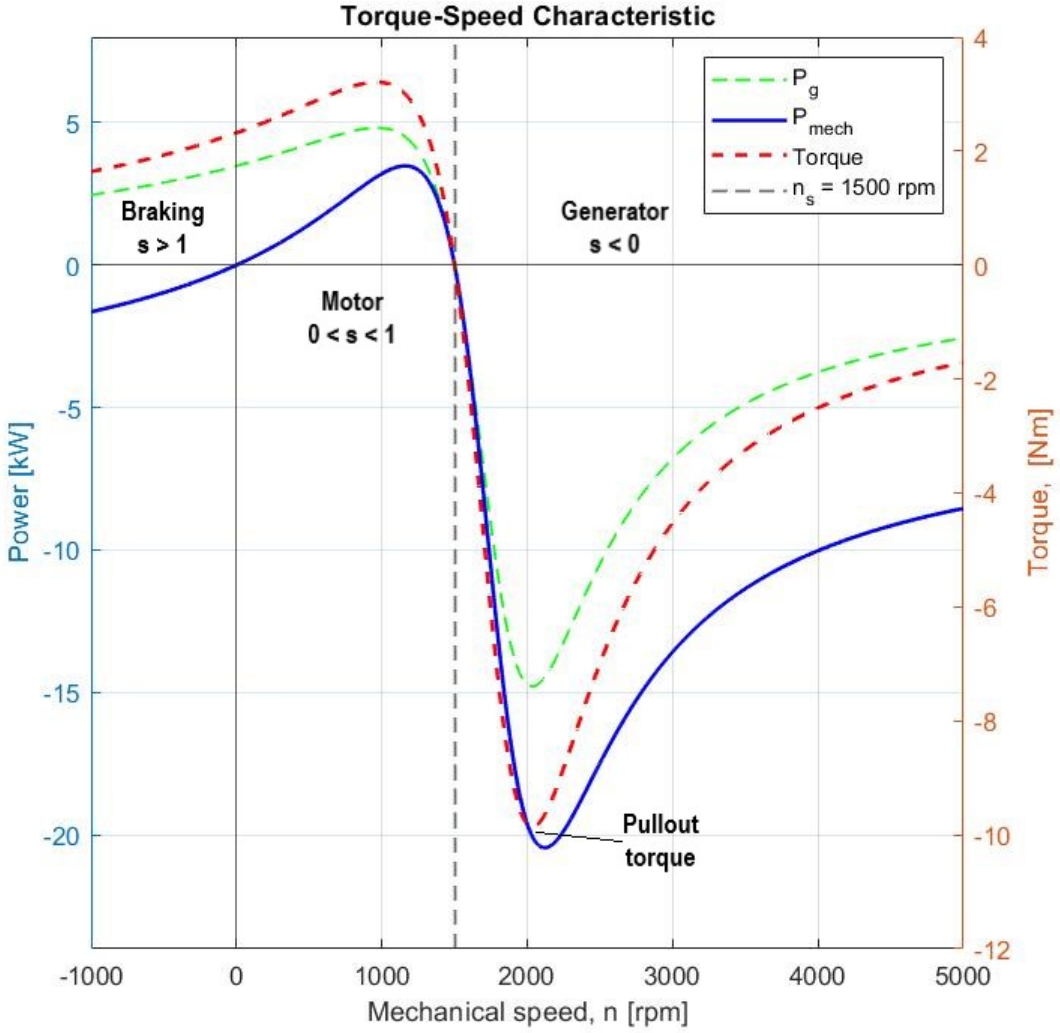

Figure 3.2: Plots of torque-speed and power-speed characteristic for #IM1

From the characteristics of torque-speed and power speed in Figure 3.2 and the above equations, several useful observations can be drawn:

- At the synchronous speed there is no torque and no power transfer.
- At rest (zero speed) the mechanical power will naturally be zero.
- The torque-speed characteristic and the power-speed characteristics are almost linear in the range from full-load to no-load. This is because the rotor resistance, $\frac{R_r}{s}$, is much larger that the rotor reactance, X_r, in the operating range. close to synchronous speed (low slip, s).
- The domination of rotor resistance in operation range, also make a linear increase of current, rotor field and torque with the slip, s.
- In the generator mode ($s < 0$) the mechanical shaft power is converted to electrical power by the external torque from the turbine to turn the rotor.
- In motoring mode ($0 < s < 1$) the machine absorbs electric power in the rotor and converts it to mechanical power.
- The rotor torque is varying with the square of terminal voltage, V_ϕ^2 (Equation 3.5).
- If the speed slows down to the synchronous speed, there is no electromotive force induced in the rotor, and therefore there is power transfer across the airgap, $P_g = 0$. Hence, also the mechanical torque becomes zero.
- In the braking region (s > 1) the generator absorbs the mechanical power on the shaft, and thus $P_{mech} < 0$.
- For a given value of current drained from the generator the maximum generated power occurs (see chapter 3.2).
- The pullout torque (maximum torque) is ≈ -10 Nm for #IM1. It occurs at a slightly different speed than maximum power.

According to [16], the total frequency variation should be limited to not much more than 5 %. This is an acceptable deviation for most loads in a stand alone plant. The back-to-back converter has a decoupling effect between the generator speed and the load frequency. With proper control it allows much greater deviations in the speed while maintaining good voltage quality and a load frequency at 50 Hz.

The electrical output power, P_{out}, of the SCIG is determined from the mechanical input power and all the inherent losses of the SCIG:

$$P_{out} = P_{mech} - P_{loss} = -3I_2^2 R_r \cdot \frac{1-s}{s} - 3I_1^2 R_s - 3I_2^2 R_r - \frac{3E_g^2}{R_m} - P_{fric+air} - P_{stray} \qquad (3.6)$$

By obtaining the expressions or estimations for these losses in a specific operating state (i.e. for a given frequency, temperature and operating voltage), the output power, P_{out}, can be determined or estimated.

3.2 Power vs. Load Current Characteristic

The relations between load current and output power become significant when optimized control methods for the induction generator are studied. It is desired to obtain a relationship between load current and power that is independent of slip. The dissipation of power in the rotor is defined by 3.7 and used as a starting point.

$$P_{mech} = 3I_2^2 R_r \cdot \frac{1-s}{s} \tag{3.7}$$

By rearranging equation 3.2 to isolate the term $\frac{R_r}{s}$, one obtains:

$$\frac{R_r}{s} = \sqrt{\left(\frac{V_\phi}{I_2}\right)^2 - (X_s - X_r)^2} - R_r \tag{3.8}$$

which inserted to 3.7 gives:

$$P_{mech} = 3 \cdot I_2^2 \cdot \left(\sqrt{\left(\frac{V_\phi}{I_2}\right)^2 - (X_s - X_r)^2} - (R_s - R_r)\right) \tag{3.9}$$

Equation 3.9 is plotted for V_Φ = 230 V in Figure 3.3. The square root in 3.9 introduces the constraint:

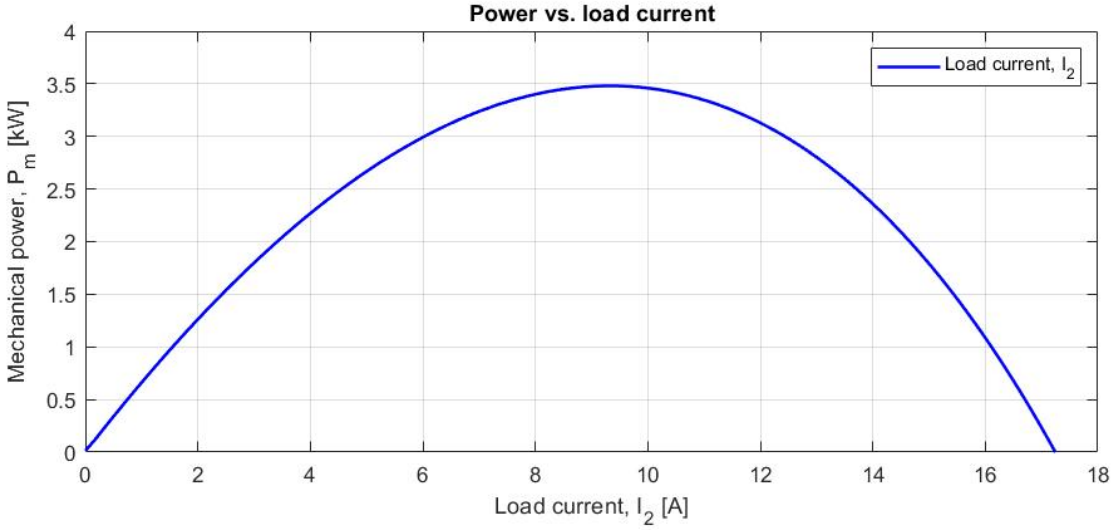

Figure 3.3: Power vs. load current, I_2

$$\left(\frac{V_\phi}{I_2}\right)^2 \geq (X_s - X_r)^2 \tag{3.10}$$

By rearranging 3.10 respect to I_2 one obtains the current constraint:

$$I_2 \leq \frac{V_\Phi}{X_s + X_r} \tag{3.11}$$

The rotor current I_2 must be kept below this limit during operation. The maximum power can be found by inserting the 3.11 into 3.9. Knowing the characteristic, shown in Figure 3.3 is very useful in optimized induction generator control when using fuzzy logic.

3.3 Nonlinear relation between air-gap voltage and magnetizing current

The non-linear relationship between the air-gap voltage, V_g, and the magnetizing current, I_m, is the main factor in the excitation (magnetization) process of an SCIG. The magnetizing reactance, X_m, is derived form this relationship $\left(\frac{V_g}{I_m}\right)$ and results in a non-linear relationship because of magnetic saturation. A common way to determine this relationship is to use a table of experimental values from a laboratory set-up. The terminal voltage and magnetizing current as well as derived quantities measured during the laboratory work during the project work [3], are given in Table A.6. During these measurements, the machine was driven at no-load in motoring mode. This make the machine unable to reach the synchronous speed with zero slip ($s = 0$) for low terminal voltages, < 50 V (or 100 V if one is strict). Thus, the measurements below 50 V are invalidated, and excluded from Table A.6 and the following work. In the case of redoing the experiment, one could have used a DC-machine rotating at 1500 rpm coupled to the shaft of the induction machine when applying the voltages to the terminals during the no-load test [16]. In this work, the magnetizing reactance is assumed constant in the low voltage range (0-50 V).

In the Simulink-model (Figure F.1), the Asynchronous Machine-block takes a data set of the measured no-load magnetizing current, I_m, and the line-to-line terminal voltage ($V_{LL} = \sqrt{3} \cdot V_\Phi$) as inputs. This is done to simulate magnetic saturation of the mutual magnetic flux in the iron of stator and rotor. This saturation is necessary to obtain a stable operation point of the generator. Hence, the machine block follows a piecewise linear relationship between the sample points. The first sample point is set to the origin by the simulator, and thus only sample points form the non-linear region are needed.

Even though the Asynchronous machine-block uses terminal voltage as an input, the air-gap voltage, V_g, across the magnetizing reactacne is also of interest when studying the magnetic saturation. The air gap voltage, V_g, is found by:

$$V_g = V_\Phi - \left(I_m \cdot \sqrt{R_s^2 + X_s^2}\right) \tag{3.12}$$

Equation 3.12 assumes $I_m = I_1$ ($I_2 \approx 0$). The magnetizing reactance X_m is found by:

$$X_m = \frac{V_g}{X_m} \tag{3.13}$$

Thus, the X_m can be determined for each set of no-load measurements.

According to [16], the non-linear relationship described by X_m, can be expressed with a polynomial expression found by using linear regression of the data points [17, 16]. The polynomial could be on the form:

$$X_m = a_0 + a_1 V_g + a_2 V_g^2 + a_3 V_g^3 \tag{3.14}$$

where a_0, a_1, a_2 and a_3 are constants to be determined.

The authors of [16] present a method that relates the air-gap voltage to the magnetizing current by using the non-linear relation expressed in equation 3.15:

$$V_g = F I_m \left(K_1 e^{K_2 I_m^2} + K_3\right) \tag{3.15}$$

where F is the frequency in pu and K_1, K_2 and K_3 are constant to be determined. These constants can be determined on the basis of only three single measurements.

3.3.1 Linear regression

In this work it is chosen to use the non-linear relationships between air gap voltage, V_g, and magnetizing reactance, X_m, as a polynomial instead of using 3.15, since more than three measurements are available. It is the *Curve Fitting Tool* in Matlab that is used to perform the linear regression. The linear regression is done in order to obtain the polynomial coefficients describing the non-linear relation based on the data set.

A 3^{rd}-order polynomial is found to be sufficient to fit the no-load terminal voltage, V_Φ, and air-gap voltage, V_g, as functions of the magnetizing current I_m. The expression is on the form:

$$V = a_0 + a_1 I_m + a_2 I_m^2 + a_3 I_m^3 \tag{3.16}$$

and the respective coefficients are given in the Table 3.1. The curves of X_m as a function of V_Φ and

Table 3.1: Coefficients for V_Φ and V_g used in equation 3.16

	$\mathbf{V_\Phi}$	$\mathbf{V_g}$
$\mathbf{a_0}$	-8.186	-8.186
$\mathbf{a_1}$	183.1	176.4
$\mathbf{a_2}$	-42.7	-42.7
$\mathbf{a_3}$	3.4	3.4

V_g are plotted as red curves in Figure 3.4a and 3.4b respectively. The blue dots are measured values or values derived from measurements.

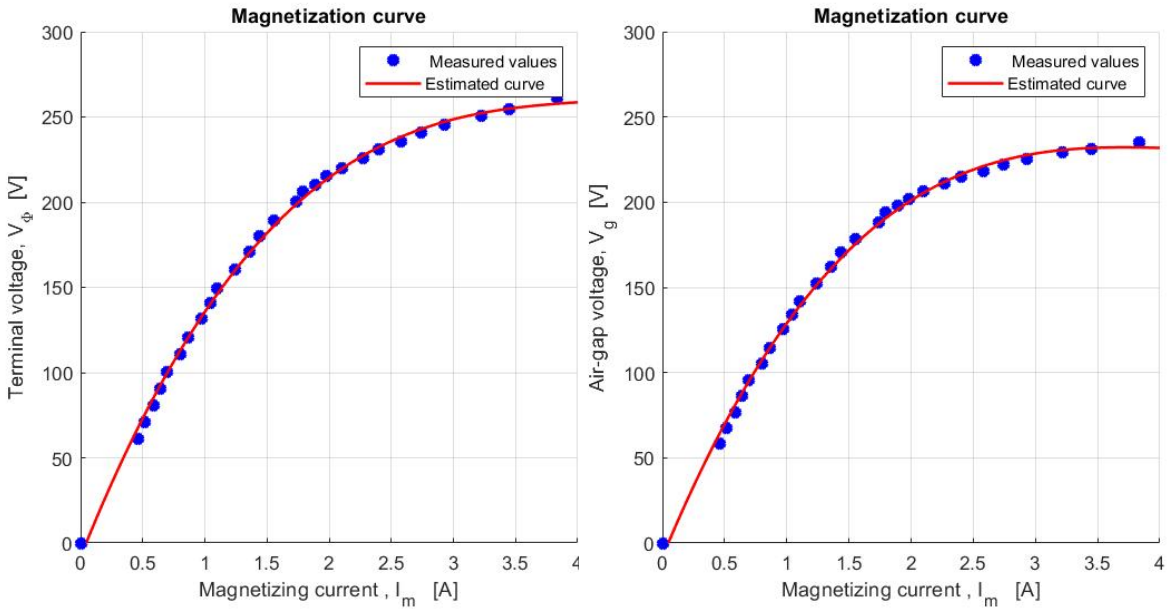

(a) Terminal voltage V_Φ vs. magnetizing current, I_m (b) Air-gap voltage V_g vs. magnetizing current, I_m

Figure 3.4: Estimated magnetizing curves (red lines) and measured values (dots)

The magnetizing reactance, X_m, can be expressed as a function of I_m or a function of V_g in a

similar way. The variety of X_m with respect to I_m is best fitted as a 4^{th}-order function:

$$X_m = a_0 + a_1 I_m + a_2 I_m^2 + a_3 I_m^3 + a_4 I_m^4 \tag{3.17}$$

where the coefficients are given in Table 3.2. In the same way X_m fits V_g best as a 4^{th}-order polynomial:

$$X_m = a_0 + a_1 V_g + a_2 V_g 2 + a_3 V_g^3 + a_4 V_g^4 \tag{3.18}$$

where the coefficients are given in Table 3.2. Figures 3.5 and 3.6 show how the magnetizing reactance, X_m, varies with magnetizing current and air-gap voltage for #IM1 with rated current at 3.45 A. The values derived from measurements are marked as blue dots. It is seen that X_m decreases as the current and voltage reaches its nominal values. The other machine models (#IM2 - #IM6) are based on the same per unit model and similar curves (Figure 3.4, 3.5 and 3.6) can be obtained for those. The dataset of terminal voltage and magnetizing current, Figure 3.4a, is given to the Asynchronous machine block in Simulink. The terminal voltage needs to be adjusted by a factor of $\sqrt{3}$ to obtain the line-to-line terminal voltage.

Table 3.2: Coefficients in the polynomial of X_m with respect to I_m and V_g (Equation 3.17 and 3.18)

	$\mathbf{I_m}$	$\mathbf{V_g}$
a_0	125	137.7
a_1	38.19	-0.3494
a_2	-45.44	4.4765e-3
a_3	12.45	-1
a_4	-1.128	1.961e-5

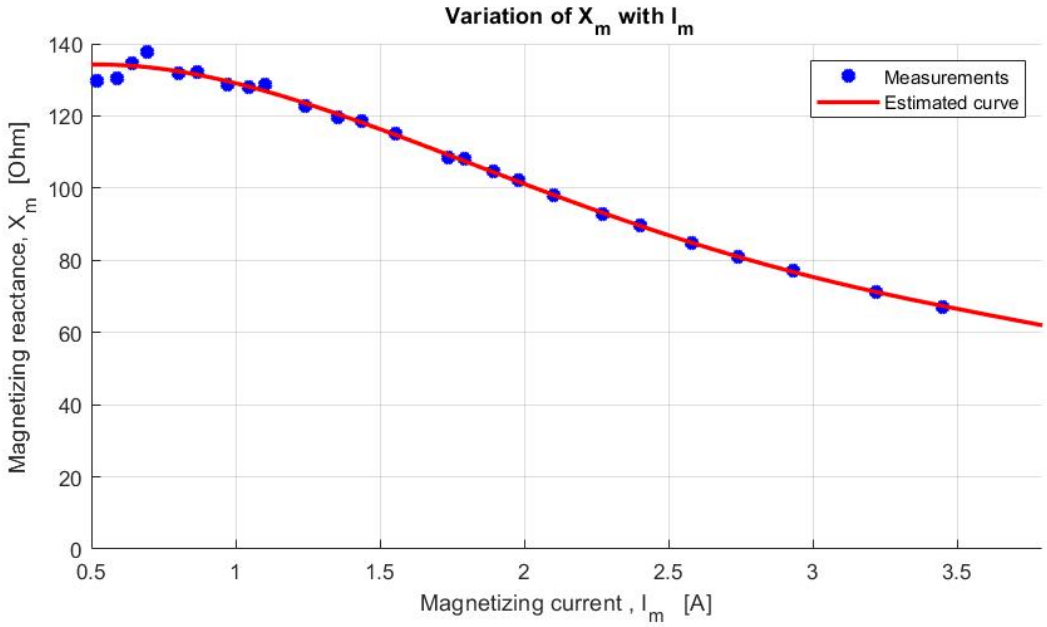

Figure 3.5: Variation of the magnetizing reactance with respect to magnetization current. #IM1

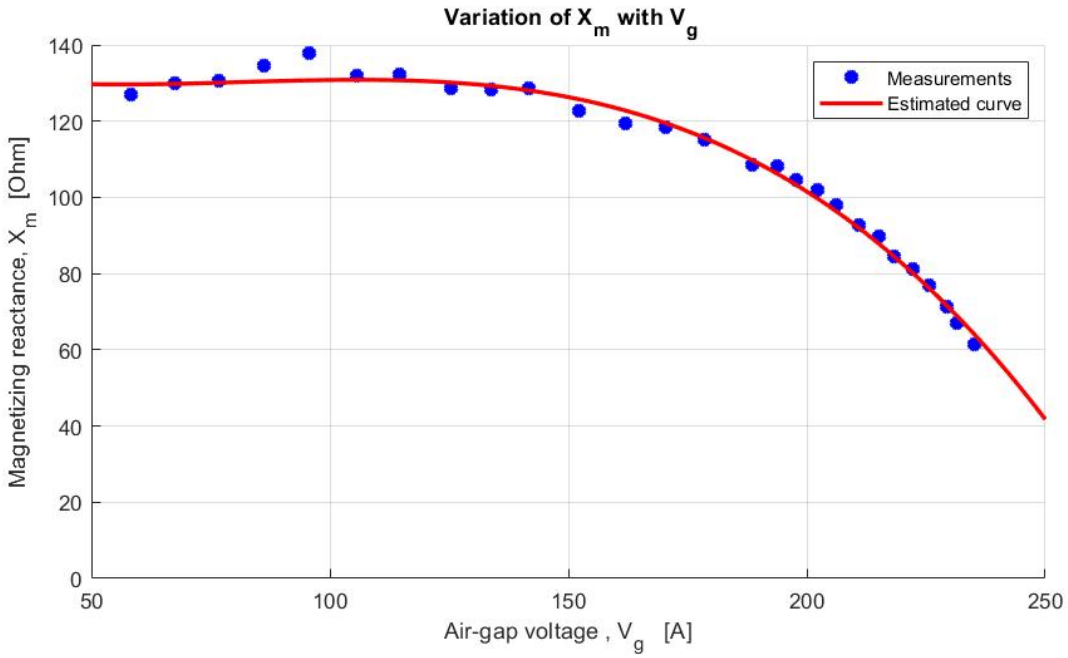

Figure 3.6: Variation of the magnetizing reactance with respect to air-gap voltage. #IM1

3.4 Behavior of Squirrel Cage Induction Generator in Grid Connected Operation

When an induction generator is directly connected to the transmission grid, or at least a power grid with several generating units, the electric (synchronous) frequency will be equal to the grid frequency. If the induction machine is run above the synchronous speed by an external mechanical torque (from a turbine) it will supply active power to the grid (generating) since the slip becomes negative. If the mechanical speed is slowed down (less torque is applied to the shaft) below the synchronous speed, the induction machine start to operates as a motor, which consumes active power from the grid. Both generator and motor operation of the grid connected induction machine will consume reactive power from the grid if no reactive compensation is used. In the isolated case the reactive power must be delivered from a reactive compensation (i.e. capacitor bank or SVC etc.). This is discussed in more details in the Project Work [3]. Alternatives are proper control of the VSC: Control method for induction machines such as V/f-control and IVC (see chapter 9 and 10) control the VSC in a such manner that it supplies reactive power to the machine and the machine is kept magnetized.

4 Converter and DC-link

To achieve the decoupling effect of the induction generator and the isolated load, a back-to-back converter arrangement is used. It consist of two independently controlled AC/DC-converters, connected by a DC-link. The DC-link is connected to a capacitor for stabilizing the DC-voltage, and thus the system's performance.

4.1 Voltage Source Converters - VSC

There is a great variation of converter topologies that can be used to convert AC/DC transition. The controllability, complexity and AC-voltage quality (i.e harmonic distortion - THD) varies among the available converter topologies. The switching components that make up the circuit topology are semiconducting devices and could be diodes, thyristors, IGBT's (Insulated-Gate Bipolar Transistor) or MOSFET's (Metal–Oxide–Semiconductor Field-Effect Transistor). One commonly used topology is the voltage source converter - VSC. An advantage of the VSC is that it can be controlled to give an arbitrary AC-voltage for a given DC-voltage. In principle, the topology of the VSC can be made for an arbitrary number of phases and an arbitrary number of levels. Since the AC-systems are 3Φ and the complexity of the converter and its control system increases with the degree of converter levels, a 2L-3Φ VSC is chosen as suitable for the purpose. The switching device is chosen to be IGBT with shunt diodes for allowing 4-quadrant operation in the *iv*-plane.

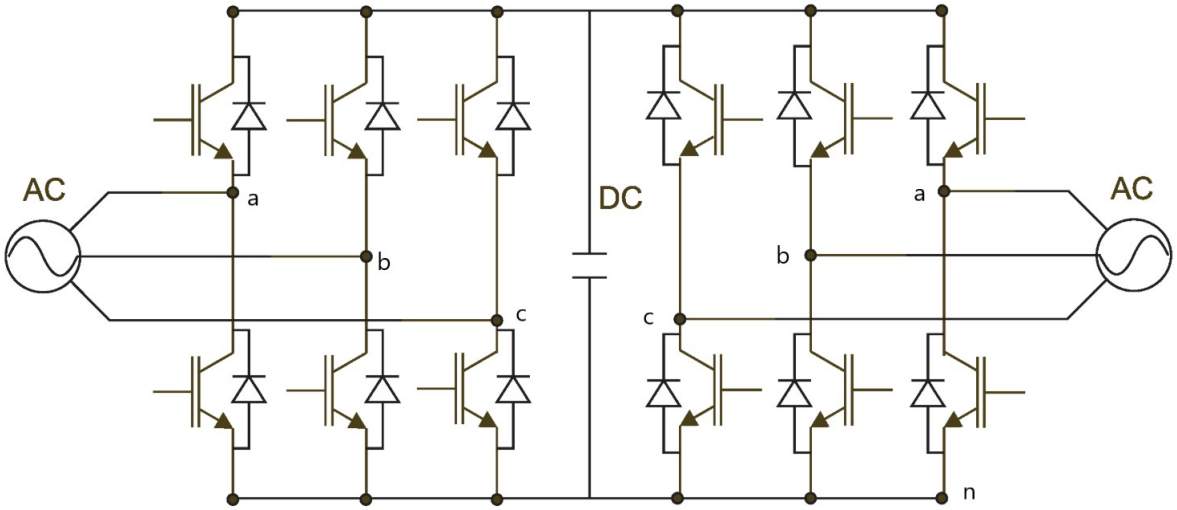

Figure 4.1: 2L-3Φ IGBT/diode-based back-to-back converter topology

4.1.1 2L-3Φ VSC

A 2L-3Φ VSC consists of a DC-circuit, an AC-circuit and three phase legs with two voltage steps on each leg. The legs have an upper and a lower pair of IGBT and diode. The AC-phase is connected to the midpoint of the phase leg. When the upper IGBT is on, the midpoint is short circuited to the positive DC-voltage, and when the lower switch is on, the midpoint is connected to the "negative" DC-voltage (point n in Figure 4.1). The upper and lower switch can never be in their on state simultaneously, since this operating state will short circuit the DC-link voltage. By defining N to be the neutral-point of the star (Y) connected AC-load or generator, v_{aN} becomes the phase voltage of phase a. v_{Nn} is the voltage difference between the Y-point, N and the negative node in the DC-link, n. We have:

$$v_{aN} + v_{bN} + v_{cN} = (3 \cdot v_{nN}) = 0 \tag{4.1}$$

Equation 4.1 can be rearranged to:

$$v_{nN} = \frac{1}{3}(v_{aN} + v_{bN} + v_{cN}) \tag{4.2}$$

For each phase, the voltage between mid-point and negative DC-node, n can be expressed:

$$\begin{aligned} v_{an} &= v_{aN} - v_{Nn} \\ v_{bn} &= v_{bN} - v_{Nn} \\ v_{cn} &= v_{cN} - v_{Nn} \end{aligned} \tag{4.3}$$

By inserting 4.2 for v_{nN} in 4.3, the expressions for the three phase voltages are given by v_{an}, v_{bn} and v_{cn}:

$$\begin{aligned} v_{aN} &= \frac{2}{3}v_{an} - \frac{1}{3}(v_{bn} + v_{cn}) \\ v_{bN} &= \frac{2}{3}v_{bn} - \frac{1}{3}(v_{an} + v_{cn}) \\ v_{cs} &= \frac{2}{3}v_{cn} - \frac{1}{3}(v_{an} + v_{bn}) \end{aligned} \tag{4.4}$$

Since the instantaneous values of v_{an}, v_{bn} and v_{cn} are either V_{dc} or 0, five possible output values (states) for the phase voltages $[v_{aN}, v_{bN}, v_{cN}]$ exist: $[-\frac{2}{3}V_{dc}, -\frac{1}{3}V_{dc}, 0, \frac{1}{3}V_{dc}, \frac{2}{3}V_{dc}]$.

The functionality described above is achieved in the Simulink Model by the Universal bridge block, found in the Simpace library. The number of bridge arms is set to 3, and IGBT/Diodes is selected as Power electronic device. Ideal switching characteristics are assumed, and thus the snubber resistance and snubber capacitance are set to infinity, and R_{on} (the conduction resistance) is set zero. The gate signal port receives the six gate signals from the controller.

4.2 DC-link

The DC-link contains the conductors, a capacitor and a battery. The capacitor is used to achieve a stable DC-circuit for each of the independently controlled VSCs. The battery is used to get an initial DC-voltage so that the generator can excitate and build up voltage at its terminals.

Capacitor
Th DC-link capacitor size is based on desired ripple in DC-link voltage, the charging time and the resilience of the system. A loaded capacitor stores a certain amount of energy, U, given by:

$$U = \frac{1}{2}C_{dc}V_{dc}^2 \tag{4.5}$$

Thus, the needed energy (work) to charge the DC-link capacitor from the battery voltage to the DC-link reference voltage is given by:

$$\Delta U = \frac{1}{2}C_{dc,ref}\left(V_{dc,ref}^2 - V_{batt}^2\right) \tag{4.6}$$

This work must be done by the prime mover (mechanical shaft) of the induction generator, during the charge-up time. The generator control must be proper so the generator is supplied with sufficient reactive power during charging.

A high capacitance will give a stable DC-voltage. Thus, the system becomes more resilient to sudden changes in the generation and/or load consumption. The loaded DC-link capacitor together

with the rotating shaft (its inertia) make up two separated "storages" of energy. The energy stored in the capacitor (equation 4.5) has an analogy in the energy stored in the rotating mass, given by:

$$E = \frac{1}{2} J\omega^2 \tag{4.7}$$

where J is the moment of inertia and ω is the angular velocity.

Another consideration regarding the DC-link capacitor is the DC-voltage ripple, ΔV_{dc}. In [27], equation 4.8 is used for proper dimensioning of the DC-link capacitor.

$$C_{dc} = \frac{i_c}{\Delta V_{dc} f_{sw}} \tag{4.8}$$

The author of [27] argues that keeping capacitance low increases the power density of the converter, since the capacitor can take up to 50% of the total converter volume. Even though power density is an important consideration for electrical vehicles, it is not crucial for this case. The capacitance of the DC-link capacitor is set such that it can store an energy amount corresponding to what the generator delivers within 0.1 s at rated operation. This will give a stable DC-voltage for most operation conditions.

$$C_{dc} = \frac{0.1 P_g}{\frac{1}{2} V_{dc,ref}} \tag{4.9}$$

Battery

A battery is used to get an initial DC-voltage during start up of the system. The battery must be able to deliver a high current for a short period. Conventional car batteries are designed to give such large currents for a short time. After the DC-link capacitor is loaded and the excitation of the induction generator has started, the battery should be removed. This is because the process is self-propelled and only need an initial voltage for start-up. In addition, the battery needs to be protected from the high DC-link voltage that builds up, which potentially could damage the battery over time. Car batteries at voltages in the range of 10-60 V is suitable for this purpose. In this case the battery voltage, V_{batt}, is set to be 40 V. In the Simulink model, the functionality of the battery is included by setting the initial voltage of the DC-link capacitor to V_{batt}.

5 Gate-Signal Generation for 2L-3Φ VSC

A *2-level 3-phase voltage source converter* (2L-3Φ VSC), contains six switching devices. It has an upper and a lower switching device for each phase: [A_u, A_l, B_u, B_l, C_u, C_l]. Usually, the off and on states are represented by gate signals 0 and 1, respectively. These six discrete gate signals are the final outputs from the control system that are fed into the gate drivers of 2L-3Φ VSC. This chapter will introduce some methods used to generate those signals from the outputs of the control system algorithms. The methods discussed are *sinusoidal pulse width modulation (S-PWM)* and *hysteresis based switching*. In addition to a brief discussion of the *space vector pulse width modulation (SV-PWM)* method is also included. Ideal switching characteristics in the switching devices (i.e IGBT) are assumed for all three methods.

5.1 Sinusoidal-PWM

Sinusoidal pulse-width modulation (S-PWM) is a commonly used gate signal generation method. Its simple implementation, the S-PWM method is often favored compared to alternatives. For a three phase system; the desired output voltages are described by three sinusoidal voltage waves, 120° displaced. They are obtained based on the modulation index m_a and a frequency reference, f_{ref} given from the control system algorithm. These three reference signals (v_a, v_b and v_c) are then compared to a triangular (carrier) wave signal, v_{tri}. The carrier signal does not need to be an triangular wave, the saw-tooth waveform are among others able to preform the same functionality as the triangular waveform. Figure 5.1 show a triangular carrier wave at frequency f_{tri} = 1 kHz and amplitude 1 pu. The reference waves have an amplitude 0.8 pu and a frequency 50 Hz.

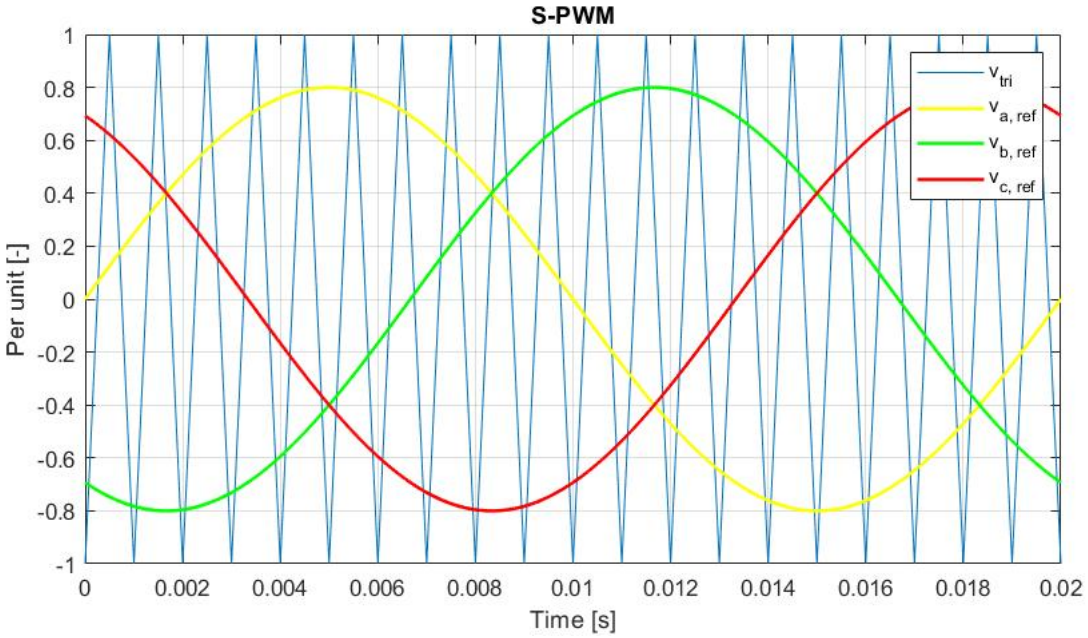

Figure 5.1: Sinusoidal reference waves 120° displaced with amplitude 0.8 pu. The triangular wave (f_{tri} = 1 kHz) has amplitude 1 pu. Thus, m_a = 0.8 and m_f = 20

Within S-PWM the frequency modulation, m_f and the amplitude modulation, m_a are the parameters to be varied to adjust the output performance of the VSC. They are defined by:

$$m_f = \frac{f_{tri}}{f_{ref}} \tag{5.1}$$

$$m_a = \frac{\hat{v}_{ref}}{\hat{v}_{tri}} \tag{5.2}$$

Usually S-PWM is operated with $m_f >> 1$. In the following simulations in this task, m_f is in the range of 100 for S-PWM[1]. Large m_f ($m_f > 21$) is required when f_{ref} is varied. This is since the amplitudes of the sub-harmonics due to asynchronous PWM operation becomes small at large values of m_f and thus allow f_{ref} to vary. [18]. In the V/f-control the variation of f_{ref} is fundamental.

The modulation index m_a can be expressed by the duty cycle. When the reference signal v_{ref} = 1 the duty cycle is 100% (m_a = 1), v_{ref} = 0 corresponds to a duty cycle of 50% (m_a = 0.5) and 0% duty cycle (m_a = 0), corresponds to v_{ref} = -1. These yields for a triangular carrier wave with unity amplitude.

Recall from chapter4.1 that a DC-voltage of V_{dc} is applied to the bridge leg when the upper switch is on. The corresponding phase voltages is obtained by 4.4. The instantaneous phase voltages have five possible output values: $[-\frac{2}{3}V_{dc}, -\frac{1}{3}V_{dc}, 0, \frac{1}{3}V_{dc}, \frac{2}{3}V_{dc}]$. By gradually lowering the duty cycle (m_a), the short time periods where the phase voltages have another value than 0 is reduced. Thus the RMS-value of phase voltage is also gradually reduced.

If m_a is increased above unity, the operation is called over-modulation. Over-modulation is beneficial to increase magnitude of fundamental component of the the phase voltage. However the over-modulation introduces a high amount of harmonic components at lower frequencies. In a view of voltage quality and THD, over-modulation (m_a > 1) should be avoided. S-PWM operation with $m_a \leq 1$ is called linear modulation because the fundamental component of the output phase voltage varies linearly with the modulation index m_a. Square wave operation occurs if the modulation index is increased such that the carrier wave only intersect the reference wave twice per fundamental period. Then the output waves become square shaped and the amplitude of the fundamental component saturates and can not be increased any more.

5.2 S-PWM with 3rd-Order Harmonic Injection

The utilization of the DC-link voltage can be increased by 15.5 % in PWM-operation, by adding a 3^{rd}-order harmonic component to the reference signal. The 3^{rd}-order harmonic component has an amplitude of $\frac{1}{6}$ pu. In the line-line voltage, all triple harmonics in the phase-to-neutral voltage generated by the converter, will be cancel each other out, thus they do not cause any distortion (THD) as over-modulation (m_a > 1) does.

The general formula for the peak value of a signal generated by linear modulation ($m_a \leq 1.0$) is given by 5.3

$$(\hat{V}_{An})_1 = m_a \frac{V_{dc}}{2} \tag{5.3}$$

The RMS-value becomes

$$(V_{An})_1 = m_a \frac{V_{dc}}{2} \cdot \frac{1}{\sqrt{2}} \tag{5.4}$$

[23] shows that the optimal size of the amplitude of the 3^{rd} order harmonic injection is $\frac{1}{6}$ of the fundamental amplitude. The maximums occur at $\frac{\pi}{3}$, $\frac{2\pi}{3}$, $\frac{4\pi}{3}$, $\frac{5\pi}{3}$ and so on.

$$\hat{V}_{An} \cdot (\sin\frac{n\pi}{3} + \frac{1}{6} \cdot \sin\cdot\frac{n\pi}{3}) = \hat{V}_{An} \cdot \frac{\sqrt{3}}{2} = 0.866 \cdot \hat{V}_{An} \tag{5.5}$$

[1] In V/f-control f_{ref} varies around the generator reference.

The maximum value of the reference wave, m_a will be $\frac{\sqrt{3}}{2}$ = 0.866. This allow multiplying the modulation signal with $\frac{1}{\sqrt{3}/2} = \frac{1}{0.866}$ = 1.155 to increase the utilization of the DC-voltage, with linear modulation ($m_a \leq 1$). Linear modulation generates less distortion (THD) in the AC output voltage than the over-modulated case ($m_a \geq 1$). The injected 3^{rd}-harmonic injections are canceled in the line voltage, thus it cause no additional distortion.

The amplitude of fundamental frequency component can represent the peak value of the phase to neutral voltage in the system. An RMS voltage of 230 V (phase to-neutral) gives a peak value at $\sqrt{2} \cdot 230$ V = 325.27 V.

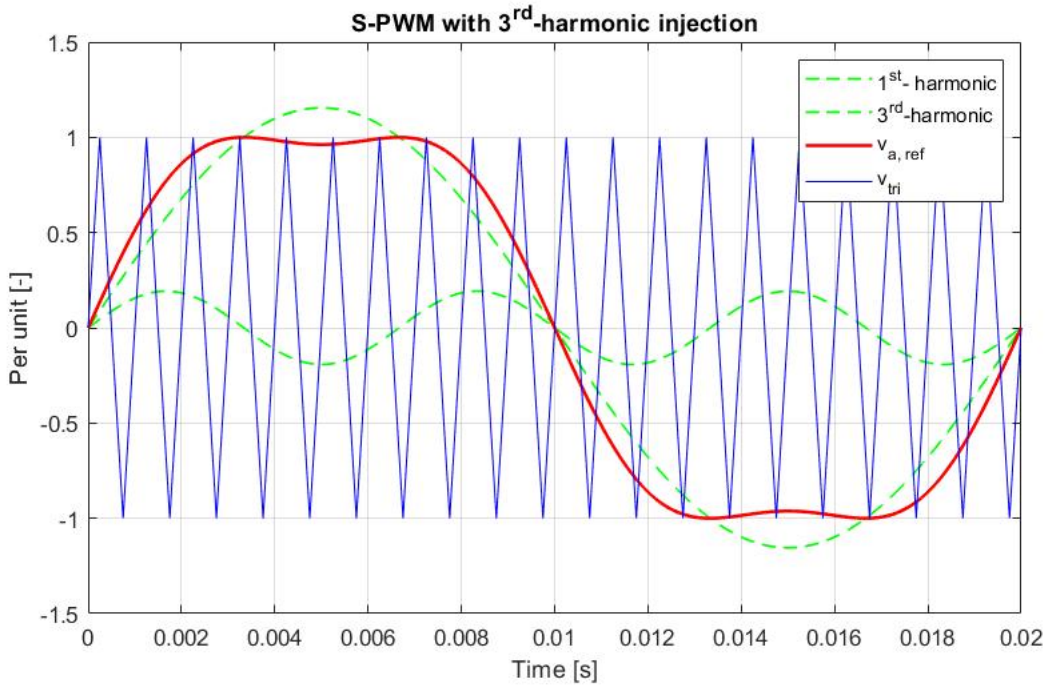

Figure 5.2: Reference signal with 3^{rd}-harmonic injection for phase a. The resulting reference wave (red) is the sum of the fundamental and the 3^{rd}-harmonic components. In this case the fundamental component can have an amplitude of 1.15 pu. f_{tri} 1 kHz. Thus, m_a = 1 and m_f = 20.

Based on this the minimum reference voltage of the DC-link voltage can be determined:

A 2L-3Φ VSC receiving a reference signal m_a will generate an AC voltage at $m_a \cdot \frac{V_{dc}}{2}$. If the modulation is kept linear the peak value of the output voltage will be $\frac{V_{dc}}{2}$. This corresponds to $(\hat{V}_{An})_1$. With a phase voltage at 230 V RMS, this becomes:

$$V_\Phi = m_a \cdot \frac{V_{dc}}{2} \cdot \frac{1}{\sqrt{2}} = 0.354 \cdot m_a V_{dc} \tag{5.6}$$

By using equation 5.6 a DC-voltage at 650 V would have be required to generate a sinusoidal voltage at 230 V RMS phase to neutral. This corresponds to a line-line voltage at 400 V. However by using the third harmonic trick a sinusoidal phase voltage at 230 V can be obtained by a significantly lower DC-link voltage:

The peak of the reference wave reaches $\frac{\sqrt{3}}{2} = 0.866$ related to the fundamental sine wave. By adjusting the pu. reference value axis by a factor $\frac{1}{\sqrt{3}/2} = 1.155$, the peaks at the 3rd harmonic injected signal reaches 1 pu and the fundamental 1.1547 pu as shown in i Figure 5.2. Now the RMS value of the phase voltage in 5.6 can be expressed as 5.7:

$$V_\Phi = m_a \cdot \frac{1}{\sqrt{3}/2} \cdot \frac{V_{dc}}{2} \cdot \frac{1}{\sqrt{2}} = \frac{1}{\sqrt{6}} \cdot m_a V_{dc} = 0.408 \cdot m_a V_{dc} \tag{5.7}$$

Thus the required value for V_{dc} is 563 V. Due to some small voltage drop in the system the reference DC-link voltage has been set to 563 V. The voltage drop across the LCL-filter is negligible. The load side VSC delivers sinusoidal line-line voltages at 400 V to the load and since the ground/neutral point of the load is isolated form the neutral at the VSC no 3rd harmonics appear in the load side AC-system.

In [23] it i proved that the best utilization of the DC-link voltage while inverting to sinusoidal AC voltage is using a 3^{rd}-harmonic component at one sixth of the fundamental amplitude.

5.3 The RMS/DC-Method: RMS-Voltage in S-PWM

In S-PWM, the discrete voltage steps that makes up the phase voltages, generated by the VSC, can be used estimate the RMS-value of the resulting phase voltage, v_Φ. Instead of using the general (continuous) definition of the RMS-value, this can be done by using a discrete integral as a definition of the RMS-value:

$$v_{\Phi,rms} = \sqrt{\frac{\Delta t \cdot \sum_{i=1}^{i=n_{samp}} v_\Phi^2}{\Delta l \cdot n_{samp}}} \tag{5.8}$$

where n_{samp} is the total number of samples, Δl is the time between each sample and Δt is the total time of fundamental period. In [1], the discrete integral in 5.8 has been used to determine the RMS-voltage for different values of m_a in the range between 0 and 2. Figure 5.3 (taken from [1]) shows the modulation index, m_a, as a function of the resulting RMS-voltages. For $m_a \leq 1$, the relationship

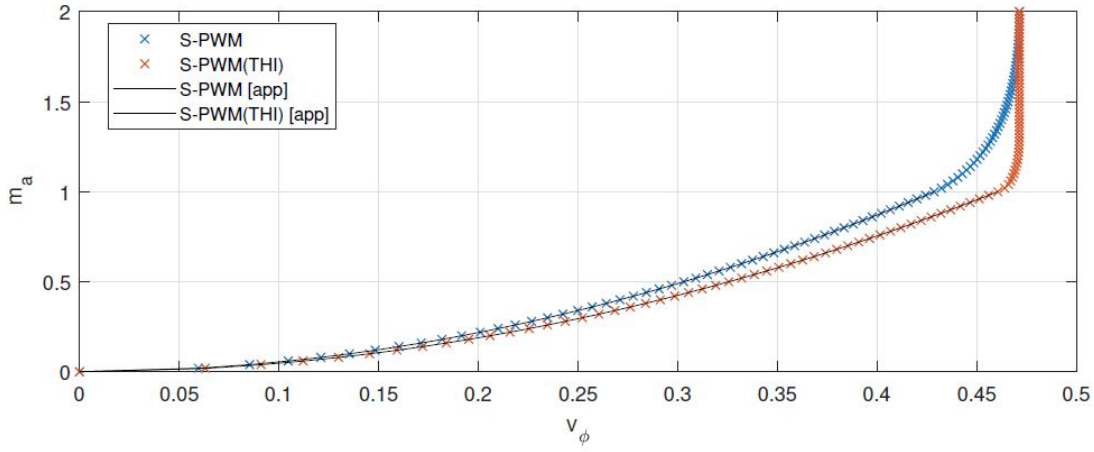

Figure 5.3: m_a as a function of v_m for S-PWM controlled 3Φ-2L VSC. Figure 6.8 in [1].

expressed can be as a 2^{nd}-order function at the form given in equation 5.9:

$$m_a = \mu_{ma} \cdot v_\Phi^2 \tag{5.9}$$

where $0 \leq v_\Phi \leq v_m$ is the limitations for the area called "linear modulation" (i.e. v_ϕ is the RMS-voltage at $m_a = 1$) [18]. In the over-modulation range, the RMS-value of the phase voltage will slightly increase before it saturates when square-wave operation is achieved. There have been determined values by regression for v_m and μ_{ma} for S-PWM and 3^{rd}-harmonic injection S-PWM:

- S-PWM: $v_m = 0.4287$ and $\mu_{ma} = 5.442$
- 3^{rd}-harmonic S-PWM: $v_m = 0.4606$ and $\mu_{ma} = 4.714$

These parameters are used in the voltage controller of the V/f-controller (Section 9) to keep the modulation index $m_a \leq 1$. Thus over-modulation and in worst case square-wave operation of the induction generator voltage is avoided.

The advantage of S-PWM with 3^{rd}-harmonic injection, in terms of increased utilization of the DC-voltage is seen in Figure 5.3. in addition to the value of V_Φ.

5.4 Implementation of S-PWM

The functionality of the S-PWM method is obtained in the Simulink model by Matlab function blocks as seen in Figure 5.4. The functionality of these block are appended in G.2 and G.3. The left block generates the three reference signals (sinusoidal or as here with 3^{rd}-harmonic injection) and are compared to the triangular carrier wave in the right block to obtain the six gate signals needed for VSC.

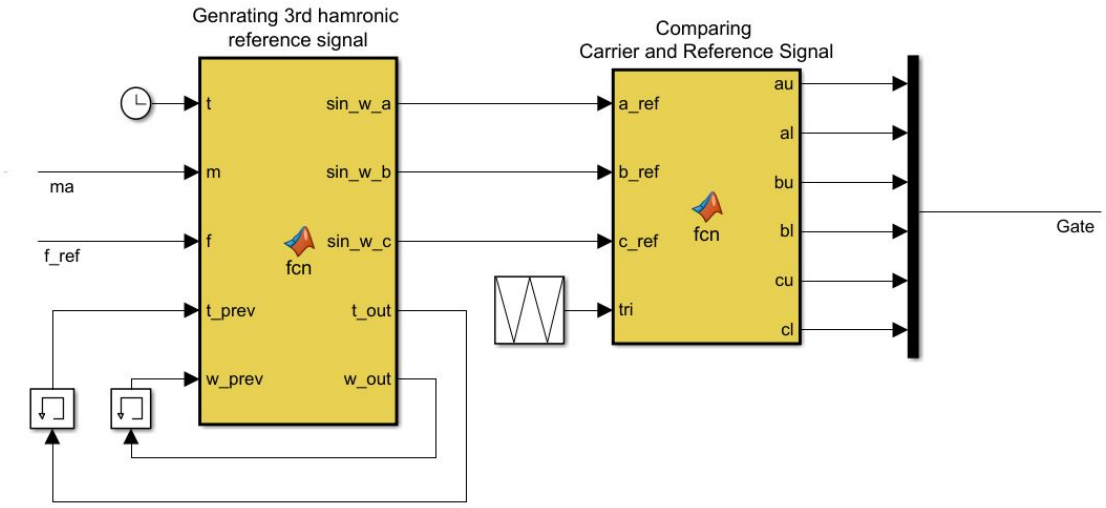

Figure 5.4: MATLAB function blocks are used to implement S-PWM with 3^{rd}-harmonic injection into the model and generate gate signals.

5.5 Hysteresis Based Switching

The hysteresis control receives an input signal and can provide two binary output states, h_{out}: On and off or 1/0. The principle is based on a input signal, h_{in} that is compared with an upper limit, h_u and a lower limit, h_l. If the input is increasing above the upper limit: $h_{in} \geq h_u$, the output switches off (0). Similar if the input drops below the lower limit: $h_{in} \leq h_l$, the output turns on (1). The difference between the upper and lower limit is called the band gap of the controller: $h_{gap} = h_u - h_l$. Thermostats usually use hysteresis control to control the temperature within a band gap given by an upper and a lower temperature reference: The heater turns on when the temperature drops below the

lower limit and stay on until the temperature rises to the upper limit where it is turned off.

In a similar manner as for thermostats, the binary output of a hysteresis controller can be used to generate binary control signals for VSCs. For a 3Φ-2L-VSC three hysteresis loops are need to generate the total of six gate signal for the 3Φ-2L-VSC. Figure 5.5 shows the control structure: The reference current (from IVC) and instantaneous measured stator currents are compared for each phase. The current error are fed into the hysteresis controller as the input signal, h_{in}. The band gap of the controller are centered around 0 and has upper and lower limits at $\frac{h_{lim}}{2}$ and $-\frac{h_{lim}}{2}$ respectively. When the current error increases above $\frac{h_{lim}}{2}$ the lower switch turns on and if it drops below $-\frac{h_{lim}}{2}$ the upper switch turns on. The a switch turns on a positive neutral voltage will be applied on the phase leg and increase the phase voltage. An increased phase voltage in turn will increase the current and lower the current error. A similar argumentation can be done for the lower switch and the decrease in current.

In Figure 5.5 the current errors are fed into Sample and hold blocks to achieve an upper switching frequency $f_{sw,IVC}$ for the hysteresis controller. Thus the error signal becomes discrete. The current error is compared to the hysteresis band gap in the Relay block. At the upper limit the output is set to 0 and and the lower limit the output is set to 1. This signal is the upper gate signal. The lower gate signal is set to 1 when the upper 0, and set to 0 when the upper signal is 1. This is done for all three phases to achieve the six gate signals.

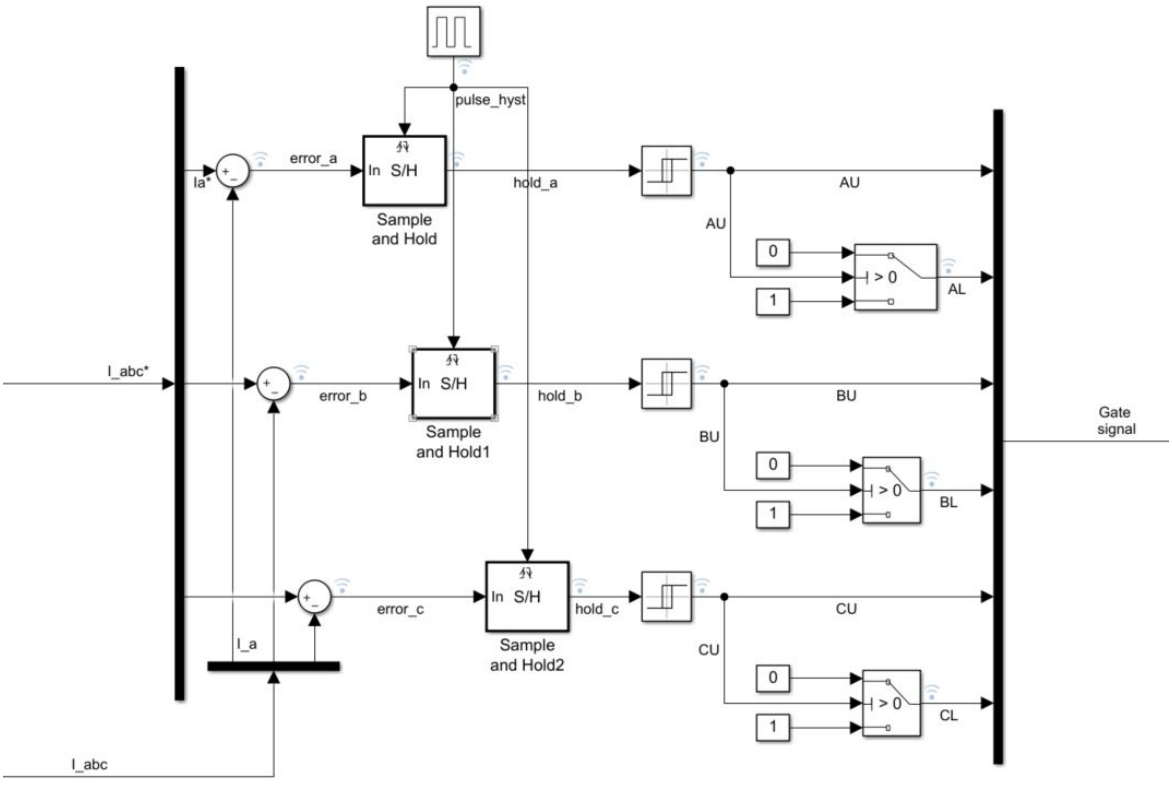

Figure 5.5: Inner structure of current hysteresis controller.

5.6 Space Vector-PWM

Space Vector Pulse Width Modulation SV-PWM is among the today standard methods for gate signal generation for converters. As the name indicates it uses the concept of space vectors (dq-

transformation) of the voltages. This is done by controlling the possible output states to imitate the reference vector. Due to simplicity in the model implementation, the S-PWM generation is favored, hence SV-PWM is not discussed any further in this thesis.

6 Passive Filter

One of the goals of this task is to obtain high voltage quality which means a smooth sinusoidal shaped voltage at a given RMS-value. The load side VSC generates discrete voltage signals at magnitudes $\pm\frac{2}{3}V_{dc}$, $\pm\frac{1}{3}V_{dc}$ and 0 in accordance with 4.4. The variable harmonic content is high and varying. Some types of electric loads are fragile to these harmonics and require a high quality voltage supply. The Norwegian grid requirements [4] are used to define high quality voltage in terms of total harmonic distortion and voltage deviation. Active and passive filters can be useful to filter out these harmonics. Passive filters are simpler than the active filters and consequently cheaper and favorable for this simple purpose. In addition the passive filter does not need any control system. The passive filters contains reactive components (capacitors and inductors) at an fixed impedance designed to obtain good performance at rated load conditions. The reactive components produces a voltage drop across the filter. Thus the load side VSC voltage needs to be somewhat higher than the desired load voltage.

There exist several types and configuration of passive filters. Among them are L-, LC- and LCL-filters. In general LCL-filters obtains better performance for lower components values that makes the filter cheaper and more compact. Thus the LCL-filter topology has been chosen to be used as filter here. Figure 6.1 shows the structure of a 3 Φ LCL filter. The capacitor branches are damped with an resistor R and Y-connected to ground.

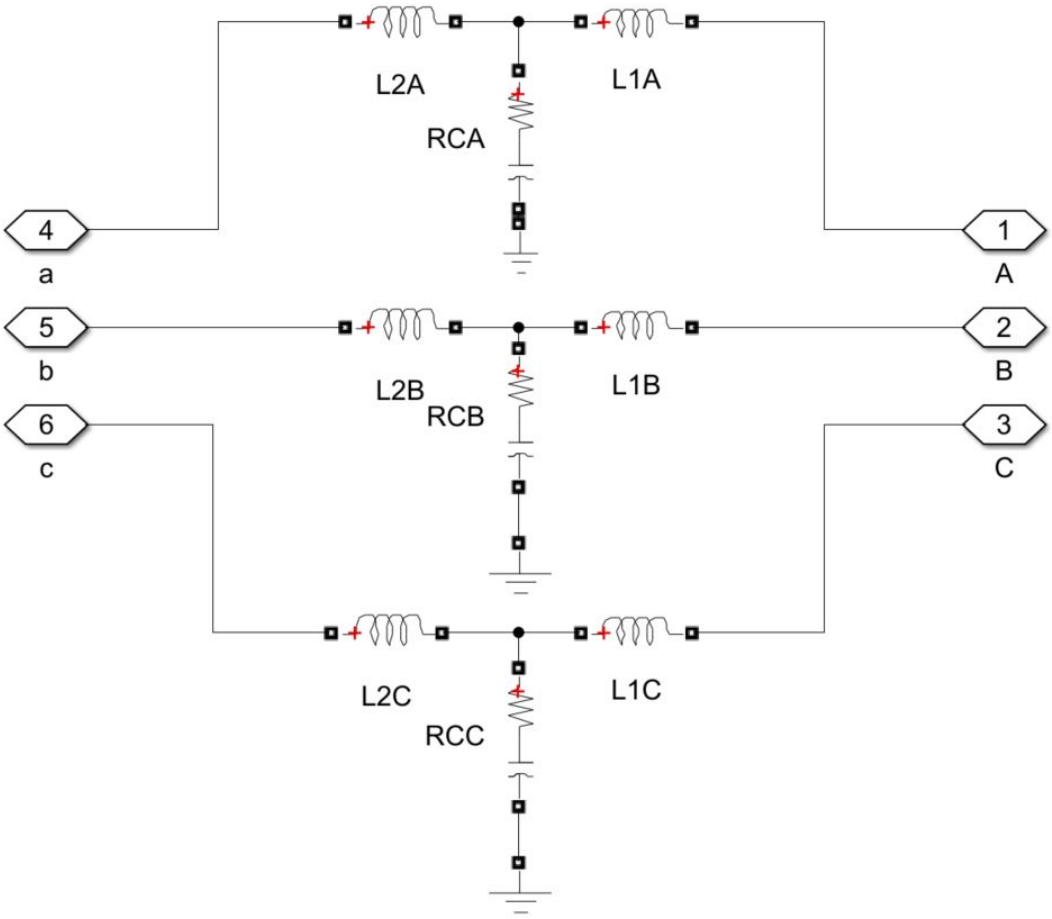

Figure 6.1: Circuit diagram of 3Φ-LCL passive filter

The MATLAB-script in Appendix G.1 is based on a design procedure for passive LCL-filter in *LCL filter design and performance analysis for small wind turbine systems* [24]. The filter design procedure become independent of the turbine type. [24] is used to determine the component values of the LCL-filter: L_1, L_2, C and R. Those are showed Table 6.2 for rated load. Where L_1 is the grid side inductor and L_2 is the VSC-side inductor, C is the capacitor and R is the damping resistor. The MATLAB-script takes the rated apparent power $S_{n,load}$, grid frequency f_{grid}, switching frequency,f_{sw} the DC-link voltage, $V_{dc,ref}$ and the load phase voltage $V_{\Phi,grid}$ as inputs (Table 6.1). The filter is designed for optimal performance at a leading power factor at 0.81 and apparent load at 1.851 kVA. The maximum current ripple is set to 5 % of maximum rated load current and is a basis for design of the grid side inductor L_1, DC-link voltage and switching frequency:

$$L_1 = \frac{V_{DC}}{6 f_{sw} \Delta I_{L,max}} \tag{6.1}$$

The script determines the capacitance, C based on the base capacitance C_b and the power factor variation seen from load $x = 0.05$:

$$C = x \cdot C_b \tag{6.2}$$

Further the script determine the ratio r between the L_2 and L_1 by iteration (see G.1). The resonance frequency, f_{res} must be checked by the constraints:

$$10 \cdot f_{grid} < f_{res} < \frac{f_{sw}}{2} \tag{6.3}$$

It is the angular resonance frequency, $\omega_{res} = \sqrt{\frac{L_1+L_2}{L_1 L_2 C}}$ and the capacitance, C that determine the damping resistor used to avoid resonance. The damping resistor is determined by:

$$R = \frac{1}{3 \cdot \omega_{res} C} \tag{6.4}$$

Table 6.1: Inputs to the passive filter design procedure

$\mathbf{S_n}$	$\mathbf{f_{grid}}$	$\mathbf{f_{sw}}$	$\mathbf{V_{dc,ref}}$	$\mathbf{V_{\Phi,grid}}$
S_{base} = 1.851 kVA	50 Hz	5 kHz	565 V	$\frac{400}{\sqrt{3}}$ V = 230.9 V

Table 6.2: Component values in passive LCL-filter and resonance frequency

$\mathbf{L_1}$	$\mathbf{L_2}$	$\mathbf{C}$	$\mathbf{R}$	$\mathbf{f_{res}}$
19.14 mH	1.277 mH	4.815 μF	5.255 Ω	2.097 kHz

7 Variable Load

The maximum load is demand is set to be 1.5 kW for the isolated system. A pure resistive load with unity power factor is assumed to be the loading. However the power factor can also be leading or lagging by including inductors and/or capacitors in the load structure. It should be possible to vary the resistive load demand during the simulation. The input signal R_{load} determine the value of the three variable resistors as seen in Figure 7.1. Figure 7.2 shows that a high shunt resistor have been necessary in the model. This is since modeling of the non-linear element such as the variable resistors are done by using current sources (i.e. the Norton Equivalent).

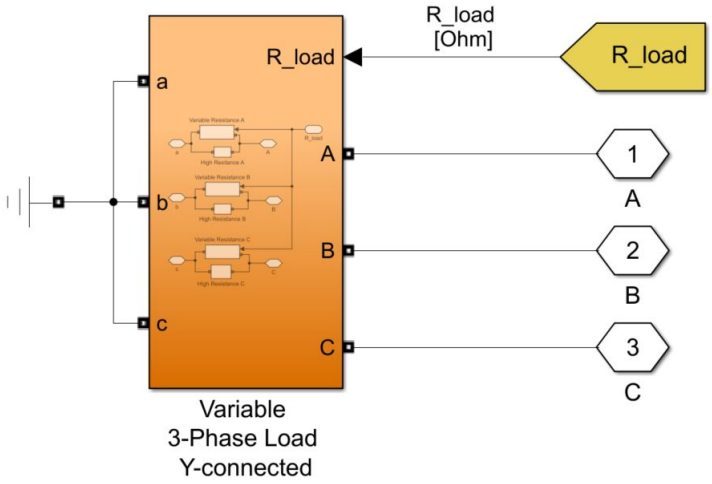

Figure 7.1: The load is a Y- connected balanced 3Φload

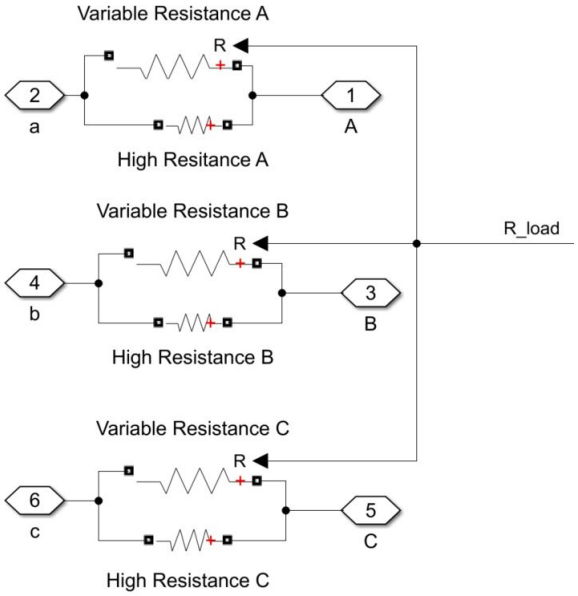

Figure 7.2: Inner structure of pure resistive load

To obtain a varying load demand between 0 and 1.5 kW, a programmed load profile is used. This

profile outputs the desired value of the three Y-connected resistors than together consumes the load demand at rated load voltage. The load profile is programmed with some load steps, sized in per unit of 1.5 kW and step times for when these load steps occurs. The structure of generation is shown in Figure 7.3:

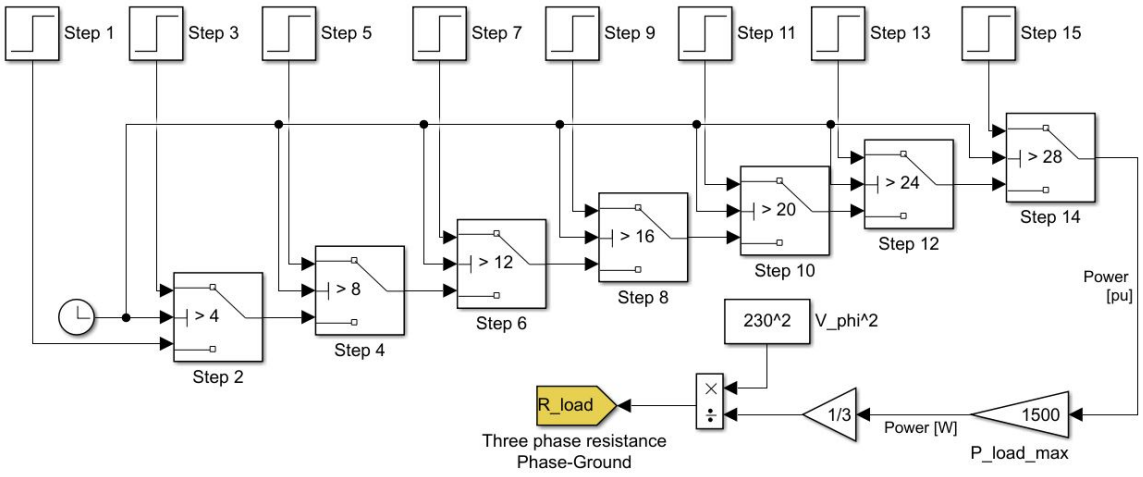

Figure 7.3: Structure of generation of load steps by adjusting the load resistor

When only the generator side characteristic are considered in the model (i.e Test 3), an equivalent DC-load resistor connected to the DC-link to make an easy modeling of the loading. Its variable resistance value is determined in a similar way as depicted in Figure 7.3. Then the voltage used is the DC-link voltage and only one variable resistor is used, thus the gain of $\frac{1}{3}$ is omitted.

The Norwegian quality requirements for low voltage grids are voltage drop 230 V ± 3% RMS voltage and total harmonic distortion, THD < 5%. They are given in *Forskrift om leveringskvalitet i kraftsystemet* [4] and are set to be yielding for the load voltage in the isolated system. These requirements are very strict and yields for low voltage grid connected systems in Norway that is a well developed country. If the equipment supplied by the isolated system is not very fragile to voltage quality, a consideration of the benefits obtained by reducing the requirements can be done. Some trade offs between cost and voltage quality and stability needs to be taken in the design process for each power plant. When designing a plant (isolated system) for operation in rural areas in a developing country, low costs is favored instead of high requirements of voltage quality. Hovever this Thesis will show that the strict Norwegian requirements are possible to be met when a squirrel cage induction machine is the generating unit.

The total harmonic distortion (THD) in terms of RMS-voltage is in [18] given by:

$$THD = 100\% \cdot \frac{\sqrt{V_s^2 - V_{s1}^2}}{V_{s1}} \tag{7.1}$$

where V_s is the RMS-value of the waveform voltage and V_{s1} is the RMS voltage of the fundamental voltage component. A similar relationship exist for harmonic distortion in the current.

8 Control Techniques of Squirrel Cage Induction Machines

The use of power electronics converters to achieve a desired performance of an induction machine is widely outstretched for most usages of induction machines. The power electronic and its control systems are used to obtain desired operation within the limitation of the induction machine. In motoring mode, the power electronics such as back-to-back arrangements can be used as frequency converters in order to obtain a desired mechanical speed, different from what is obtained by applying the frequency at 50 Hz (or 60 Hz) to the induction machine terminals. The supply of reactive power to the induction machine can also be accommodated by a proper control. In generator operation of the machine utilization of these two advantages is favorable, thus a back-to-back converter arrangement is suitable for the desired application. In the following sections the ratings and limitations of induction machines are discussed followed by a theoretical introduction of three common control techniques for induction machines. They are: Scalar control (V/f-method), direct and indirect vector control (DVC and IVC) and direct torque control (DTC).

8.1 Rating and limitations of SCIMs

All electrical machines have ratings and limitations in voltage and currents. The main constraint in the voltage rating of a machine is its insulation. A to high voltage can in worst case lead to breakdown within the machine coils. The current constraints is related to overheating of the coils (due to losses) and to magnetic saturation [1]. The efficient use of the current in an induction machine to achieve torque decreases as the machine saturates. Thus most induction machines designs have nominal operation close to the saturation point. The power electronic converters do also have limitations in voltage and current. The conducting losses and switching losses (related to the switching frequency, f_{sw}) of the power converter are important considerations in the power converter design. If the power converter limitations conflicts the limitation of the induction machine, these limitations must also be considered in the control system.

Within a rotating induction machine interaction between the magnetic fields develops a mechanical torque, τ_m on the shaft (motor operation), or it convert the external applied torque into an electric torque τ_e (generator operation). The magnetic fields are produced by the rotor and stator currents. In the simplest models the magnetic saturation is often neglected. In those cases the magnetic fields are assumed to vary in proportion to the fixed machine inductance. However this is a great simplification: Figure 3.4a shows the unlinear relation between terminal voltage and the magnetization current, I_m. This is due to the magnetic saturation in the stator and rotor iron, which makes the magnetization reactance, X_m as a function of the machine's operating state [i.e. voltage and current]. Figures 3.6 and 3.5 show this great variation of the magnetizing inductance, X_m within the operating range of the investigated 1.5 kW SCIM.

9 Scalar control (V/f-method)

Scalar control is a very popular control technique for pumping and other low-cost industrial applications. This is because the scalar control technique is easy to implement and thus cheap, even though it has an inferior performance for some applications compared to alternative control schemes. In the recent years, the more superior vector control, has become price competitive to the scalar controlled V/f-method. The V/f-control is based on a principle of keeping the flux linkage, λ_m, constant. This is achieved by adjusting the voltage to keep the V/f-ratio constant as the frequency varies.

The main constraint of using scalar control for induction motors and generators is related to the machine's transient response. The torque and speed vary slowly for most cases of hydro power (and wind power) applications. Thus, scalar control works appropriately for these types of induction generators. This is since the mechanical dynamics (speed and shaft torque) are bandwidth-limited (due to water inertia and limitations in gate speed etc.) the torque varies relatively slow. If these variations are within one hundredth of a milliseconds and up to a second, the scalar control (V/f-method) works appropriately [16].

9.1 Principal Background

Simones and Farret have in [16] used a steady state two inductance per-phase equivalent circuit of the induction machine as a theoretical background for understanding the scalar control method. The two-inductance equivalent circuit can be a Γ-stator or a Γ-rotor equivalent circuit. The two models are related to the ordinary per phase equivalent by the transformation coefficients $\gamma = \frac{X_s}{X_m}$ and $\rho = \frac{X_m}{X_r}$, respectively. In the literature, the Γ-stator and the Γ-rotor equivalents are also referred to as Γ-equivalent and inverse Γ-equivalent circuits.

In the Γ-stator equivalent, the effects of the stator resistance, r_r are usually neglected. Further, the stator leakage reactance, X_{ls} is included in the resulting rotor reactance, $X_{l,\gamma}$, as shown in Table 9.1. The other parameters used in the following derivation are also given in Table 9.1.

Table 9.1: Γ-stator equivalent parameters referred to stator

Rotor resistance	$R_{r,\gamma} = \gamma^2 R_r$
Magnetizing reactance	$X_{m,\gamma} = \gamma X_m = X_s$
Total leakage reactance	$X_{l,\gamma} = \gamma\ X_{ls} + \gamma^2 X_{lr}$
Rotor current	$I_{r,\gamma} = \frac{I_r}{\gamma}$
Rotor flux	$\lambda_{r,\gamma} = \gamma \lambda_r$
Angular velocity of rotor currents (Rotor frequency)	$\omega_r = s\omega_e$
Rotor angular frequency	$\omega_r = \frac{p}{2}\omega_{sl}$

The stator flux linkage, λ_s, is approximated by the air-gap flux linkage, λ_m, in the Γ-stator equivalent model. The equivalent parameters in Table 9.1, together withe the basic and well known expression 9.1 for the resultant air-gap flux per pole for an induction machine, form the basis of V/f-control.

$$\Phi_m = \frac{1}{4.44 K_{w1} N} \cdot \left(\frac{V}{f}\right) \tag{9.1}$$

where K_{w1} is a stator winding factor and N is the number of turns per pole. There is a linear relationship between the air-gap flux, Φ_m, and the air-gap flux linkage, λ_m, given by:

$$\lambda_m = N\Phi_m \tag{9.2}$$

The flux linkage is kept constant during operation of the SCIM, to avoid magnetic saturation and hence a sharp increase in the magnetizing current. It is seen from equation 9.1 and 9.2 that the flux linkage, λ_m, is proportional to the ratio $\frac{V}{f}$. V_0 and f_0 are the nominal terminal voltage and frequency of the induction machine respectively. It gives constant ratio $\frac{V_0}{f_0}$. For any frequency, f, an applied terminal voltage of V will give the desired operation that keeps the V/f-ratio constant:

$$V = \left(\frac{f}{f_0}\right) \cdot V_0 = \left(\frac{\omega_e}{\omega_{e,0}}\right) \cdot V_0 \tag{9.3}$$

The rotor current in the Γ-equivalent model can be expressed by:

$$|I_{r,\gamma}| = \frac{\lambda_m}{R_{r,\gamma}} \cdot \frac{\omega_r}{\sqrt{(T_r\omega_r)^2 + 1}} \tag{9.4}$$

where the time constant is $T_r = \frac{X_{l,\gamma}}{R_{r,\gamma}}$ and $X_{l,\gamma}$ is the total leakage reactance of the circuit. When the resistive rotor losses ($3I_{r,\gamma}^2\ R_{r,\gamma}$) are neglected, the converted power, P_{mech}, can be expressed by:

$$P_e = 3R_{r,\gamma}\frac{\omega_e}{\omega_r}|I_{r,\gamma}|^2 \approx P_{mech} \tag{9.5}$$

When inserting equation 9.4 into equation 9.5 and using the fact that the angular shaft speed is leading the stator electrical frequency by $\omega_m = \frac{1}{p_p}\omega_e(1 + s)$ when applying scalar control. The shaft torque, τ_e is given by:

$$\tau_e = \frac{P_{mech}}{\omega_m} \approx 3p_p\frac{\lambda_m^2}{R_{r,\gamma}} \cdot \frac{\omega_r}{(T_r\omega_r)^2 + 1} \tag{9.6}$$

The machine will operate slightly above the synchronous speed, ω_s, in generator operation and slightly below in motor operation. Thus, the operational slip will be well below the critical slip, s_{max} which gives the pullout torque. In that case the denominator of 9.6 ($(T_r\omega_r)^2 + 1$) will approximate to unity. This will make the torque virtual proportional to the rotor frequency for constant flux [16]. Transferring 9.6 back to the induction machine model in Figure 3.1 (called the T model) and considering that the flux is $\lambda_m = \frac{V_s}{\omega_e} = const$, the torque is given by:

$$\tau_e = 3p_p \cdot \frac{1}{R_r}\lambda_m^2\omega_{sl} \tag{9.7}$$

Equation 9.7 shows that for a fixed V/f-ratio (constant λ_m), there is one characteristic torque speed curve. The stator frequency, ω_e, that determines the torque crossover frequency (i.e. synchronous speed of the operating state). The constant flux gives a high utilization of the stator and rotor iron in addition to a high torque per stator ampere. In the above discussion the stator resistance and magnetic saturation are neglected, but in the real 1.5 kW induction machine these considerations will have a great effect on the induction machine performance. The stator resistance will oppose the terminal voltage in motor operation. In generator operation, the reversed voltage will create an increased back-emf with increased air-gap flux. This gives an initial increase of the torque when the speed is reduced [16].

9.2 Implementation of V/f-control-scheme

The fundamental objective of scalar control is to control the slip operation, ω_{sl}, in such a manner that it maintains the DC-voltage at the reference level. The overall V/f-control scheme is depicted in Figure 9.1. The *slip-speed controller* uses the DC-voltage, V_{dc}, as an input to determine the commanded slip speed, $\omega_{sl}*$. The commanded slip speed, ω^*_{sl}, determines how much torque the induction machine extracts from the prime mover as seen in equation 9.7.

Table 9.2: Inputs and outputs of the V/f-controller

Inputs (5) **from measurements**	**Outputs (2)** **to S-PWM with THI**
DC-link voltage, V_{dc} Mechanical shaft speed, ω_r Stator currents, i_{abc} (3)	Modulation index, m_a Electric frequency reference, f_e

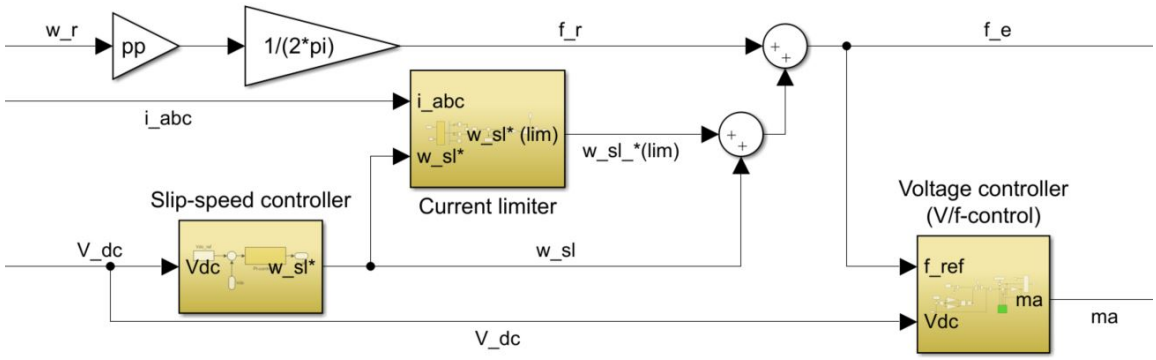

Figure 9.1: Schematic structure of V/f-controller. Based on V_{dc}, ω_r and the stator currents, it calculates the modulation index, m_a and frequency reference, f_{ref}.

The *Current limiter* is included to avoid excessive stator currents and has the opportunity to reduce ω^*_{sl} if needed. The commanded electrical angular frequency, ω_e, is given by $\omega_r p_p + \omega_{sl}$. A modulation index, m_a, is determined by the *Voltage controller*. It tries to maintain the RMS-voltage such that the V/f-ratio remains constant, based on the electrical frequency, f_e (which depends on ω_{sl} and ω_r). An overview of the inputs from measurements to the V/f-controller and the outputs from the V/f-controller to the S-PWM, is shown in Table 9.2

9.2.1 Slip-speed controller

The slip-speed controller contains a PI-controller, which based on the DC-voltage error gives the commanded slip speed, ω_{sl}^*. The integrator and output of the PI-controller is limited to a lower and an upper slip speed $\omega_{ls,l}$ and $\omega_{ls,u}$, respectively.

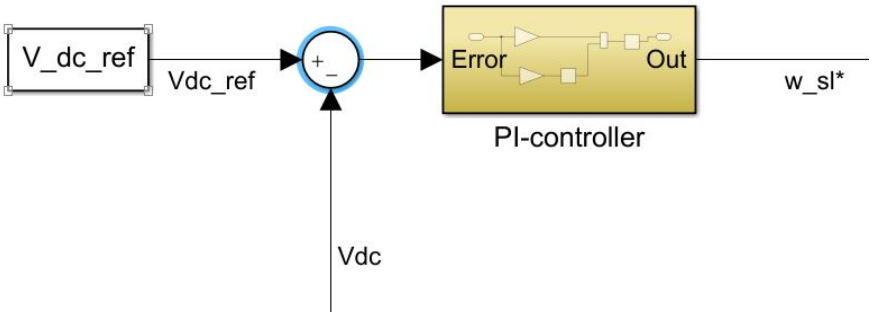

Figure 9.2: Inner structure of slip-speed controller. A reference slip speed ω_{sl} is calculated based on the instantaneous DC-link voltage error.

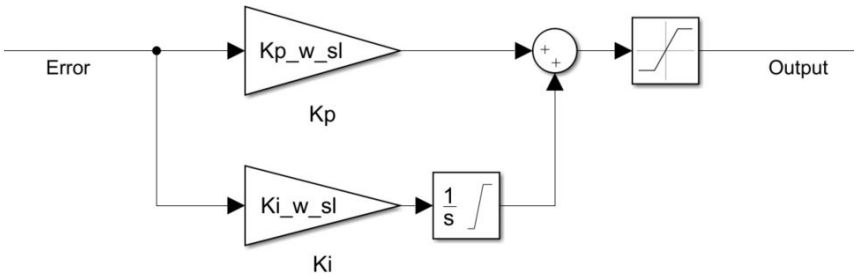

Figure 9.3: Inner structure of limited PI-controller used in slip-speed controller.

9.2.2 Current limiter

The current limiter uses the park-transformation to obtain the peak value of the instantaneous measured stator currents, i_{abc}. This value is compared to the rated peak value of the induction machine, i_{max}, and fed to an integrator with an upper limit 0 and a lower limit -1. The limited output of the integratoris multiplied with the commanded slip speed, ω_{sl}^*, to obtain the commanded slip speed reduction.

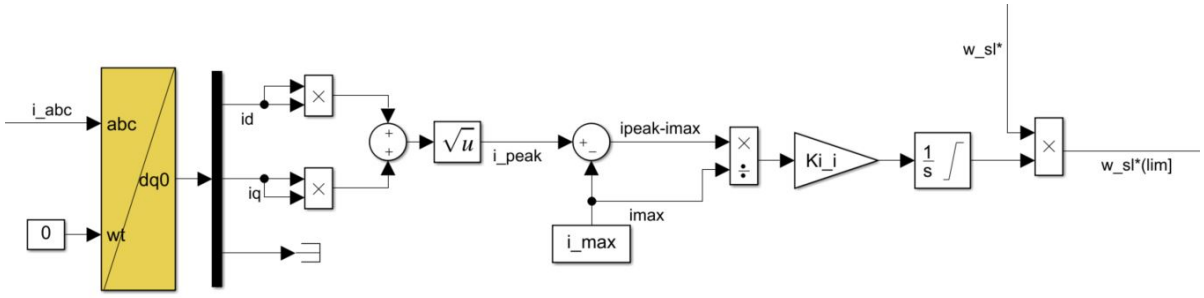

Figure 9.4: Inner structure of current limiter. The current limiter calculates any reduction of the slip-speed reference if the stator currents are excessive.

reduction. If the stator currents become excessive, the integrator reaches -1 and thus the commanded slip speed is reduced by $-\omega_{sl}^{*}$. When the stator currents are kept within the rated range, the integrator works toward zero and there is no adjustment of the commanded slip speed.

9.2.3 Voltage controller

The voltage controller uses the nominal V/f-ratio $\left(\frac{V_{nom}}{f_{nom}}\right)$ as a basis for determining the voltage of the SCIM, V_{gen}. V_{gen} is according to equation 9.4 based on the frequency reference, f_{ref}, which is given by the slip speed and the mechanical speed. The modulation index, m_a, is determined by normalizing the desired phase voltage to the DC-voltage and using the RMS/DC-method described in Section 5.3. The modulation index is achieved by using 5.9. To avoid over-modulation, m_a is set to unity if the normalized phase voltage $\left(\frac{V_{gen}}{V_{dc}}\right)$ increases above $\hat{v}_m$. (Called norm_rms_max in Figure 9.5.)

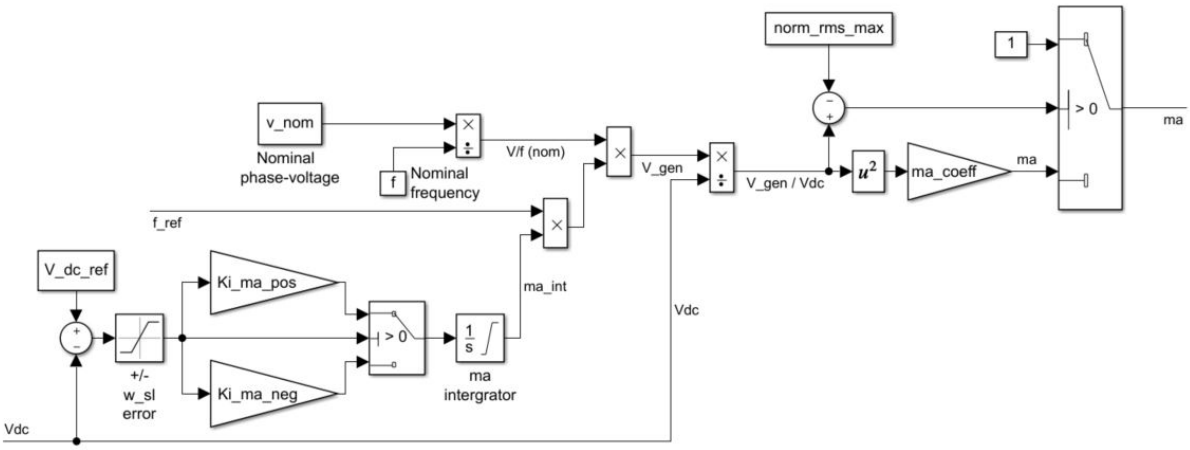

Figure 9.5: Inner structure of the voltage controller. The voltage controller calculates the modulation index, m_a, mainly based on the frequency reference, f_{ref}.

Figure 9.5 also includes the functionality of scaling the frequency reference, based on the DC-voltage deviation. The DC voltage deviation is limited by the upper and lower integrator limits used in the slip speed PI-controller. Whenever the DC-voltage error is positive (i.e DC-voltage is below its reference), the positive gain $K_{i,ma,pos}$ is used to scales the value up towards the upper integrator limit $K_{i,ma,u}$. When the DC-voltage exceeds its reference, the error becomes negative and the integrator uses the negative gain $K_{i,ma,neg}$, to scale the value toward the lower limit, which is set to unity. This scaling of the frequency reference is motivated by the following fact: The torque and power generated by an induction generator, supplied by rated voltage and frequency from a sinusoidal source, is compared to the operating of the same induction generator controlled by a VSC operating at the same RMS-voltage and frequency to keep the V/f-ratio constant. The torque produced will be less (in absolute value) for the VSC supplied generator. Thus, scaling up the frequency reference for a VSC-controlled induction generator allows the system to apply a higher RMS-voltage and thus utilize more of the potential of the generator.

The V/f-controller has a reference frequency and a modulation index, m_a, as output, which are fed into the S-PWM converter. The S-PWM converter generates the six gate signals fed to the 2L3Φ VSC. SV-PWM could also have been used to generate the gate signals. The SV-PWM method is

known to have superior performance compared to the S-PWM method. But the S-PWM has been favored in this somewhat inferior V/f-control due to the implementation being much simpler.

9.3 Parameter list

An overview of the fixed parameters used in the V/f-controller is shown in Table 9.3. The values are given for #IM1. The overview of the tuned parameters for V/f-control is shown in Table 12.1 in Section 12.3, where the basis for tuning are discussed.

Table 9.3: Overview of fixed parameters used in V/f-controller.

Name	**Value for #IM1**	**Appears in**	**Description**
p_p	2	V/f-controller	Number of pole pairs
f_{sw}	5 kHz	S-PWM	Switching frequency for V/f-controller
$V_{dc,ref}$	565 V	Slip speed controller	Reference DC-voltage
v_{nom}	$\frac{V_{LL}}{\sqrt{3}}$ = 230 V	Voltage controller	Nominal generator phase voltage
f_{nom}	50 Hz	Voltage controller	Nominal generator frequency
i_{max}	$\sqrt{2}I_n$	Current limiter	Rated generator peak current
$\bar{v}_m$	0.4287	Voltage controller	norm_rms_max (S-PWM)
μ_{ma}	5.442	Voltage controller	ma_coeff (S-PWM)
i_{upper}	0	Current limiter	Upper limit for integrator
i_{lower}	-1	Current limiter	Lower limit for integrator
$K_{i,ma,lower}$	1	Voltage controller	Lower limit for integrator

10 Vector Control

Vector Control is the most common control technique used in many modern electric high performance drives today [16]. Field orientation, decoupling, transvector control and orthogonal control are other commonly used terms for vector control. The technology was first introduced by the Germans Hasse and Blaschke in the 1970's, and today a great variety of derived implementation techniques are available in the technical literature and used in installations. At least two different sub-categories of vector control can be made based on the methodology used to find or estimate the instantaneous flux position, λ, of the induction machine. These two methodologies will be discussed later and are:

- Indirect vector control (IVC): The feedforward method
- Direct vector control (DVC): The feedback method

Vector control has been widely used due to its advantages in dynamic response and high efficiency. Since processors are getting cheaper and faster, the vector control techniques are driven towards further improvement [13, 16, 22].

The principles of vector control or field orientation control uses a Park-transformation which transforms a three-phase AC machine into the dq0-domain. It is in the dq-domain the control is performed. These control principles are discussed in chapter 10.

10.1 Principal Background

When studying field oriented control (FOC) (i.e vector control) for AC machines, an analogy to the DC-machine control scheme can be used: In DC-machine control it is the field current and the armature current that are adjusted to control the torque. The field current produces the magnetic field and the armature current is representing the force applied to the shaft. A greater torque is achieved by aligning the current components perpendicular to each other, in addition to increasing the magnitudes of each of the current components. The mechanical analogy: $\tau = R\ x\ F$, the field current represents the arm length, R, and the armature current represents the perpendicular force, F, used to produce the torque.

The induction machine is described in the dq0-domain by using the Park-transformation E.7 synchronously to the rotor flux, λ_r. A dq0-domain rotating in sync with the rotor flux is achieved by adjusting the angle between the a-axis and the d-axis, θ_d, so that it is in sync with the stator frequency: $\left(\frac{d}{dt}\theta_d = \omega_e\right)$. In Appendix E the mathematical details of the dq0-representation of the induction machine are discussed. The rotor flux alignment is preferred to the stator flux alignment or the resulting air-gap flux alignment, because the rotor flux alignment decouples the flux and torque. Thus, the control system can be designed in a similar way as done for DC-machines.

The voltage equations E.14 and E.15 for the rotor flux oriented dq-model of the induction machine (Appendix E) are repeated here in a compact formate, shown as equation 10.1 and 10.2 respectively.

$$v_{dq,s} = r_s i_{dq,s} + j\omega_e \lambda_{dq,s} + \frac{d}{dt}\lambda_{dq,s} \tag{10.1}$$

$$0 = r_r i_{dq,r} + j(\omega_e - \omega_r)\lambda_{dq,r} + \frac{d}{dt}\lambda_{dq,r} \tag{10.2}$$

The electromagnetic torque is given by 10.3:

$$\tau_e = \frac{3}{2} \cdot p_p \cdot (\lambda_{sd} i_{sq} - \lambda_{sq} \cdot i_{sq}) = \frac{3}{2} \cdot p_p \cdot (\lambda_{rd} i_{rq} - \lambda_{rq} i_{rd}) \tag{10.3}$$

Since the d-axis is aligned with the rotor flux in the rotor flux oriented model, $\lambda_r = \lambda_{r,d}$ and thus $\lambda_{r,q} = 0$. The expression for $\lambda_{r,q}$ in equation E.10, can be used to express the q-component of the rotor current, $i_{q,r}$:

$$0 = \lambda_{rq} = L_m i_{qs} + (L_m + L_{lr}) \cdot i_{qr} \tag{10.4}$$

which can be rearranged to:

$$i_{qr} = -\frac{L_m}{L_m + L_{rl}} \cdot i_{q,s} \tag{10.5}$$

By using the fact $\lambda_{r,q} = 0$, and inserting 10.5 into 10.3, it is found that the electromagnetic torque τ_e is proportional to the q-component of the stator current, $i_{s,q}$:

$$\tau_e = \frac{3}{2} \cdot p_p \cdot \left(\frac{L_m}{L_m + L_{lr}} \right) \cdot \lambda_{rd} \cdot i_{sq} \tag{10.6}$$

By expressing $v_{d,r}$ with the Laplace operator, s

$$v_{rd} = r_r i_{rd} + (\omega_e - \omega_r) \cdot 0 + s \cdot \lambda_{rd} \tag{10.7}$$

the relation: $i_{rd} = -\frac{s\lambda_{r,d}}{r_r}$, can be used in the expression for $\lambda_{r,d}$:

$$\lambda_{rd} = L_m i_{sd} + (L_m + L_{lr}) i_{rd} = \frac{L_m}{1 + s\left(\frac{L_m + L_{lr}}{r_r}\right)} \cdot i_{sd} = \frac{1}{1 + sT_r} \cdot L_m \cdot i_{sd} \tag{10.8}$$

From 10.8 the rotor time constant, T_r, is found:

$$T_r = \frac{L_m + L_{lr}}{r_r} \tag{10.9}$$

The time represented by T_r, is the delay of the rotor flux, λ_{rd}, with respect to i_{sd}. T_r is dependent on the magnetizing inductance, L_m, in addition to the rotor leakage inductance, L_{lr}, and the rotor resistance, r_r. The dependency of these parameters is of importance in indirect vector control of the machine. The estimation of the magnetizing inductance, L_m, at the operating state is crucial for T_r.

The delay in rotor flux, λ_{dr}, due to T_r, makes the q-component of the stator current, i_{qs}, most suitable as the prime variable in fast torque control. i_{ds} is used to maintain the magnetization at its reference. Generally one can say that i_{qs} is the active power reference current and i_{ds} is the reactive power reference current. During steady operation, the cross-product of $d-$ and $q-$ current components scales the resulting torque: $\tau_e \propto i_{ds}$ x i_{qs}. The maximum torque is limited to the current ratings of the machine as seen in equation 10.10:

$$\sqrt{i_{sd}^2 + i_{sd}^2} \leq \sqrt{2} \cdot I_n \tag{10.10}$$

10.2 Direct Vector control - DVC

Direct vector control relies on on-line estimation of the rotor flux position. The control is less sensitive to machine parameters, but it is, however, sensitive to the measurements used to determine the rotor flux. Hall-sensors can be used to perform such flux measurement. Another approach for the direct vector control is measuring the stator currents and stator voltages and transforming them into the static reference frame components. After calculating the flux in the static reference frame, an estimation of the rotor flux position, θ_e, can be made: The procedure shown in equations 10.11- 10.15 is usually used to obtain the rotor flux when the voltages and currents are known:

$$\lambda_{ds} = \int (v_{sd} - i_{ds} r_s) \tag{10.11}$$

$$\lambda_{qs} = \int \left(v_{qs} - i_{sq} r_s\right) \tag{10.12}$$

$$\lambda_s = \sqrt{\lambda_{ds}^2 + \lambda_{sq}^2} \tag{10.13}$$

$$\cos\theta_e = \frac{\lambda_{ds}}{\lambda_s} \tag{10.14}$$

$$\sin\theta_e = \frac{\lambda_{qs}}{\lambda_s} \tag{10.15}$$

where the unity vectors of flux position, $\cos\theta_e$ and $\sin\theta_e$, makes up the rotor flux position. It is used in the inverse Park-transformation to obtain i^*_{abc}

There are some challenges that need to be overcome when using DVC: If Hall sensors are used, they are fragile and sensitive to temperature. There could potentially become drift in the integration used to obtain the flux. The flux estimation is most challenging at lower speeds and position control. Another consideration is that several sensors naturally increases the costs. In the investigated system low cost is favored, and thus DVC is not further investigated here.

10.2.1 Direct Torque Control - DTC

Direct torque control (DTC) is another vector control technique used for induction machines. It is developed by ABB and is most similar to DVC (Direct vector control). The DTC is based on theory developed by Depenbrock [16], and uses two different control loops to control the switching of converters directly (without PMW or current hysteresis). Those two loops correspond to the magnitude of flux and torque. The independent control of torque and flux is similar to IVC. The DTC has been successfully applied to drives applications, and is among the industrial standards today. It has relatively large torque ripple, but the simple implementation and fast response are usually favored above other control techniques. However, DTC has not been fully proven for control of induction machines in generating mode yet [16]. Thus, the usage of DTC is still an topic in of further research, but it will not be explained in details here.

10.3 Indirect Vector Control - IVC

Indirect vector control (IVC) estimates the rotor flux while mitigating the need of measurements. The method is based on using the rotor position, θ_r, in a feed forward manner to determine the rotor flux position, θ_e.

In equation 10.4, the q-axis rotor flux is defined to be zero and will remain at zero. Thus, the rotor flux is aligned with the d-axis. The rotor flux can be assumed to be a "stable" value that does not change, thus the rough assumption, $\frac{d}{dt}\lambda_{rd} = 0$, yields. The rotor voltage equation 10.2 is repeated here as equation 10.16 and 10.18.

$$0 = v_{rq} = r_r i_{rq} + (\omega_e - \omega_r) \cdot \lambda_{rd} \tag{10.16}$$

and thus the slip frequency, ω_{sl}, is given by:

$$\omega_{sl} = \omega_e - \omega_r = -\frac{r_r i_{rq}}{\lambda_{rd}} \tag{10.17}$$

$$0 = v_{rq} = r_r i_{rq} \tag{10.18}$$

The q-component of the rotor current is zero: $i_{rq} = 0$. The steady flux (from 10.8) is given by:

$$\lambda_{rd} = L_m i_{sq} \tag{10.19}$$

Using equation 10.19 and 10.5 in 10.17 gives:

$$\omega_{sl} = \frac{i_{sq}}{i_{sd}} \cdot \frac{r_r}{L_m + L_{lr}} = \frac{i_{sq}}{i_{sd}} \cdot \frac{1}{T_r} \tag{10.20}$$

Equation 10.20 show that the slip speed, ω_s, is given by the ratio of the stator current components when the reference frame is properly oriented. If the references of the current components i^*_{ds} and i^*_{qs} are inserted into 10.20, the commanded slip speed, ω^*_{sl}, is obtained. By integrating ω^*_{sl} and adding the measured rotor position, θ_m, the flux position, θ_e, is found. This position is fed forward to the dq0-abc transformation in order to obtain the abc-reference currents.

Form 10.6 the reference torque τ^* is given by:

$$\tau^*_e = \frac{3}{2} p_p \cdot \frac{L_m}{L_r} \cdot \lambda^*_{rd} i^*_{sq} \tag{10.21}$$

where the reference rotor flux, λ^*_{dr}, is given by 10.19. It is seen that the steady state torque in principle is proportional to the product of the d-q current components.

10.4 Current Limitations

The current in an induction machine is limited by the rated current limitation (10.10). However, an induction machine operating at a higher speed gives a higher back emf. The dq-components of the stator voltage can be limited by:

$$V_s \geq \sqrt{v^2_{sd} + v^2_{sq}} \tag{10.22}$$

where $V_s = \sqrt{2} \cdot \frac{400}{\sqrt{3}}$ V = 326.59 V for the nominal voltages of #M1-#M6. Expressions for the dq-voltage components can be found by using equation 10.1 and obtain:

$$v_{sd} = -\omega_e \sigma L_s i_{sq} + r_s i_{sd} \tag{10.23}$$

$$v_{sq} = \omega_e \sigma L_s i_{sd} + r_s i_{sq} \tag{10.24}$$

Equations 10.23 and 10.24 are based on the following assumptions and definitions:

- The conditions are steady (i.e. currents and fluxes are not varying: $\frac{d}{dt}\lambda_s = \frac{d}{dt}\lambda_r = 0$)
- $L_s = L_m + L_{ls}$
- $L_r = L_m + L_{lr}$
- $\sigma = 1 - \frac{L^2_m}{L_s L_r}$
- $\lambda_{rq} = 0$, and thus: $i_{rq} = -i_{sq}\frac{L_m}{L_r}$
- $i_{rd} = 0$

Further, by neglecting the stator voltage drop (due to $r_s \cdot i_{sdq}$) in 10.23 and 10.24, a simplified diagram of the dq-current limitations for #IM1 is drawn in Figure 10.1. The blue circle curve[2] is the rated current limit from 10.10, while the dashed, cyan, red and green ellipse curves indicates the dq-current limitations from 10.22 for the respective electrical frequencies. Allowed operating states for the induction machine must lie within the current circle and the voltage ellipse. It is seen that in the nominal speed range (~ 50 Hz) and above, i_d is limited by the voltage for the 50 Hz case. Figure 10.1 shows that i_d is limited well below the nominal current, I_n, at 50 Hz. The stretching of the voltage

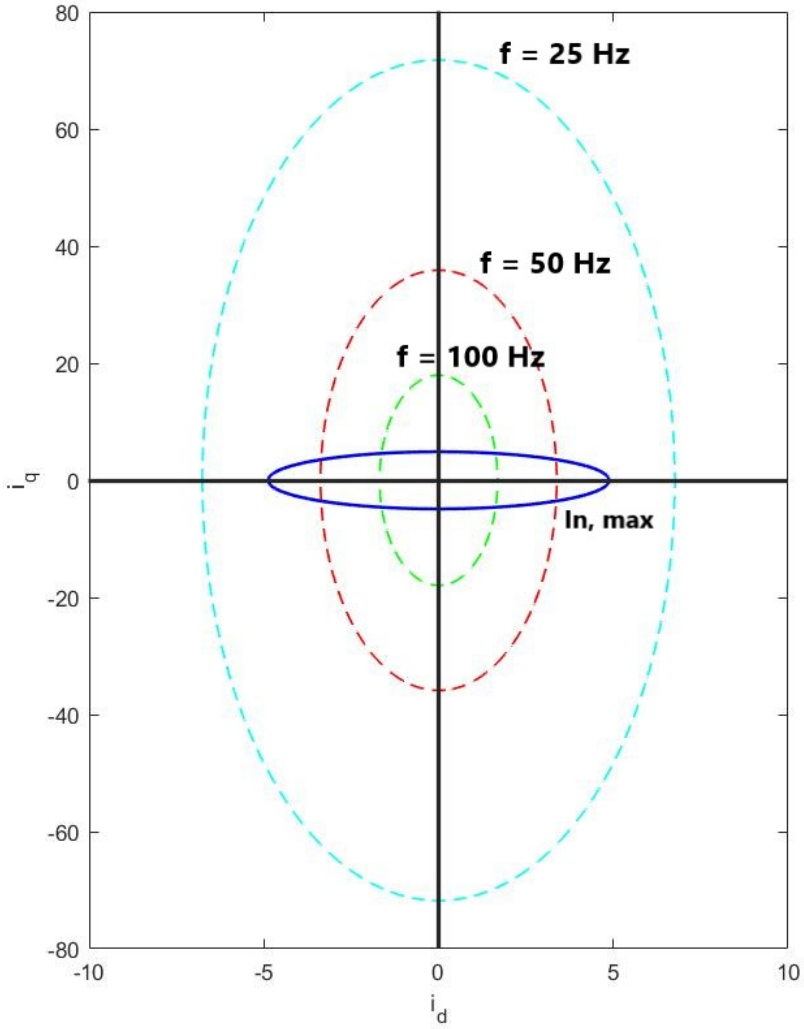

Figure 10.1: Current limitations in terms of voltage ellipses (dashed lines) for different frequencies and current circle (bold blue line) of the nominal stator currents for #IM1 (1.5 kW) sketched in the dq-domain.

ellipses in the $q-$direction is determined by σ (as defined in the list above). A low value of σ gives a large stretch and occurs when $L_m >> L_{ls}$ and $L_m >> L_{lr}$. If the stator voltage drops were included in Figure 10.1, the offset of the voltage ellipses would be displaced some degrees anti-clockwise. However, it would have no significant effect on the point of intersection with the current limit circle. Thus, Figure 10.1 gives a good indication of the induction generators field weakening region and how

[2]If the d- and q-axes are equally scaled the blue curve becomes a circle.

i_{ds} and i_{qs} should be properly limited.

10.5 Implementation of the IVC-Scheme

The fundamental objective of the IVC is to calculate the rotor flux position, θ_e, and the references of the dq-current components that are used to obtain the output reference stator currents, i^*_{abc}. Table 10.1 shows the IVC inputs (measurements) and outputs (fed to current hysteresis).

Table 10.1: Inputs and outputs used in IVC

Inputs (5) **from measurements**	**Outputs (3)** **to current hysteresis controller**
DC-link voltage, V_{dc} Mechanical shaft speed, ω_r Stator currents, i_{abc} (3)	Reference stator currents, I^*_{abc} (3)

A schematic structure of the IVC is shown in Figure 10.2. The angular rotor position, θ_r, is obtained by integrating the mechanical speed, ω_r, while taking the number of pole pairs into account. The *flux controller* controls the d-axis reference current, i^*_d which generates the flux. i^*_d is usually said to be a "stable" quantity and is maintained more or less constant. The *torque controller* receives the i^*_d and the DC-voltage V_{dc}. It produces the reference current for torque generation, i^*_q. These two reference currents and the rotor time constant, T_r, are used to calculate the commanded slip speed, ω_{sl}, and the slip angle, θ_{sl}, in the *slip speed* block. To obtain the rotor flux position, θ_e, the angular rotor position ,θ_m, is fed forward and added to the slip angle, θ_{sl}. The commanded dq^*-current components are fed into a dq0-abc transformation to obtain the three phase reference current that is fed into the current hysteresis. It is also possible to obtain three phase reference voltages with modulation index, m_a, and a frequency reference, f_{ref}, and use S-PWM to obtain the gate signals as done for V/f-control

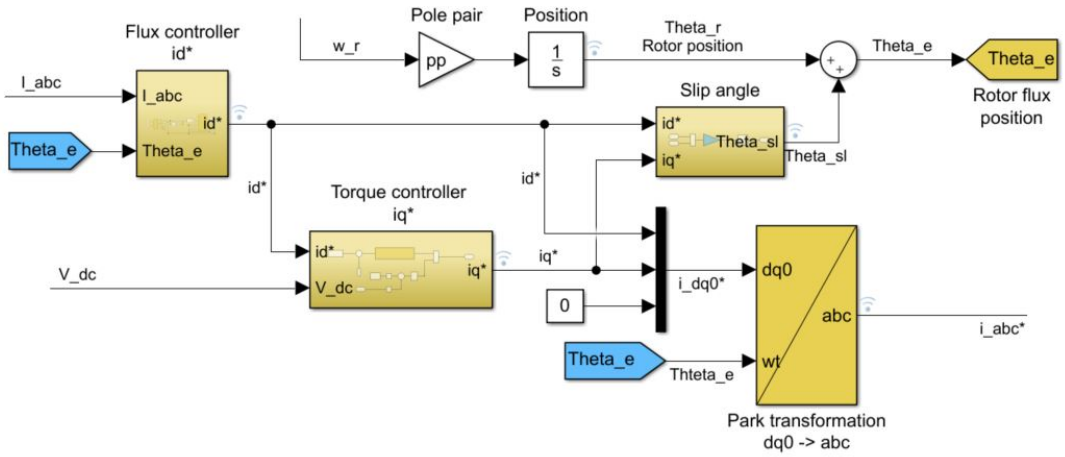

Figure 10.2: Overview of indirect vector control (IVC). The rotor flux position, θ_e, is estimated based on the slip speed and rotor speed. The reference $d-$ and $q-$current components are calculated to obtain the stator reference currents, which are fed into the current hysteresis.

10.5.1 Flux controller, i_d^*

The flux controller generates the reference d-axis current component, i_d^*, which is proportional to the rotor flux of the machine, λ_{rd}. For most cases, λ_{rd} is "stable" due to the delay from T_r and is thus held constant during transients. Thus, also i_d^* becomes stable. The value for i_d^* must satisfy the limitations for stator current as discussed in Subsection 10.4.

The simplest approach is to keep i_d^* constant during IVC. Then it must produce sufficient flux to keep the induction machine magnetized in the allowed operation range, and thus the constant value of i_d^* must be high enough to keep the machine magnetized when operating at no-load to full-load. The drawback is that the machine must operate at this full-load magnetizing current in the whole range between no-load and full-load. The stator currents will become unnecessarily high during no-load and low load, which make the low-load operation with constant i_d^* inefficient. Reducing i_d^* will reduce the three phase stator currents and thus the stator copper losses ($i_s^2 \cdot r_s$). In those cases, a proper programmed i_d^* will increase the efficiency of the induction machine. Fuzzy logic can be used for this purpose [16].

If the generator are speeded up such that field weakening is required, i_d^* needs to be reduced accordingly, such that it satisfies the constraints in Figure 10.1.

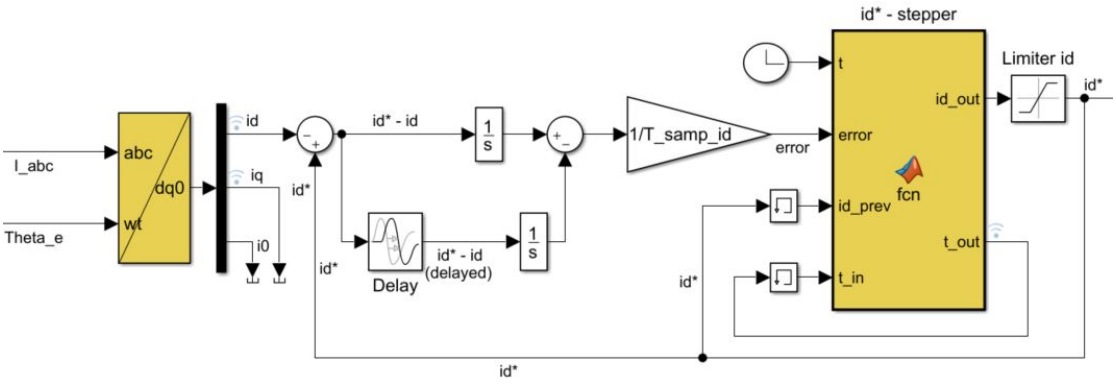

Figure 10.3: Inner structure of the flux controller: An approach to achieve proper control of the magnetizing current, i_d^*, by comparing the actual i_d and i_d^* to evaluate the need for adjusting i_d^*.

An attempt to make a control script that scales i_d^* is showed in Figure 10.3. It transforms the measured stator currents into the synchronous (rotor flux) dq0-domain to obtain a "measured" i_d that is subtracted from the calculated reference i_d^* to obtain an error. The error is fed into a moving average filter, whose is a common filter in digital signal processing (DSP). It is simple and optimal for the task of reducing random noise while retaining a sharp step response [26]. In general, it operates by averaging a number of points from the input signal to produce the points in the output signal. In Figure 10.3 this is achieved by delaying the error by $\frac{T_{samp}}{2}$. The i_d^*-stepper updates i_d^* every T_{samp}, to adapt if the operating conditions changes. Memory blocks are used to memorize current and step time between each update of i_d^*. A high value of i_d^* is favorable to effectively handle step changes.

Due to some difficulties with the control of i_d^* in above described system, the assumption: $i_d^* = \frac{I_n}{2} = const$ are made here. The assumption is used in the following simulations instead of the controlled i_d^* from the flux controller. This is done for IVC in [16]. However the above attempt of making a flux controller is a good starting point for further work.

10.5.2 Torque controller, i_q^*

Figure 10.4 shows the inner structure of the torque controller. It contains a PI-controller that scales the DC-voltage error to obtain a normalized quadrature current, i_q^* $(norm)$, such that the DC-reference can be maintained at its reference. The inner structure of the PI-controller is shown in Figure 10.5. The integrator and the output of the controller are both limited to ± unity. The normalized q-axis current from the PI-controller is multiplied by the maximum quadrature axis current found from equation 10.10 and implemented in Figure 10.4. The inner structure of the Pi-controller are shown in Figure 10.5.

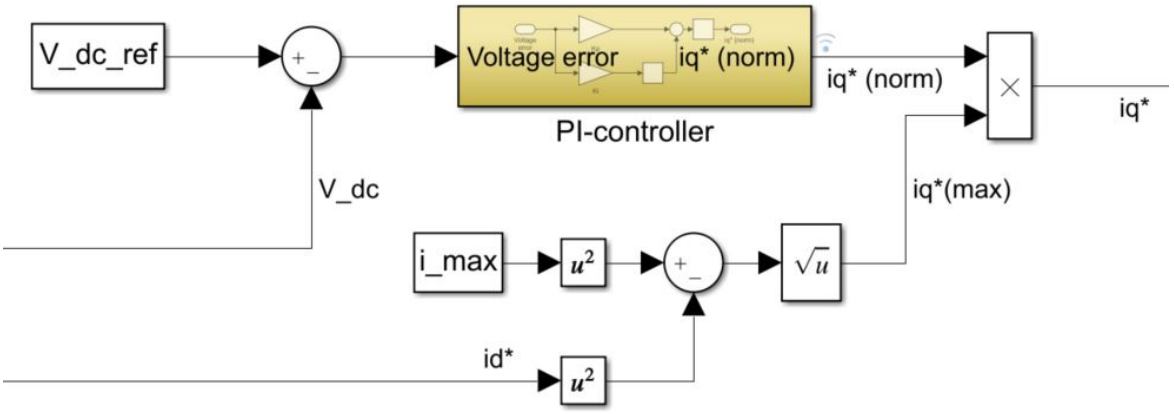

Figure 10.4: Inner structure of torque controller. A normalized i_{qnorm}^* is adjusted based on the DC-voltage error. i_d^* determines the maximum amount of i_q^* that does not cause excessive stator currents.

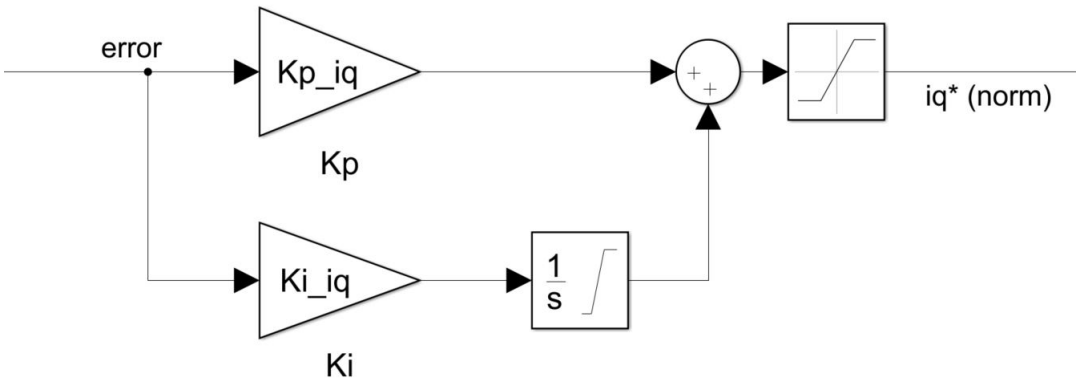

Figure 10.5: Inner structure of PI-controller used in the torque controller

10.5.3 Slip angle

The slip angle block calculates the slip angle, θ_{sl}. It uses the ratio of the magnitude of q-axis to d-axis current components and the rotor time constant, T_r, to find the slip speed, ω_{sl}, by using equation 10.20. Finally, the slip angle, θ_{sl}, is found by integrating the slip speed, ω_{sl}. The rotor time constant is given by the induction machine parameters: $T_r = \frac{L_{lr}+L_m}{r_r}$, and thus θ_{sl} becomes largely dependent on the machine parameters. The parameters, especially L_m, vary with the operating state (current voltage, frequency, temperature etc.) and is difficult to estimate exactly.

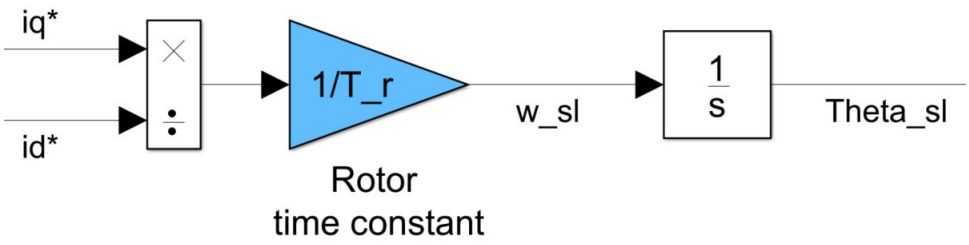

Figure 10.6: Structure for calculation of instantaneous slip position, θ_s, based on i_d^* and i_q^* and the rotor time constant, T_r.

10.5.4 Parameter list

Table 10.2: Fixed parameters used in indirect vector control.

Name	Value for #IM1	Appears in	Description
p_p	2	IVC	Pole pairs
$f_{sw,IVC}$	25 kHz	Current hysteresis	Switching frequency
$V_{dc,ref}$	565 V	Torque controller	DC-link reference voltage
i_{max}	$\sqrt{2}I_n$	Torque controller	Rated generator peak current
τ_r	0.111 s	Slip angle	Rotor time constant
$i_{q,u}$	1	Torque PI-controller	Limit for integrator and output
$i_{q,l}$	-1	Torque PI-controller	Limit for integrator and output

11 Load Voltage Controller

Chapter 11 deals with the load controllers structure and how it achieves the resulting load side performance. The purpose of the load voltage controller is to keep the load side voltage at its reference voltage and frequency. The load controller generates a modulation index and a frequency reference. The generation of gate signal is done by S-PWM with 3^{rd} harmonic injection.

11.1 Implementation of Load Voltage Controller

An overview of the inputs and outputs of the load voltage controller can be seen in Table 11.1

Table 11.1: Inputs and outputs of the load voltage controller

Inputs (3) **from measurements**	**Outputs (2)** **to S-PWM with THI**
Stator voltages v_{abc} (3)	Modulation index, m_a Load frequency reference, f_e

The schematic overview of the load voltage controller is seen in Figure 11.1. It receives the measured three phase load voltages, measured at the load side of the passive filter. Based on those voltages, it uses the static park transformation and some simple calculations to obtain the load voltage peak value at that instant. The calculated peak value is compared to the reference $\hat{V}_{load,ref} = \sqrt{2} \cdot V_{nom}$ = 325 V, and fed through a limited PI-controller to obtain the load side modulation index, $m_{a,load}$. The inner structure of the limited PI-controller is shown in Figure 11.2. It has a similar structure to the PI-controllers (e.g. in the torque controller in IVC). The frequency reference, f_{ref}, is constant and set to 50 Hz as desired. In principle, f_{ref} could have been set to an arbitrary frequency reference because of the decoupling from generator frequency by the DC-link.

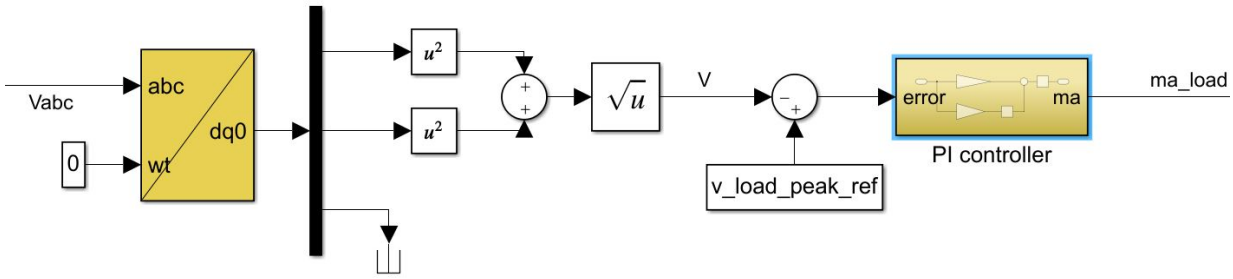

Figure 11.1: Schematic overview of the load voltage controller. Calculates the modulation index, m_a, based on the instantaneous load voltages and the load peak reference $\hat{V}_{load,ref}$.

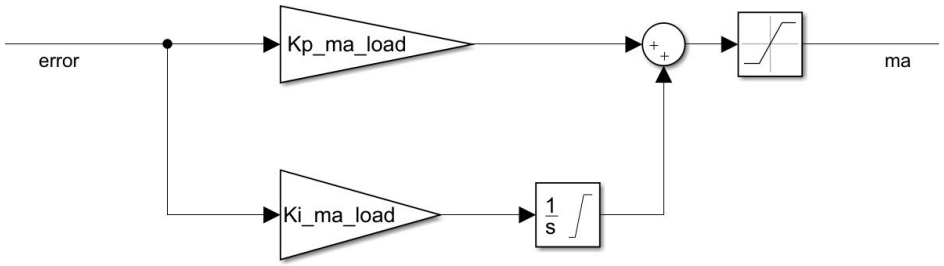

Figure 11.2: Inner structure of load PI-controller used in load controller.

11.2 Parameter list

The fixed parameters used in the load voltage controller are given in Table 11.2.

Table 11.2: Fixed parameters in load voltage controller

Name	**Value used in S-PWM**	**Appears in**	**Description**
$V_{dc,ref}$	565 V	Voltage controller	DC-link reference voltage
$f_{load,ref}$	50 Hz	S-PWM	Reference load frequency
$f_{sw,load}$	5 kHz	S-PWM	Switching frequency
$\hat{V}_{load,ref}$	$\sqrt{2}V_{nom}$ = 325 V	Voltage controller	Reference peak load voltage
$ma_{u,load}$	1	Voltage PI-controller	Upper integrator and output limit
$ma_{l,load}$	0	Voltage PI-controller	Lower integrator and output limit

12 Tuning of Parameter

12.1 Turbine and Governor Parameters

The turbine and governor parameters are assumed to be constant. These are dependent on turbine characteristics and the physical and geographical circumstances at site in addition to the maximal load demand that is supplied by the system. The turbine rated power of the picked turbine is 2.2 kW somewhat above the maximum load demand, due to the total losses in turbine, generator, converters and filter. The design procedure of the turbine and governor in addition to the tuning of droop parameters are described and discussed in chapter 2.3.

12.2 Ratings of Electrical Components

12.2.1 Rating of Generator

The rated power of the generator must, in the same manner as the turbine, be able to supply the maximum load demand, $P_{L,max}$, in addition to all the electrical losses $P_{e,loss}$. Thus, the power ratings of the generator, $P_{n,gen}$, must satisfy:

$$P_{n,gen} \frac{P_{L,max}}{\eta_{tot}} \tag{12.1}$$

where η_{tot} is the total electric efficiency.

12.2.2 DC-Link Voltage Reference

The DC-link voltage reference, V_{dc}, is mainly determined by the RMS/DC method described in chapter 5.3. For the V/f-controlled S-PWM operated generator it is assumed that the operating state is close to the nominal voltage and speed of the generator, and thus:

$$V_{dc,gen} = \frac{V_{n,gen}}{\bar{v}_m} \tag{12.2}$$

It is assumed that the value obtained for V/f controlled S-PWM is a reasonable set point for the current hysteresis gate signal controller in IVC. The load side controller also uses the S-PWM and thus the RMS/DC-method can be used. However, there is an additional voltage drop due to the passive filter at the load side of VSC. Thus, the DC-voltage needs to be increased by a factor k in the RMS/DC-method:

$$V_{dc,load} = \frac{V_{n,gen}}{\bar{v}_m} \cdot (1 + k) \tag{12.3}$$

For a given value of k, the maximum voltage drop across the filter inductors L_1 and L_2 must not exceed:

$$k \cdot V_{n,load} > 2\pi(L_1 + L_2) \cdot I_{n,load} \tag{12.4}$$

When comparing the DC-link reference requirement for both generator side and load side, the maximum of those is determining the DC-link voltage reference. In some cases, an additional margin of 10% is added to this value. The set-point criterion thus becomes:

$$V_{dc,ref} = \max\left[V_{dc,gen}, V_{dc,load}\right] \cdot 1.10 \tag{12.5}$$

By using injection of 3^{rd}-harmonic in the reference signal wave, the utilization of the DC-voltage will be increased somewhat by using a slightly greater $\bar{v}_m$. This procedure has determined the DC-link voltage reference, $V_{dc,ref}$ to be 565 V.

12.2.3 DC-link Capacitor and Battery Voltage

The DC-link capacitor stores an amount of energy between the generator side and load side. As discussed in chapter 4.2, the DC-link capacitor works as a buffer during sudden variations in generated power and load demand. By assuming that the DC-link capacitor should be able to store 10% of maximum load demand and by using equation 4.6,the following is found:

$$C_{dc} = \frac{0.1 \cdot P_{L,max}}{\frac{1}{2}V_{dc}^2} \tag{12.6}$$

The capacitor must also be rated for the DC-link voltage. It is the largest device in the control system, but it is assumed that neither size (volume) nor price are crucial factors for the DC-link capacitor.

The battery is connected to the DC-link to obtain an initial voltage in the DC-link. This initial voltage is necessary in order to magnetize the induction generator and thus build up the DC-link voltage. Batteries with voltages V_{batt} = 10 V - 60 V will be sufficient for this purpose, and a value of V_{batt} = 40 V is used in the model. A common available type of batteries that can be used for this purpose is conventional car batteries. Those can deliver a high current for short periods. The battery current is used to charge up the DC-link voltage (across the capacitor) to V_{batt}, before the excitation process starts. When the system is running, the battery can be removed. A lower battery voltage will give a longer charge up time and a higher battery voltage will give a shorter charge up time. In order to obtain simplicity in the Simulink model, the battery is replaced with an initial capacitor voltage at V_{batt}.

12.2.4 Switching Frequency

The switching frequency is mainly determined by the desired output wave forms, and thus the switching frequency should be as high as possible in the ideal case. The frequency modulation, m_f, for the S-PWM based methods is assumed to be $m_f > 100$. In the case of current hysteresis (IVC), the frequency modulation is increased to be $m_f > 500$. There is a trade-of between shape of the output wave forms, switching losses and size of filter components. When determining the frequency modulation the switching frequency can be found by:

$$f_{sw} = m_f \cdot f_{ref} \tag{12.7}$$

12.2.5 Passive Filter

The components in the passive LCL-filter is determined though a design procedure in accordance with [24]. The details in the procedure are given in chapter 6.

12.2.6 Other Considerations

In a real system, the transistors in VSC, gate drives, lines and sensors used for measurements etc. will have physical constraints and will not behave ideal, as assumed in this study. These constraints are in terms of voltage, current, temperature and time dependency and become important when choosing components for a real system. Such considerations can be crucial for the real system's performance, reliability and expected lifetime.

12.3 Control System Parameter

The control system contains some saturation-blocks which provide a limitation of the controlled outputs. It also contains several *if/else*-statements. Thus, the system becomes a non-linear control

system. The non-linear characteristics make it comprehensive to obtain an accurate transfer function that describes the behavior of the system. For simpler and linear control systems, the transfer function is a natural starting point when tuning the control system parameters. Modulus optimum and symmetrical optimum are among the common tuning techniques.

The system contains several PI-controllers with proportional gain, K_p, and integral gain, K_i. The integrator and the controller output are limited to an upper and a lower limit, respectively. In most cases these limits are set to ± unity for the upper and lower limit. For simplicity, a PI-speed controller is considered to be suitable. The PI-controller has a reference speed at y_{ref}. The maximum acceleration equals an upper speed limit, y_u = 1, and maximum braking equals a lower speed limit, y_l = -1. A certain error, y_{error} (e.g speed deviation), is used to determine the value of y_{error}, that the proportional gain will scale the output, y, to y_u (unity). From this size of errors and upward the system will accelerate (or decelerate) at maximum. The basis for the proportional gain, K_p, used in the control system is determined by the relation:

$$K_p = \frac{y_u}{y_{error}} \tag{12.8}$$

where the error is a given fraction of the reference speed:

$$y_{error} = \frac{1}{k} \cdot y_{ref} \tag{12.9}$$

The integral gain, K_i, builds up over some time and helps K_p to reach its reference without any stationary deviation. If saturation of K_i is achieved within a time t for a speed deviation v_{error}, the integral gain is given by:

$$K_i = \frac{y_u}{t \cdot y_{error}} \tag{12.10}$$

The saturation times for integral gains are set to saturate for k periods of the nominal frequency of the system (i.e. $t = \frac{k}{f_{nom}}$). The tuning of controller parameters for V/f-control, IVC and load voltage controller are given in Table 12.1-12.3. A more detailed discussion of the functionality of P-, PI- and PID-controllers are given Appendix D.

Table 12.1: Basis for tuning of parameters in V/f-controller

Name	Parameter name in MATLAB	Basis for tuning	Appears in	Description
$\omega_{sl,error}$	w_sl_error	$0.1 \cdot V_{dc}$	Slip speed PI-controller	Integral error
$\omega_{sl,u}$	w_sl_u	$2 \cdot \omega_{sl,nom}$	Slip speed PI-controller	Limit (integrator, output)
$\omega_{sl,l}$	w_sl_l	$-2 \cdot \omega_{sl,nom}$	Slip speed PI-controller	Limit (integrator, output)
$K_{p,\omega_{ls}}$	Kp_w_sl	$\frac{\omega_{sl,u}}{\omega_{sl,error}}$	Slip speed PI-controller	Proportional gain
$K_{i,\omega_{sl}}$	Ki_w_sl	$-\frac{\omega_{sl,u}}{2 \cdot \omega_{sl,error}/f}$	Slip speed PI-controller	Integral gain
$K_{i,i}$	Ki_i	$\frac{i_{lower}}{10/f}$	Current limiter	Integral gain
$K_{i,ma,u}$	Ki_ma_u	$\frac{V_{dc} \cdot \bar{v}_m}{V_{nom}}$	Voltage controller	Integrator limit
$K_{i,ma,pos}$	Ki_ma_pos	$\frac{K_{i,ma,u}}{(100/f) \cdot \omega_{sl,error}}$	Voltage controller	Integral gain
$K_{i,ma,neg}$	Ki_ma_neg	$10 \cdot K_{i,ma,pos}$	Voltage controller	Integral gain

Table 12.2: Basis for tuning of parameters in IVC

Name	Parameter name in MATLAB	Basis for tuning	Appears in	Description
h_{lim}	hyst_lim	$10 \cdot i_{max}$	Current hysteresis	Band gap
$i_{q,error}$	iq_error	$0.1 \cdot V_{dc}$	Torque PI-controller	Integral error
$K_{p,iq}$	Kp_iq	$\frac{i_{max}}{i_{q,error}}$	Torque PI-controller	Proportional gain
$K_{i,iq}$	Ki_iq	$\frac{i_{max}}{i_{q,error} \cdot (2/f_{nom})}$	Torque PI-controller	Integral gain
$i_{d,u}$	id_u	$\frac{i_{max}}{\sqrt{2}}$	Flux Controller	Upper output limit
$i_{d,l}$,	id_l	$\frac{i_{max}}{10}$	Flux Controller	Lower output limit
$i_{d,inc}$	id_inc	$i_{max} \cdot 0.01$	Flux Controller	Step change
$i_{d,error}$	id_error	$i_{max} \cdot 0.005$	Flux Controller	Error
$T_{id,samp}$	T_samp_id	$\frac{1}{10 \cdot f_{nom}}$	Flux Controller	Sample time MV

Table 12.3: Basis for tuning of parameters in load voltage controller

Name	Parameter name in MATLAB	Basis for tuning	Appears in	Description
$ma_{L,error}$	ma_error_load	$0.1 \cdot \hat{V}_{L,ref}$	Voltage controller	Integral error
$K_{p,ma,L}$	Kp_ma_load	$\frac{ma_{u,L}}{ma_{L,error}}$	Voltage controller	Proportional gain
$K_{i,ma,L}$	Ki_ma_load	$\frac{ma_{u,L}}{ma_{L,error} \cdot (2/f_{L,ref})}$	Voltage controller	Integral gain

13 Results from Simulation Study

This chapter presents the results achieved when studying the V/f-control and the IVC-control schemes for the induction generators #IM1-#IM5 in the MATLAB Simulink model. Parameter data and magnetizing characteristics for the induction machines #IM1-#IM5 are presented in Appendix A. An overview of the Simulink model is seen in Figure F.1, which contains the whole system with turbine, generator, back-to-back converter, passive filter and the isolated load. Figure F.2 shows the four separated control systems (i.e. hydro governor, V/f-controller, IVC and load voltage controller). The structure of the physical system as well as the controller is discussed in the previous sections. Table 13.1 shows the values for the parameters that are kept fixed in the simulation tests:

Table 13.1: Parameter values kept fixed in simulation tests

$\mathbf{V_{gen,nom}}$	$\mathbf{P_{load,nom}}$	$\mathbf{V_{batt}}$	$\mathbf{V_{dc,ref}}$	$\mathbf{C_{dc}}$	$\mathbf{n_{nom}}$
400 V	1.5 kW	40 V	565 V	9.398 mF	1500 rpm

The purposes of the tests performed can be summarized as follows:

- **Test 1** investigates the properties of V/f-control and IVC for different power ratings of the generator while rotating at nominal speed.
- **Test 2** investigates the dependency of the rotor time constant, T_r, for IVC while rotating at nominal speed. T_r is determined by the machine parameters.
- **Test 3** investigates how the hydraulic turbine and governor influence the system properties. The load is increased by using a step-by-step load profile that is applied to the system load.
- **Test 4** focuses on the load controller and the passive LCL-filter performance and load voltage quality.
- **Test 5** investigates the system as a whole and the interactions between the separated control systems.

In all tests, the V/f-controller and load controller uses 3^{rd}-harmonic injection to increase the utilization of the DC-link voltage. Thus, v_m= 0.4606 and μ_{ma} = 4.714 as discussed in chapter 5.2.

Due to the magnetizing characteristic of the induction machine, the magnetizing inductance, L_m, is changing with the operation conditions, and in addition it is used to determine the rotor time constant T_r used in IVC. The value of L_m picked to determine T_r is sampled at a stator current at 0.3 pu (I_n = 1.044 A in Table A.6 for #IM1), which gives a rotor time constant of 0.11 s. The rotor time constant becomes more or less equal for all machines, since the per unit model is the same. A rotor time constant T_r = 0.11 s is in the upper operation range where X_m and L_m are constant. For higher magnetizing currents, the magnetizing characteristic leads to a decrease in X_m and L_m for higher currents. For an actual machine, the L_m might be lower than this "estimate" and thus also T_r, which influences the generator control. This behavior is investigated in Test 2.

For simplicity, the d-axis reference current, i_d^*, from the flux controller in IVC is kept constant during most simulations. i_d^* must produce sufficient flux to keep the generator magnetized during operation. However, if it is unnecessarily high, it will lead to high stator currents and decrease the efficiency of the generator, especially for low loading. Since the electromagnetic torque is proportional to the product of i_d and i_q, it is of minor importance at steady high generator loading. Fuzzy logic

can be used in the flux controller to find the optimal value of i_d^*.

The sampling time is set to T_s = 0.02 ms at all simulations to secure sufficient sampling during the high switching frequency (25 kHz) of the current hysteresis controller. This is in accordance with the Nyquist-Shannon sampling theorem [15].

13.1 Test 1: DC-link Charge-Up and Step to Full Load

Test 1 considers the excitation process of induction generators and the associated charge up of DC-voltage for the induction generators #IM1 -#IM5 controlled by V/f-control and by IVC. In addition, the properties of the controlled machine, while handling a step change from no-load to full load (1.5 kW), is investigated for both V/f-control and IVC. The mechanical speed is kept constant during this simulation at 1500 rpm, even though this is a rough assumption that is not physically possible by using the simple 2.2 kW turgo turbine model and the hydro governor. However, this test is done to investigate the performance of the induction generator control system when the speed is constant. Thus, the mechanical speed is selected as input to the mechanical input of the asynchronous machine block in the Simulink model. A constant speed of $\frac{2\pi \cdot 1500}{60}$ = 157 rad/s is used in Test 1. The initial slip of the generator is 0. An initial voltage across the DC-link capacitor represents the battery voltage which is connected to the DC-link at start up. If the values of the parameters and components in Table 13.1 are changed, it will influence the simulation results. Some definitions/measurement used in Test 1 need to be stated:

Charging time: Time from start ($V_{dc} = V_{batt}$ = 40 V) until the controlled DC-link voltage reaches its reference, $V_{dc} = V_{dc,ref}$ the first time.
Overshoot: Largest deviation from reference value (transient) before settling at the reference.
Drop: Largest deviation from reference voltage when step changes in the loading are applied.
Settle time: Time from a step change occurs until the controlled variable settles within ± 1 % of its rated value.

To investigate these properties, two simulations are run for each induction machine (#IM1,-#IM4), one controlled by the V/f-scheme and the other one by the IVC-scheme. The tables 13.2 and 13.3 show measured charging time and overshoot data for the above definitions of the DC-voltage. The time elapse of the DC-voltage, stator currents, modulation index (m_a), reference frequency, electromagnetic torque and the generated electrical power when #IM1-#IM4 are V/f-controlled are showed in Figure 13.1 - 13.4. Table 13.2 shows that a tendency of larger overshoot in DC-link voltage and shorter charging time are seen for higher ratings of generator (#IM1- #IM3). Initially, for #IM4 the overshoot in DC-voltage is no longer damped and the DC-link voltage becomes a standing oscillation. This have been caused by insufficient tuning of V/f-controller parameter (Table 12.1) with respect to the power and current ratings of generator. For these variations it is expected that the larger machines will have a quicker response since the per unit power needed to compensate for the changes is lower. By reducing the proportional gain in the slip speed controller and the integral gain accordingly, the V/f-control of #IM4 becomes sufficient damped and achieves stability. As expected, the charging time increases when the gain is reduced. Some oscillations are seen in Figure 13.4 and further parameter tuning will be needed for #IM4 and higher power ratings of machines. This has not been given any further attention in this work. During the charge-up and magnetization process, the frequency and modulation indexes are limited to constant values before they oscillates to their stationary no-load values. The electromagnetic torque (and thus power) must be large during charge up and excitation, and settle slightly below 0 to compensate for no-load stator losses.

Table 13.3 shows that the IVC (with constant $i_d^* = \frac{I_n}{2}$) produces a peak in the DC-link voltage at

600 V (+6.02% from the reference) independently of the generator power rating. This is since the rated current scales the magnitudes of i_d^* and i_q^*. i_d^* is also determined in the control. The overshoot is significantly lower than what obtained in V/f-control. The charging time and settling time are a bit longer compared to the stable V/f controlled case at same power rating. Lower charging time and settling time is achieved for higher power ratings as for V/f-control. #IM5 is operating at a relatively low loading of 1.5 kW. Thus, the i_d^*-current could preferably be reduced to increase the machine efficiency. It is seen that the actual i_d-current component initially takes a negative value during the excitation-process (charge up) before it stabilizes at its given reference. The q-current component also becomes negative to produce the needed torque to magnetize the generator and charge up the DC-link. In the no-load case, the q-current component is slightly below zero, since the electromagnetic torque must compensate for the no-load stator losses. It is seen a ripple in i_d and i_q. The ripple occurs also in the electromagnetic torque and power, since these quantities are proportional to i_d and i_q (equation 10.21). The torque ripple is larger for IVC than for V/f-control.

Table 13.2: Overshoot, charge up time and settling time for DC-voltage for #IM1- #IM4 V/f-control. Running at constant speed during magnetization.

Machine	Overshoot	Peak DC-voltage	Charging time	Settle time
#IM1	13.5 %	641 V	0.272 s	0.343 s
#IM2	17.3 %	663 V	0.216 s	0.358 s
#IM3	21.6 %	687 V	0.195 s	0.375 s
#IM4	45.3 %	821 V	0.282 s	0.624 s

Table 13.3: Overshoot, charge up time and settling time for DC-voltage for machines #IM1- #IM5 - IVC. Running at constant speed during magnetization.

Machine	Overshoot	Peak DC-voltage	Charging time	Settle time
#IM1	6.02 %	599 V	0.374 s	0.475 s
#IM2	6.19 %	600 V	0.307 s	0.405 s
#IM3	6.19 %	600 V	0.274 s	0.369 s
#IM4	6.19 %	600 V	0.228 s	0.334 s
#IM5	6.19 %	600 V	0.197 s	0.308 s

Table 13.4 and 13.5 show the behavior of the DC-link voltage when a load step of 1.5 kW is switched in after the voltage is stabilized at its reference. The Figures 13.1 - 13.8 show how this control is performed for the simulated cases: #IM1-#IM4 with V/f-control and with IVC[3]. Table A.5 shows how large the 1.5 kW load step is in per unit of the generator power rating. This is significant for the generator's ability to handle a load step at a given size. Except for #IM1, the generators are able to handle this load step. #IM1 becomes overloaded (due to the additional stator losses) and is not able to maintain the DC-link voltage at its reference anymore. For IVC, the DC-link voltage drops to 460 V for #IM1 (Figure 13.5). The V/f-scheme reaches the DC-link reference again before the DC-link gradually starts to decrease (Figure 13.1). In the cases of the other machines, #IM2-#IM4, it is seen that the DC-link voltage drops (in %) and the settle time are lower than the

[3]Note different times for the load step between plots.

corresponding overshoots and settle times during charge up. For the large machines, #IM4 and #IM5 (in IVC) the voltage drop is only ∼1% and the settle time is low. As expected #IM5 handles the 1.5 kW load step in the best way in terms of DC-link voltage drop. If the constant i_d^* is proper reduced the efficiency, η of larger machines while loaded at 1.5 kW could be increased (η is given in Table 13.5).

A higher (more negative) electromagnetic torque is generated to maintain the DC-voltage at reference while the system is loaded. The V/f-controller needs to operate at a higher (more negative) slip to produce the required torque. It is seen from Figures 13.1-13.4 that the reference frequency is controlled to its new reference at a lower frequency to increase the slip and thus the torque. It is seen that the frequency reference and the torque are proportional and follow the same shape. The modulation index is also reduced accordingly to keep the V/f-ratio constant. For IVC, the i_q-current drops to produce the needed electromagnetic torque when the load step is applied.

Table 13.4: Voltage drop and settling time (DC-voltage) and full-load efficiency for #IM1- #IM4 V/f-control. While running at constant speed, a load step of 1.5 kW is applied.

Machine	**Drop**	**Drop DC-Voltage**	**Settle time**	**Efficiency, η**
#IM1	-6.73 %	527 V	0.272 s [∞]	82.1 %
#IM2	-5.31 %	535 V	0.095 s	83.3 %
#IM3	- 4.42 %	555 V	0.103 s	85.7 %
#IM4	-1.06 %	559 V	0.009 s	79.0 %

Table 13.5: Voltage drop and settling time (DC-voltage) and full-load efficiency for generators #IM1- #IM5 with IVC. While running at constant speed, a load step of 1.5 kW is applied.

Machine	**Drop**	**Drop DC-voltage**	**Settle time**	**Efficiency, η**
#IM1	-12.56 %	494 V	∞	76.7 %
#IM2	-5.13 %	536 V	0.099 s	81.1 %
#IM3	-3.89 %	542 V	0.085 s	84.4 %
#IM4	-2.65 %	550 V	0.063 s	88.2 %
#IM5	-1.41 %	557 V	0.023 s	81.9 %

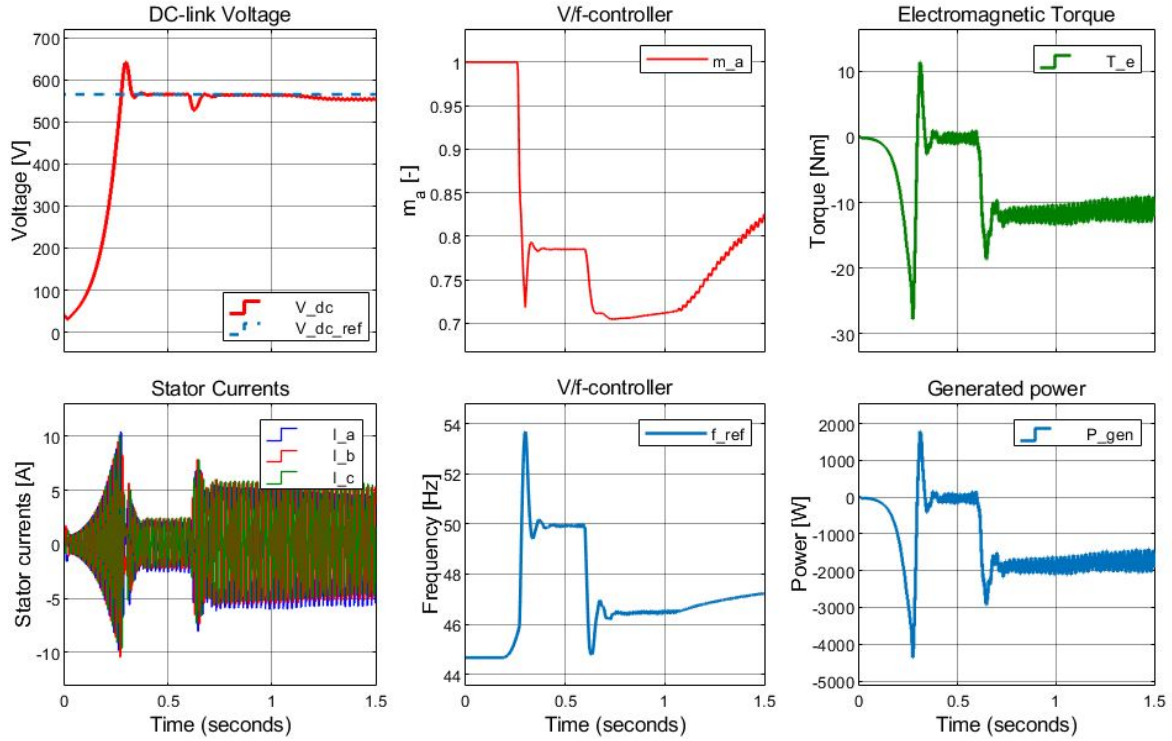

Figure 13.1: #IM1 (1.5 kW) controlled by V/f-control. Magnetization process and a load step of 1.5 kW at 0.6 s is applied. The machine becomes overloaded and the DC-voltage reduces.

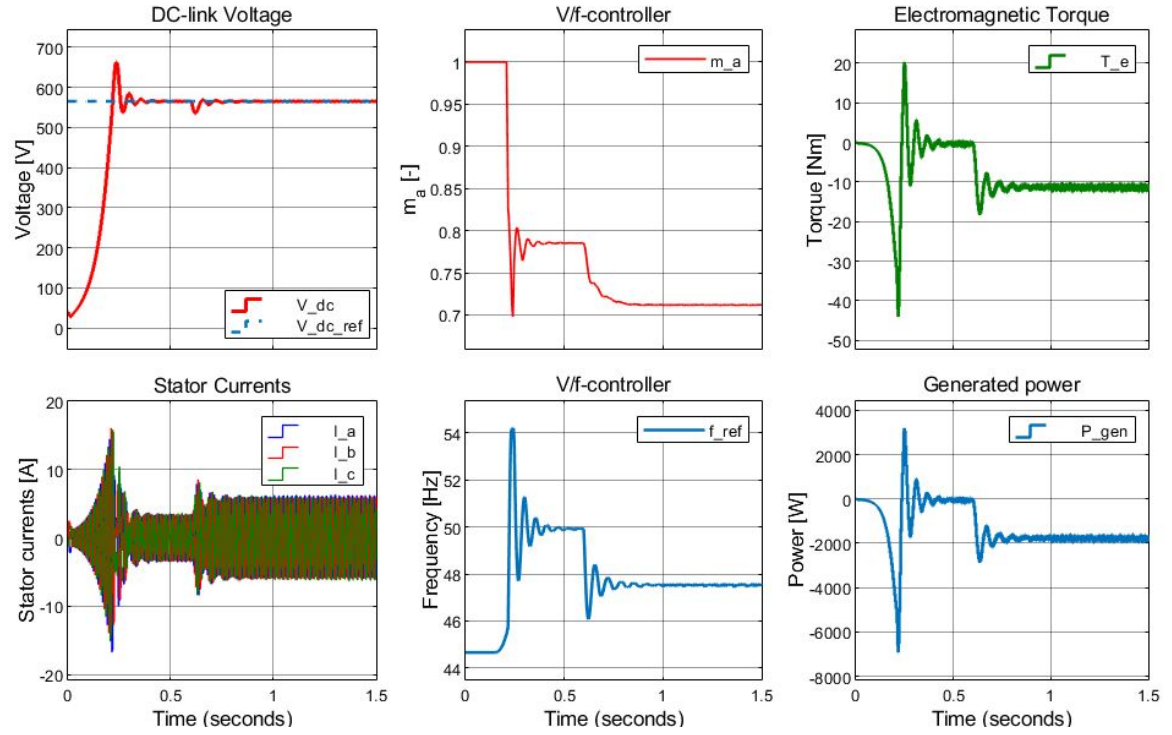

Figure 13.2: #IM2 (2.2 kW) controlled by V/f-control. Magnetization process and a load step of 1.5 kW at 0.6 s is applied. The machine can maintain the DC-link voltage.

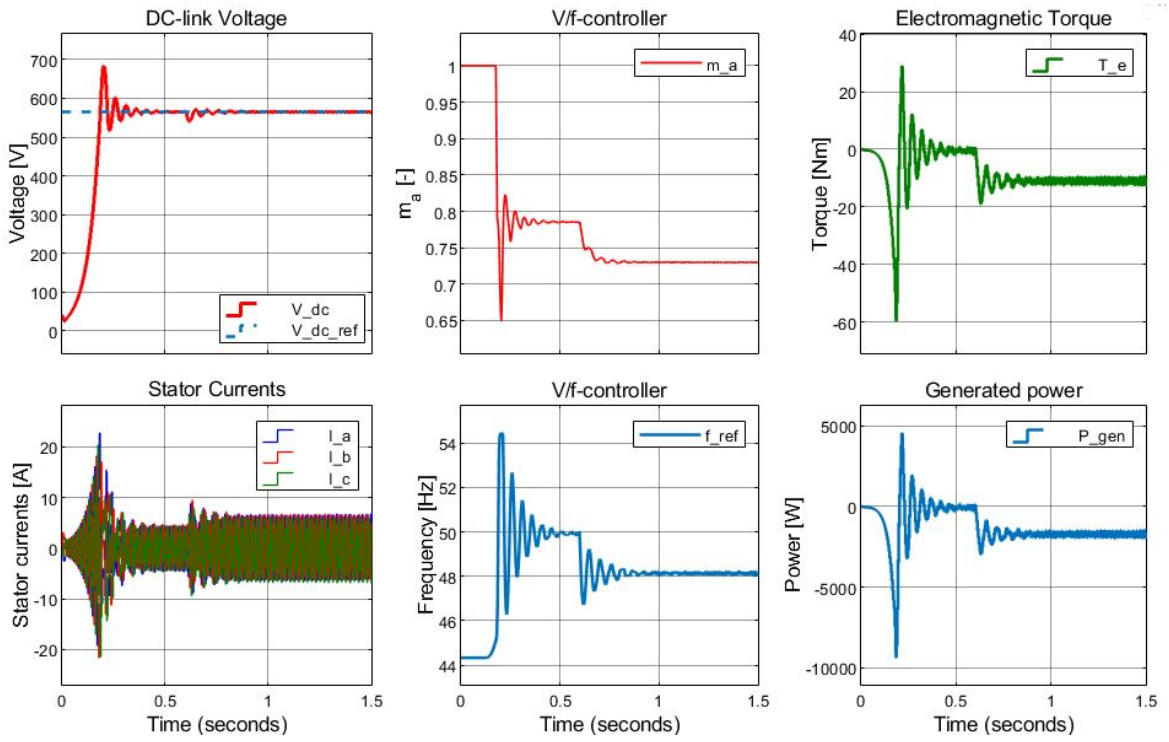

Figure 13.3: #IM3 (3.0 kW) controlled by V/f-control.Magnetization process and a load step of 1.5 kW at 0.6 s is applied. The machine can maintain the DC-link voltage.

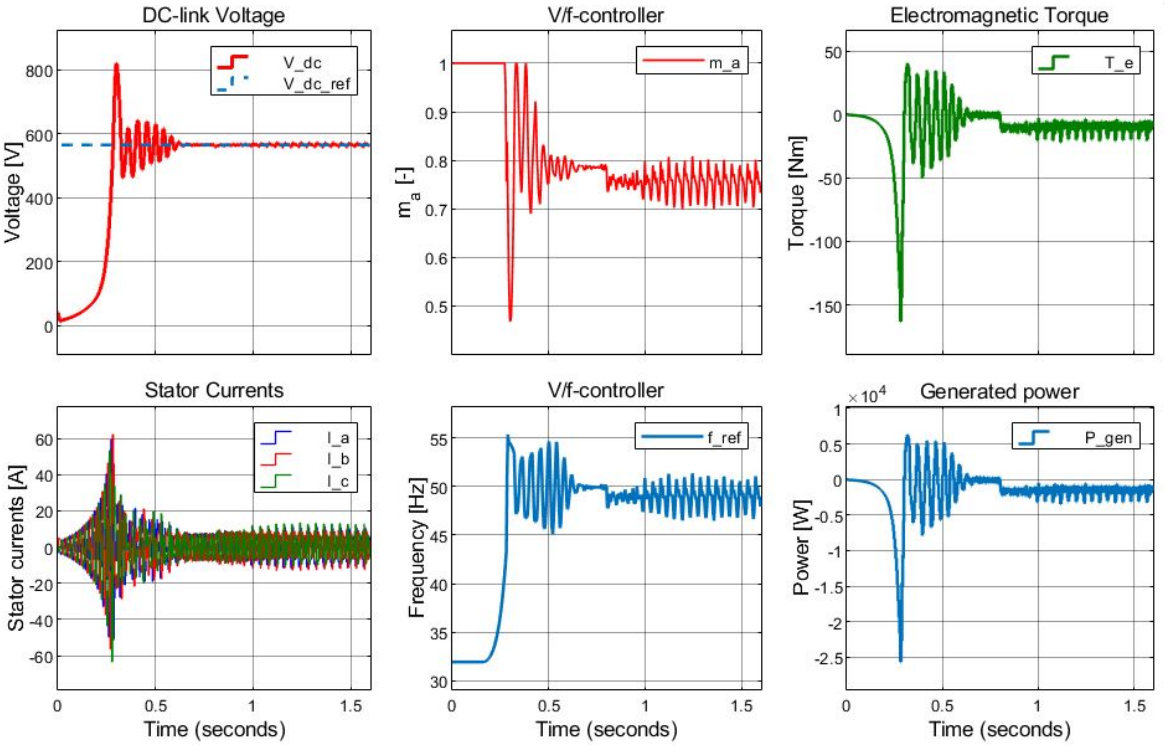

Figure 13.4: #IM4 (5.5 kW) controlled by V/f-control.Magnetization process and a load step of 1.5 kW at 0.8 s is applied. Better tuning of controller parameters could be done to achieve stability.

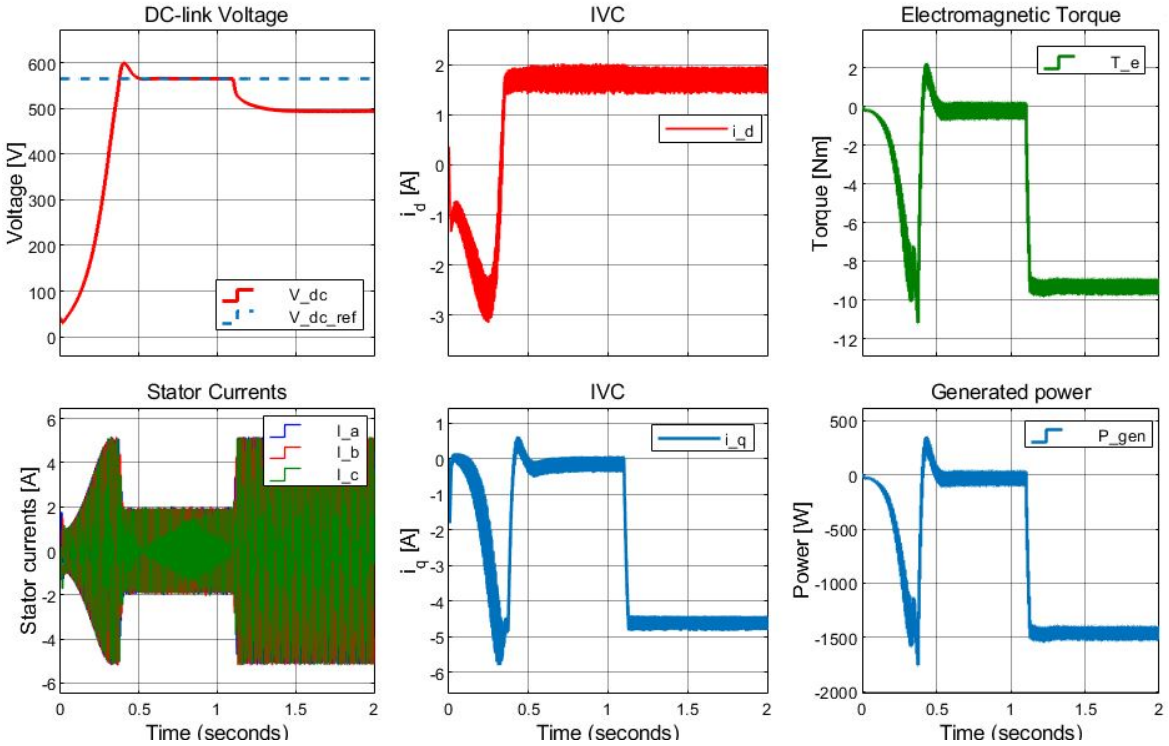

Figure 13.5: #IM1 (1.5 kW) controlled by IVC. Magnetization process and a load step of 1.5 kW at 1.15 s is applied. The machine become overloaded and the DC-voltage reduces.

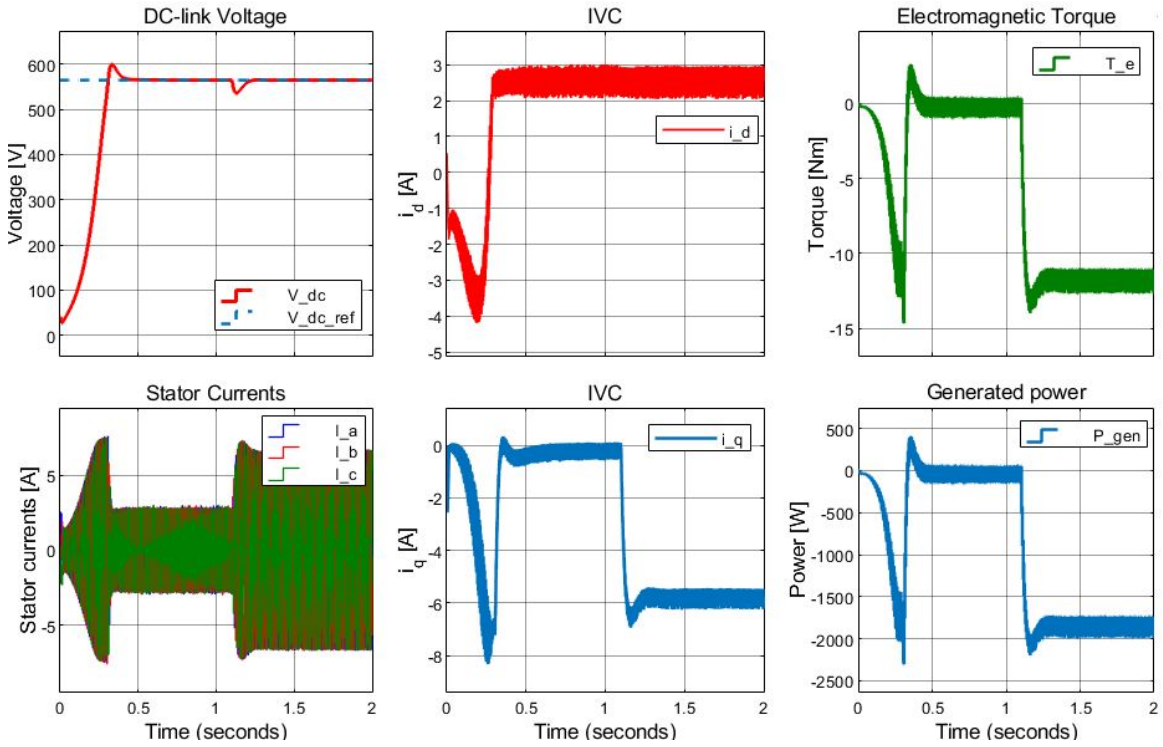

Figure 13.6: #IM2 (2.2 kW) controlled by IVC. Magnetization process and a load step of 1.5 kW at 1.15 s is applied . The machine can maintain the DC-link voltage.

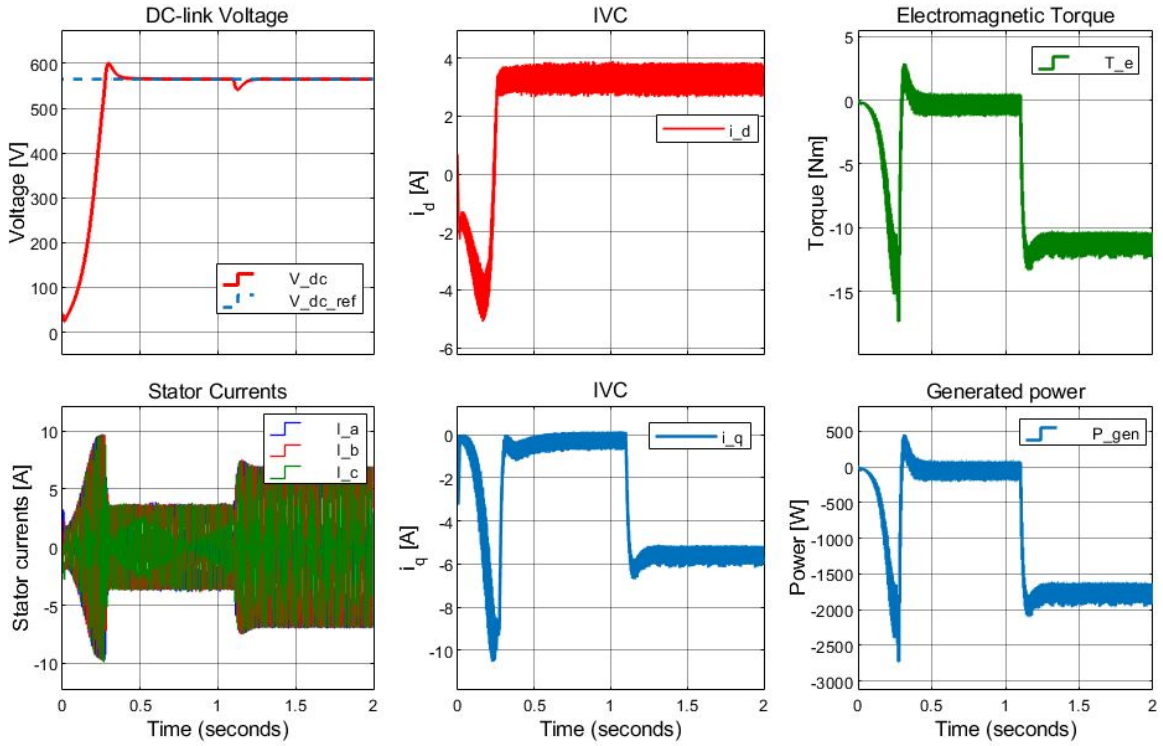

Figure 13.7: #IM3 (3.0 kW) controlled by IVC. Magnetization process and a load step of 1.5 kW at 1.15 s is applied.The machine can maintain the DC-link voltage.

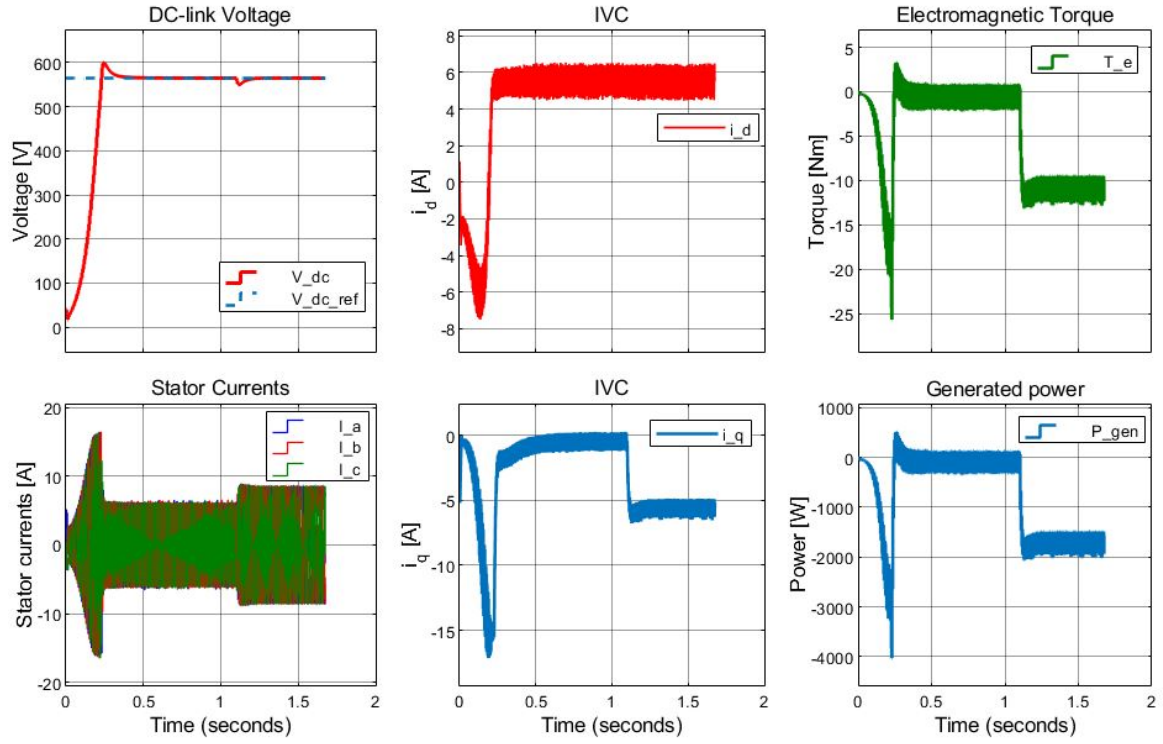

Figure 13.8: #IM4 (5.5 kW) controlled by IVC. Magnetization process and a load step of 1.5 kW at 1.15 s is applied. The machine can maintain the DC-link voltage.

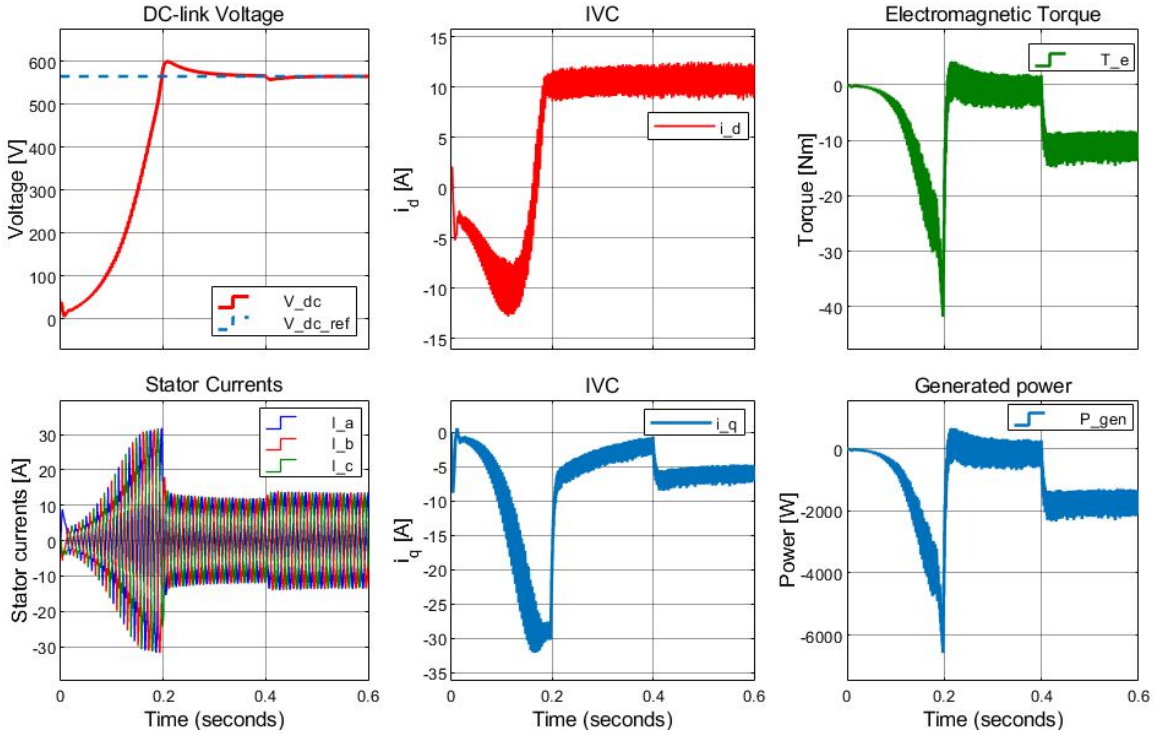

Figure 13.9: #IM5 (11 kW) controlled by IVC. Magnetization process and a load step of 1.5 kW at 0.4 s is applied. The machine can maintain the DC-link voltage, but the stator currents are unnecessarily high.

13.2 Test 2: Dependency of Rotor Time Constant, T_r

The indirect vector control (IVC) approach relies on the rotor parameters r_r, L_m and L_{lr} of the machine to determine the rotor time constant, T_r. T_r is used to estimate the slip speed that is used to obtain the rotor flux position, θ_e. Test 2 investigates how any inaccuracy in the rotor time constant affects the indirect vector control approach. The equation for the rotor time constant 10.9 is repeated here as 13.1:

$$T_r = \frac{L_m + L_{lr}}{r_r} \tag{13.1}$$

The slip speed, ω_{sl}, is in IVC calculated by:

$$\omega_{sl} = \frac{i_q^*}{i_d^*} \cdot \frac{1}{T_r} \tag{13.2}$$

The magnetizing inductance, L_m, changes in accordance with the magnetization characteristic of the machine, and consequently it can be considered to be a state variable. The rotor resistance increases with temperature and the rotor leakage inductance, L_{lr}, can be altered by e.g. changing speed, and thus also these must be considered to be state variables. Usually, the parameters used to calculate T_r in IVC have some inaccuracy from the actual parameter value in the induction machine at the the actual operating state.

Test 2 is performed by using the same procedure as in Test 1: Magnetization and charge up of DC-link (1) and a load step from no-load to 1.5 kW (2), both performed while rotating at constant speed. It is only #IM2 being investigated in Test 2 to illustrate the issue. The other machines would have similar findings with respect to dependency of parameters and T_r. A total of five different rotor time constants in the range of $\left(\frac{1}{2}, 4\right)$ times the theoretical rotor time constant, T_r, have been investigated. The theoretical value of T_r is set to 0.111 s as indicted for #IM2 in Table A.4.

During magnetization and charge-up of DC-link, the machine charges up with a minor overshoot for all values of the rotor time constant. The overshoot, charging time and settle time are shown in Table 13.6. Generally the response seems to be somewhat slower when T_r increases,. The settle time at $\frac{T_r}{2}$ is a bit higher because of some oscillations before settling.

Table 13.6: Peak voltage, charge up and settling time for DC-link voltage for #IM2 with varying T_r.

$\mathbf{T_r}$	**Overshoot**	**Peak DC-voltage**	**Charging time**	**Settle time**
$\frac{T_r}{2}$	5.31 %	595 V	0.246 s	0.366 s
$\frac{3T_r}{4}$	7.26 %	606 V	0.253 s	0.343 s
T_r	6.19 %	600 V	0.306 s	0.405 s
$\frac{3T_r}{2}$	4.60 %	591 V	0.471 s	0.530 s
$4T_r$	1.41 %	573 V	1.036 s	1.233 s

When a load step of 1.5 kW is applied to #IM2, Table 13.7 shows that for a too low value of T_r (i.e. $\frac{T_r}{2}$) the DC-link voltage is unable to settle at the reference again. This is because the machine is unable to produce the required torque needed for the load demand, and consequently the DC-link voltage drops and the requirements for load side voltage are not able to be met. Figure 13.10 shows that the active current saturates and torque become unable to increase the DC-link voltage. The settle time is set to ∞ in Table 13.7.

Using rotor time constants of $\frac{3}{4}$, 1 and $\frac{3}{2}$ times the theoretical value T_r = 0.111 s result in a stable operation for the test case where the mechanical speed remains constant (Table 13.7).

A rotor time constant of 4 T_r causes a slip speed that reaches the pullout torque of #IM2. At the speed of maximum slip, the magnetizing of the machine collapses. Figure 13.12 shows how the DC-link voltage gradually falls from its reference voltage 565 V to 0 within 5 seconds, as the DC-link capacitor is discharging. The settle time is set to ∞ in Table 13.7 since the voltage collapses. Figure 13.12 also shows that current, power and electromagnetic torque stabilize at zero.

Table 13.7: DC-link voltage drop and settling time for #IM2 controlled by IVC with varying T_r

T_r	Drop	Drop DC-voltage	Settle time
$\frac{T_r}{2}$	-21.95 %	441 V	∞
$\frac{3T_r}{4}$	-6.29 %	537 V	0.150 s
T_r	-5.13 %	536 V	0.095 s
$\frac{3T_r}{2}$	-4.78 %	538 V	0.082 s
$4T_r$	-100 %	0 V	∞

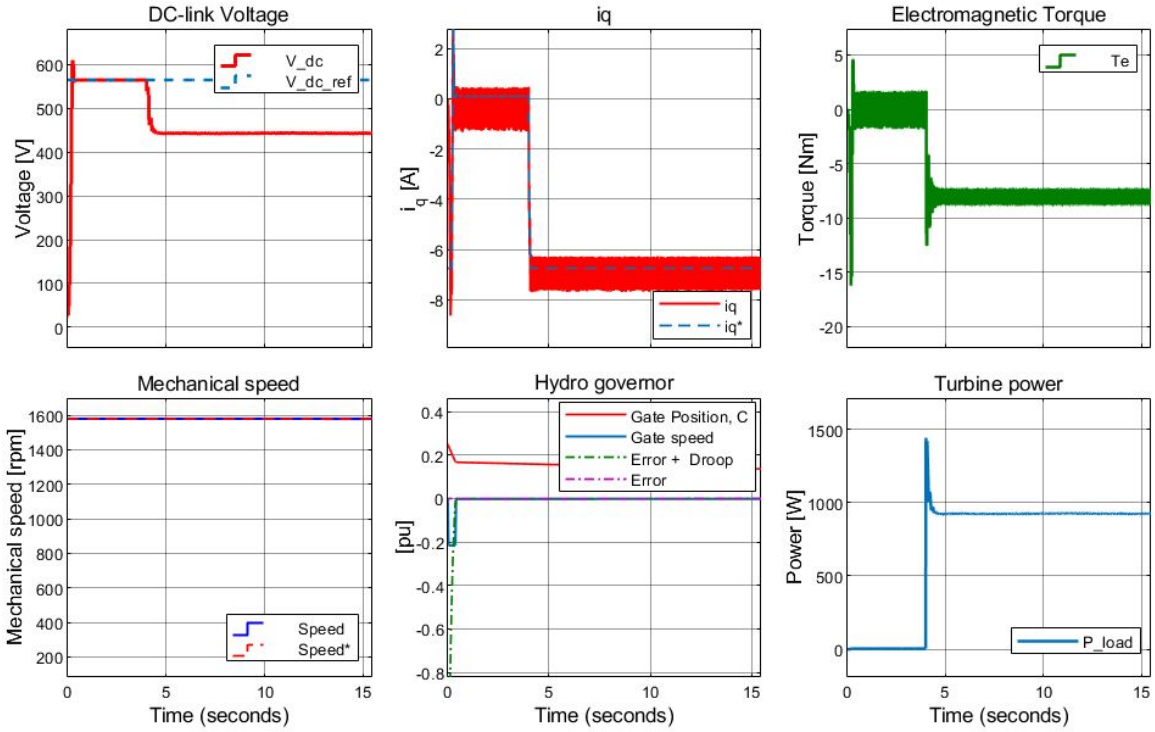

Figure 13.10: #IM2 with IVC and $\frac{T_r}{2}$. Constant speed.

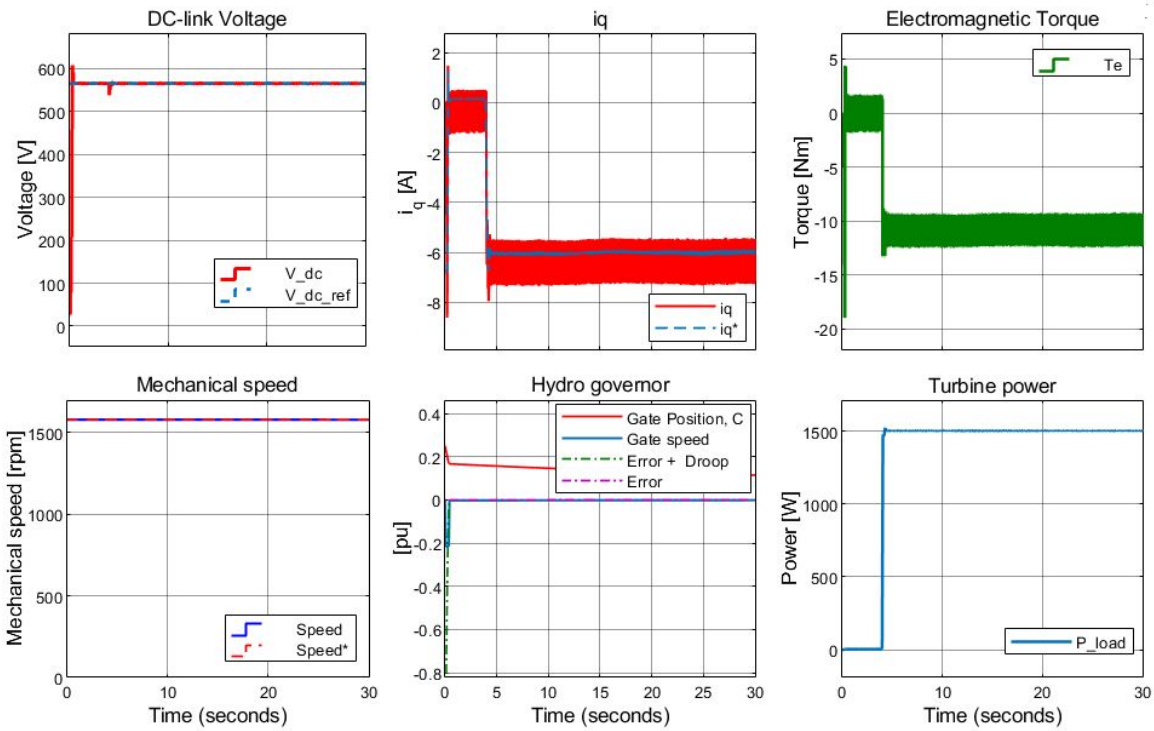

Figure 13.11: #IM2 with IVC and $\frac{3T_r}{4}$. Constant speed.

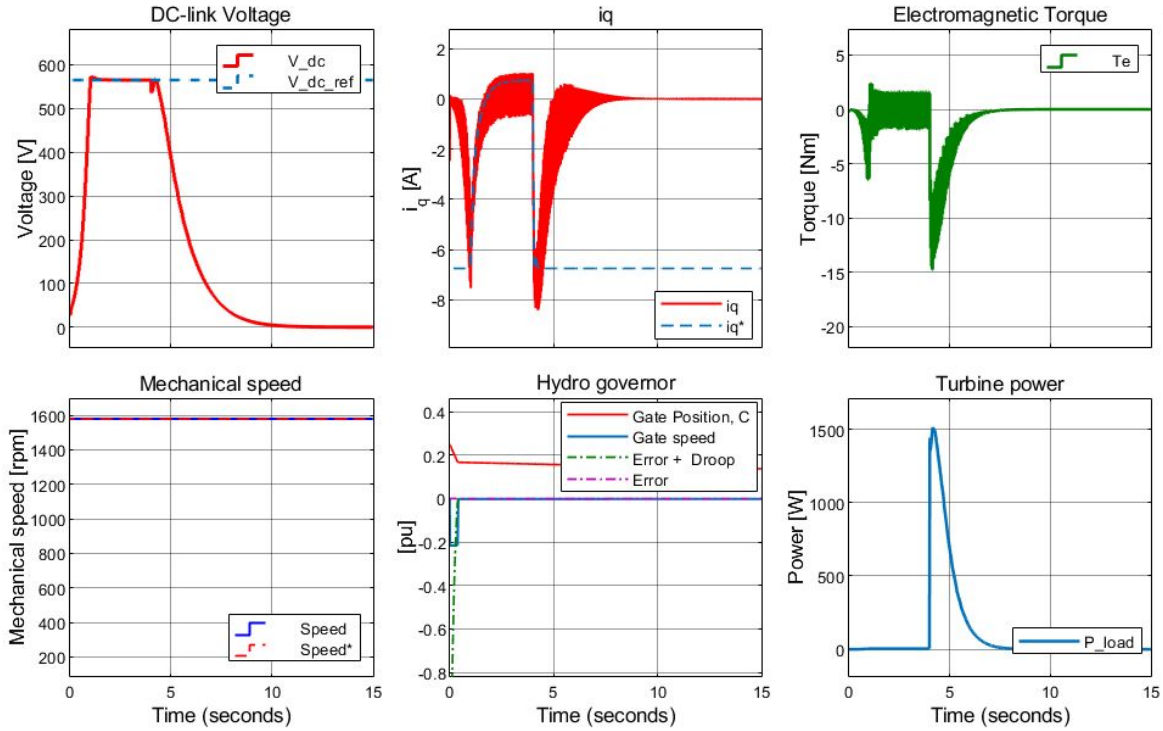

Figure 13.12: #IM2 with IVC and $4T_r$. Constant speed

13.3 Test 3: Hydraulic Turbine Governor Model

In a realistic isolated system with the 2.2 kW hydraulic turbine model,[4] the mechanical speed will not be constant during the magnetization (DC-link charge-up process) and during load steps. This is due to slower hydraulic response than electric response. The influence of total moment of inertia (generator-turbine set) and the generator power ratings is investigated in Test 3. The mechanical shaft speed, ω_r, is changing by the the following relation:

$$\frac{d}{dt}\omega_r = \frac{1}{2H} \cdot (\tau_e - F\omega_r - \tau_m) \tag{13.3}$$

where H is the inertia constant given by $\frac{J_{tot} \cdot \omega_s^2}{S_n}$, F is the friction coefficient set to 0.0184 kg m^2/s to compensate for rotational losses. τ_e and τ_m are the electromagnetic and mechanical torques, respectively.

The 2.2 kW hydraulic turbine (turgo turbine) is run up in speed to the mechanical speed, ω_s, which will give an electric frequency 50 Hz at the nominal slip of generator. For #IM3, the nominal slip is 5.33 % and hence the mechanical reference speed becomes 1580 rpm. The initial gate opening in the turbine model is set to 0.25 pu and the maximum gate changing ratio, G_{lim}, is ± 0.216 pu/s. The total moment of inertia is J_{tot} = 0.0064 kg m^2 for turbine-generator set #IM3 with no additional flywheel. The impact of machine rating and the machine inertia might be large (Equation 13.3). Consequently, also #IM2 and #IM4 and two additional tests of #IM3 with a flywheel that fivefold (Flywheel 1) and tenfold (Flywheel 2) the total moment of inertia, J_{tot} are done. The radius of these flywheels are based on the procedure described in Appendix C and calculated to be 36.2 cm and 40.1 cm, respectively. For simplicity, the tests are done with IVC and $i_d^* = \frac{I_n}{2}$ = const. This will cause larger stator currents at no-load and at low loading, and thus lower the efficiency at these conditions. However, the benefits of utilizing the generators ability to handle a large load step is increased by the high i_d^*.

13.3.1 Magnetization and DC-link Charge-Up

Table 13.8: Test 3: Gate positions and inertia

Machine	$P_{gen,nom}$	G_{init}	$G_{no-load}$	G_{max}	J_{tot}
#IM2	2.2 kW	0.25 pu	0.212 pu	0.450 pu	0.0053 kgm^2
#IM3	3.0 kW	0.25 pu	0.203 pu	0.514 pu	0.0064 kgm^2
#IM4	5.5 kW	0.25 pu	0.162 pu	0.694 pu	0.0110 kgm^2
#IM3 + Flywheel 1	3.0 kW	0.25 pu	0.203 pu	0.203 pu	0.0319 kgm^2
#IM3 + Flywheel 2	3.0 kW	0.25 pu	0.203 pu	0.271 pu	0.0638 kgm^2

To initialize the simulation of magnetization and the DC-link charge-up process, a trial-and-error method has been used to find the above conditions that give a satisfying response for turbine-generator set of #IM3 without any additional flywheel. The speed must not drop to zero during charge-up, and in addition the speed must be damped to the nominal value when the DC-link becomes charged. Thus, the initial gate position at G_{init} = 0.25 pu is a compromise. Table 13.8 shows some gate

[4]SUNECO 2.2 kW Turgo Turbine Model: XJ25-2.2DCT4-Z

positions and total moment of inertia for the tests performed in Test 3. The steady state gate position stabilizes at approximately 0.2 pu. This is because the system contains rotational losses and no-load stator losses. Table 13.13 shows the behavior of the speed and DC-link voltage during the charge up process. It is seen that a larger machine is heavier (needs more energy) to magnetize and thus the speed-drop and DC-rest time is larger for the larger machines. Consequently, the maximum gate opening, G_{max}, reaches high values before it is reduced again, and the machine is quickly run into high speed (overshoot). Within 4-7 seconds (after simulation start) the speed stabilizes at its reference.

The governor performance for #IM3 is shown in Figure 13.15. Initially, the speed error is 0 and the droop given by the initial gate position causes an decrease in gate position. When the speed drops, the gate changing ratio saturates at the limit. The excitation and DC-link charge up processes go on at a varying and low speed and require a high energy supply in order to complete. When charge-up is complete, the power consumption reduces and the turbine-generator set runs up. The gate changing ratio saturates at the negative limit before the set slows down to steady state. Figure 13.15 also shows how the speed error is reduced by the droop functions to accommodate the peculiar response of the hydraulic turbine.

Table 13.9: Test 3: Speed and DC-link behaviors

Machine	**Nominal speed**	**Speed-drop**	**Speed Overshoot**	**Speed Reset**	**DC-peak**	**DC-reset**
#IM2	1580 rpm	204 rpm	2100 rpm	4.01 s	601 V	1.281 s
#IM3	1585 rpm	169 rpm	2211 rpm	4.75 s	603 V	1.583 s
#IM4	1550 rpm	94 rpm	2482 rpm	6.385 s	608 V	2.444 s
#IM3 + Flywheel 1	1585 rpm	855 rpm	1712 rpm	6.49 s	606 V	0.386 s
#IM3 + Flywheel 2	1585 rpm	1254 rpm	1667 rpm	4.48 s	603 V	1.702 s

The speed and voltage profiles in Figure 13.16 show how the DC-link becomes charged when the turbine generator set is running at a lower speed and the speed overshoot that occurs after the DC-link is charged. With constant i_d^* (magnetization), the electromagnetic torque follows the shape of i_q. As expected, a high electromagnetic torque is applied during charge up. Figure 13.17 - Figure 13.14 show these properties for #IM3 with fivefold inertia and for #IM2. For fivefold inertia, the speed response is slower, but the speed deviation is significantly lower.

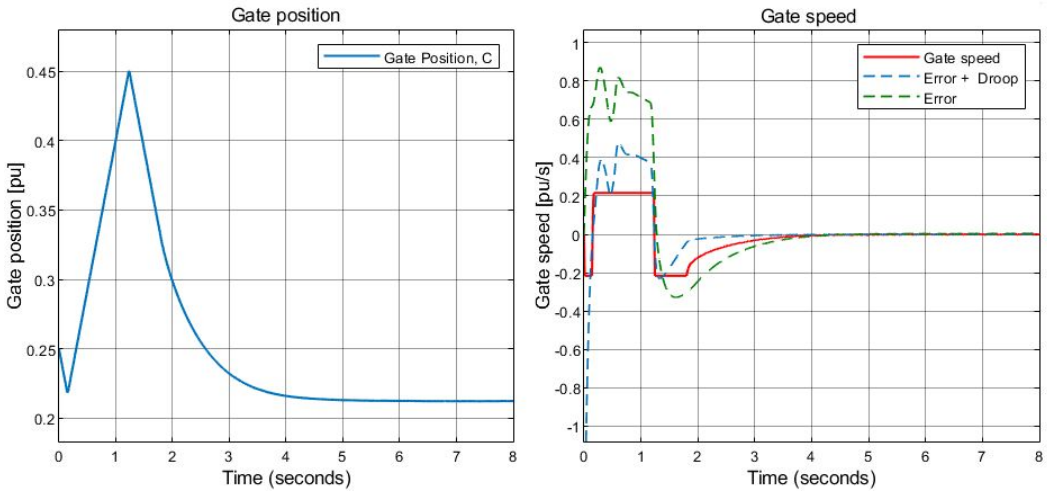

Figure 13.13: Gate position and governor behaviors during charge up for #IM2 (2.2 kW). The gate position speed is limited to 0.216 pu/s

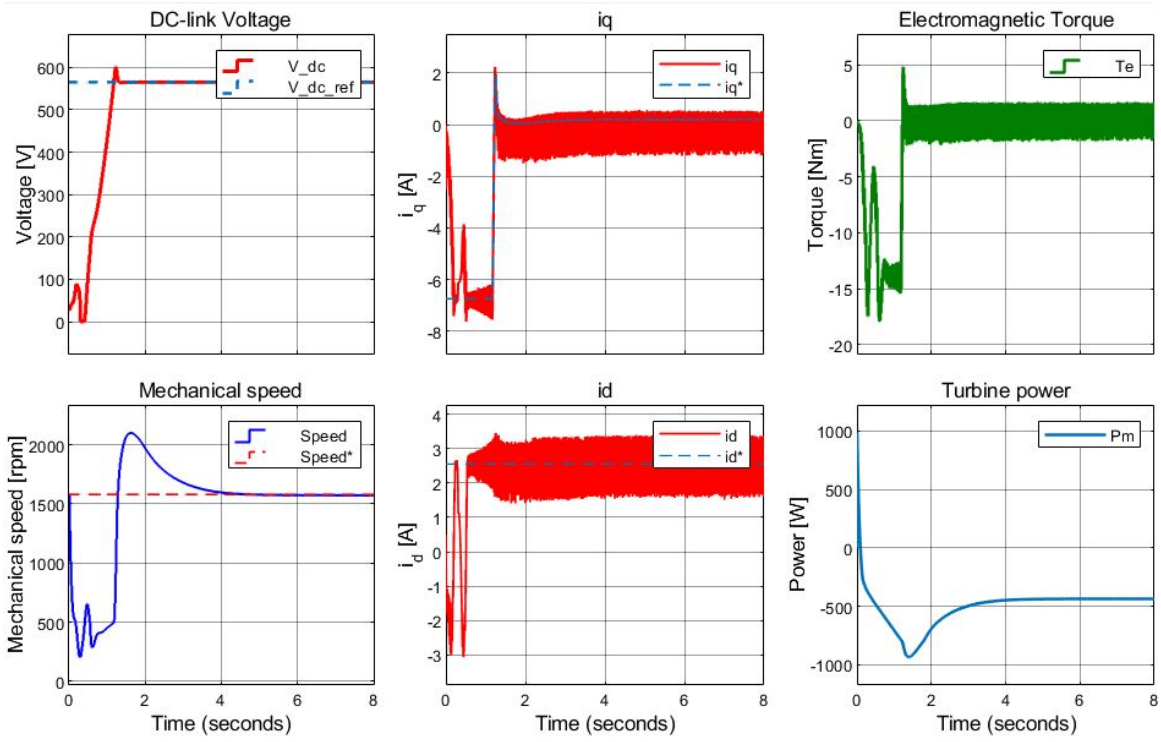

Figure 13.14: Charge up #IM2 (2.2 kW)

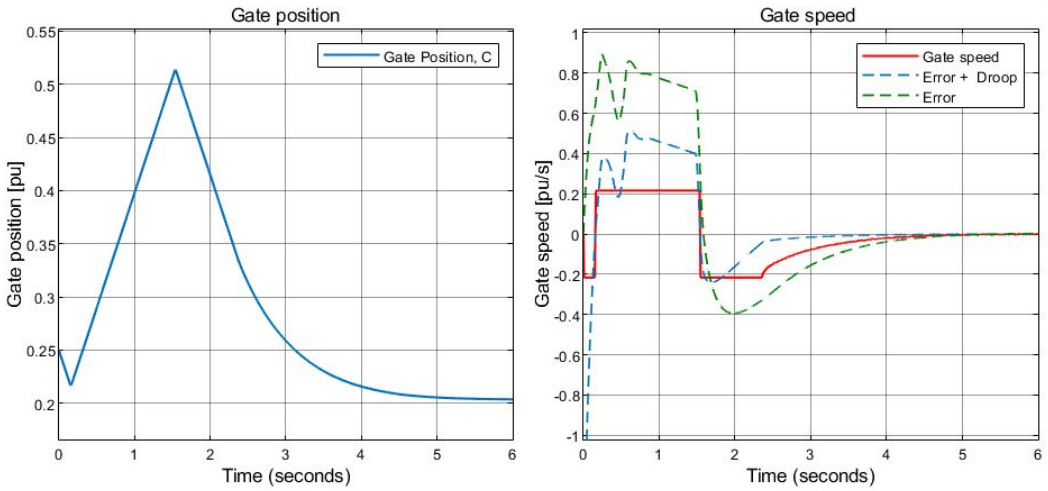

Figure 13.15: Gate position and governor behaviors during charge up. #IM3 (3.0 kW). The gate position speed is limited to 0.216 pu/s

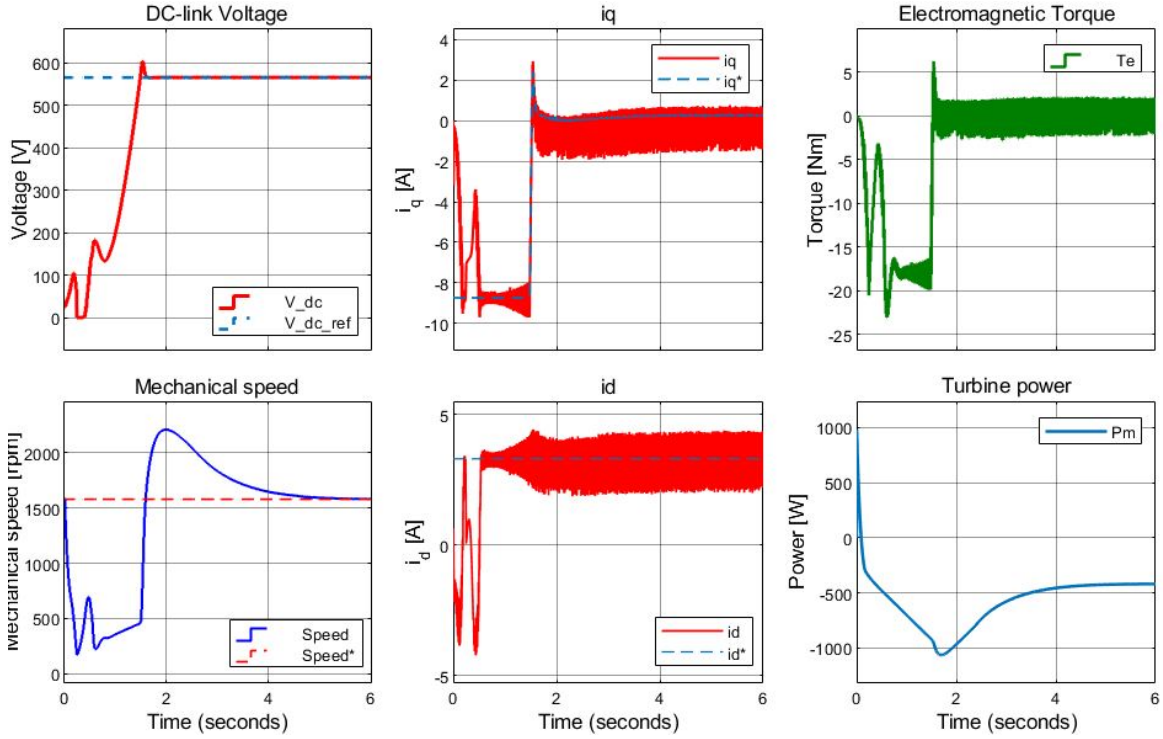

Figure 13.16: Charge up #IM3 (3.0 kW)

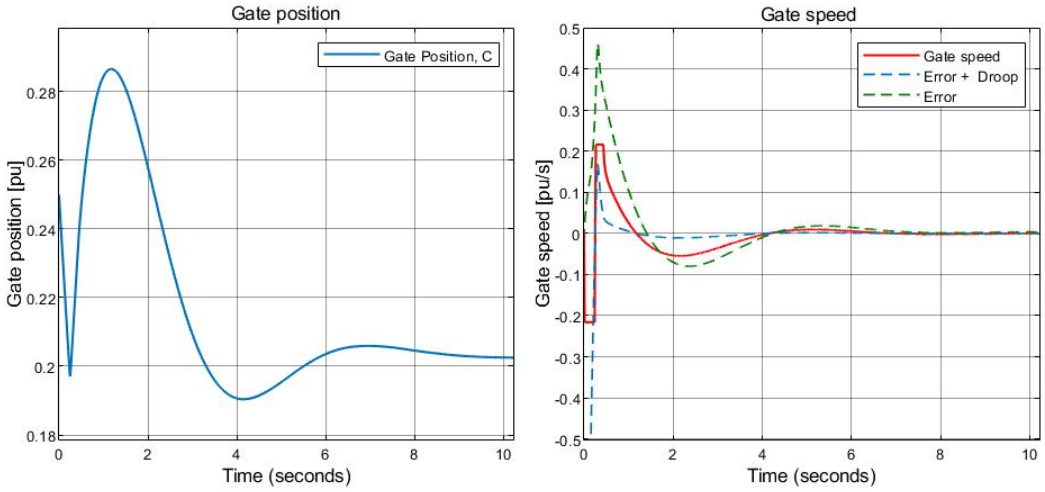

Figure 13.17: Gate position and governor behaviors during charge up. #IM3 (3.0 kW) with fivefold moment of inertia $J_{tot} = 5 \cdot (J_{gen} + J_{turb})$

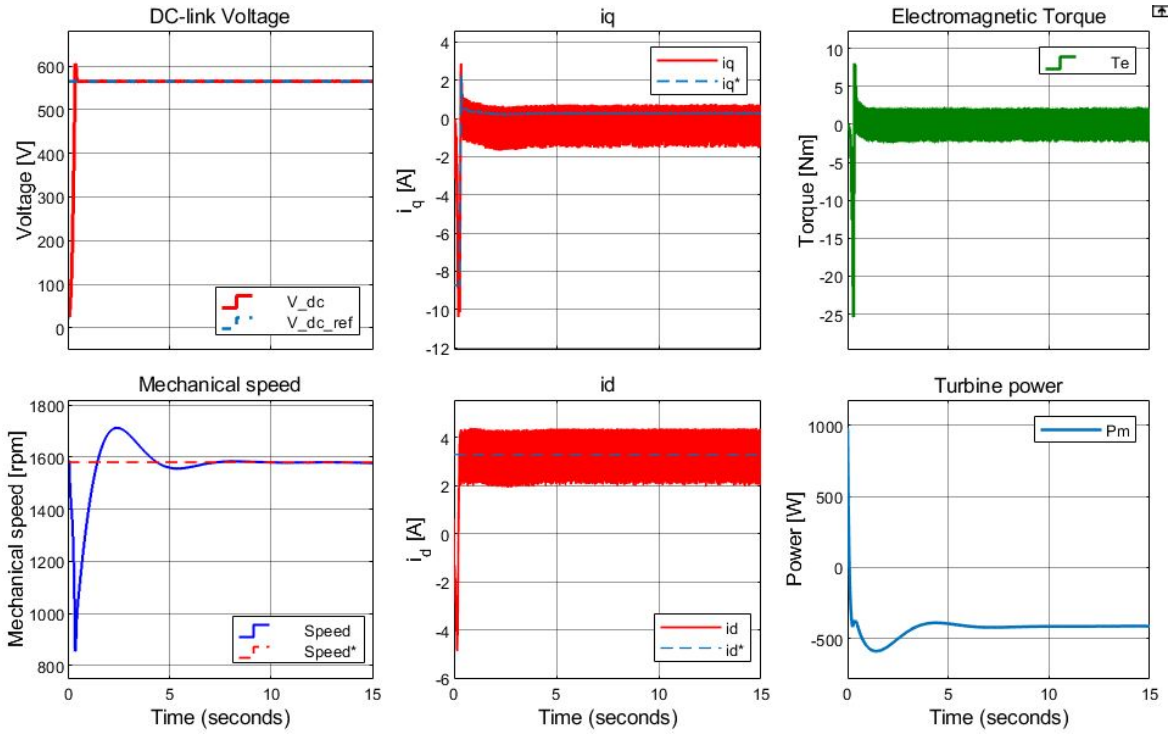

Figure 13.18: Charge up #IM3 (3.0 kW) with fivefold inertia $J_{tot} = 5 \cdot (J_{gen} + J_{turb})$. Note the less speed reduction.

13.3.2 Step-Wise Increase from No-load to Full Load

The second part of Test 3 investigates how the machine inertia influence the system behavior during load steps. The load step could not be large (1.5 kW as in Test 1) since the mechanical torque given by the turbine can not be changed as fast as the electromagnetic torque. By increasing the load step-by-step in a such manner that the turbine speed reaches to catch up, it is possible to go from no-load to full load and maintain stable operation. A load step causing speed drop from the reference and down to more than 1000 rpm can be handled by the turbine and its governor. The generator is controlled by IVC with $i_d^* = \frac{I_n}{2}$ and gets problem in keeping the voltage constant if the speed drops too much (< 1000 rpm). The response from the hydraulic governor containing permanent and transient droop ensures stability with low gain short time after the step and high gain in the steady controlling. It is aimed to not reach the limit of gate changing ratio at 0.216 pu/s in the governor. During those speed variations, the resulting the DC-link voltage is kept relatively constant with a minor voltage drop ($\leq 1\%$), consequently the AC-voltage will be minor affected.

Three simulations have been performed: The step-wise load profile is applied to #IM2, #IM3 and #IM3 with a flywheel that fivefolds the moment of inertia. It is seen that the speed drops becomes highest for #IM2 which has the lowest moment of inertia and decrease with when the moment of inertia is increased. However the speed drops in this range is affecting the DC-link voltage significantly. During a step wise load rejection the speed deviation will be in the opposite direction, in other words the speed overshoots to a value higher than the reference speed before it stabilizes by the governor. The rotational losses will damp the overshoot and reset time a bit compared. The DC-link voltage will also have a overshoot instead of drop when the load is rejected.

Table 13.10: Speed drops when applying the step-by-step increase of load demand from 0 to 1.5 kW for generators #IM2, #IM3 and #IM3 + flywheel. All are controlled by IVC

Loading 1 pu = 1.5 kW	**Step Time**	**Speed drop #IM2**	**Speed drop #IM3**	**Speed drop #IM3 + Flywheel**	**DC-drop #IM3 + Flywheel**	$\mathbf{i_q^*}$
0.20 pu	2.0 s	1081 rpm	1132 rpm	1327 rpm	560 V	-0.75 A
0.35 pu	4.0 s	1166 rpm	1225 rpm	1388 rpm	561 V	-1.45 A
0.45 pu	6.0 s	1295 rpm	1339 rpm	1459 rpm	562 V	-1.95 A
0.55 pu	8.0 s	1272 rpm	1328 rpm	1442 rpm	562 V	-2.35 A
0.60 pu	10.0 s	1418 rpm	1448 rpm	1507 rpm	563 V	-2.60 A
0.65 pu	12.0 s	1413 rpm	1445 rpm	1504 rpm	563 V	-2.80 A
0.70 pu	14.0 s	1404 rpm	1445 rpm	1498 rpm	563 V	-3.10 A
0.75 pu	16.0 s	1388 rpm	1440 rpm	1496 rpm	563 V	-3.30 A
0.80 pu	18.0 s	1374 rpm	1435 rpm	1498 rpm	563 V	-3.55 A
0.85 pu	20.0 s	1345 rpm	1427 rpm	1493 rpm	563 V	-3.80 A
0.90 pu	22.0 s	1313 rpm	1417 rpm	1490 rpm	563 V	-4.10 A
0.95 pu	24.0 s	1208 rpm	1409 rpm	1487 rpm	563 V	-4.75 A
1.00 pu	26.0 s	1173 rpm	1390 rpm	1487 rpm	563 V	-4.75 A

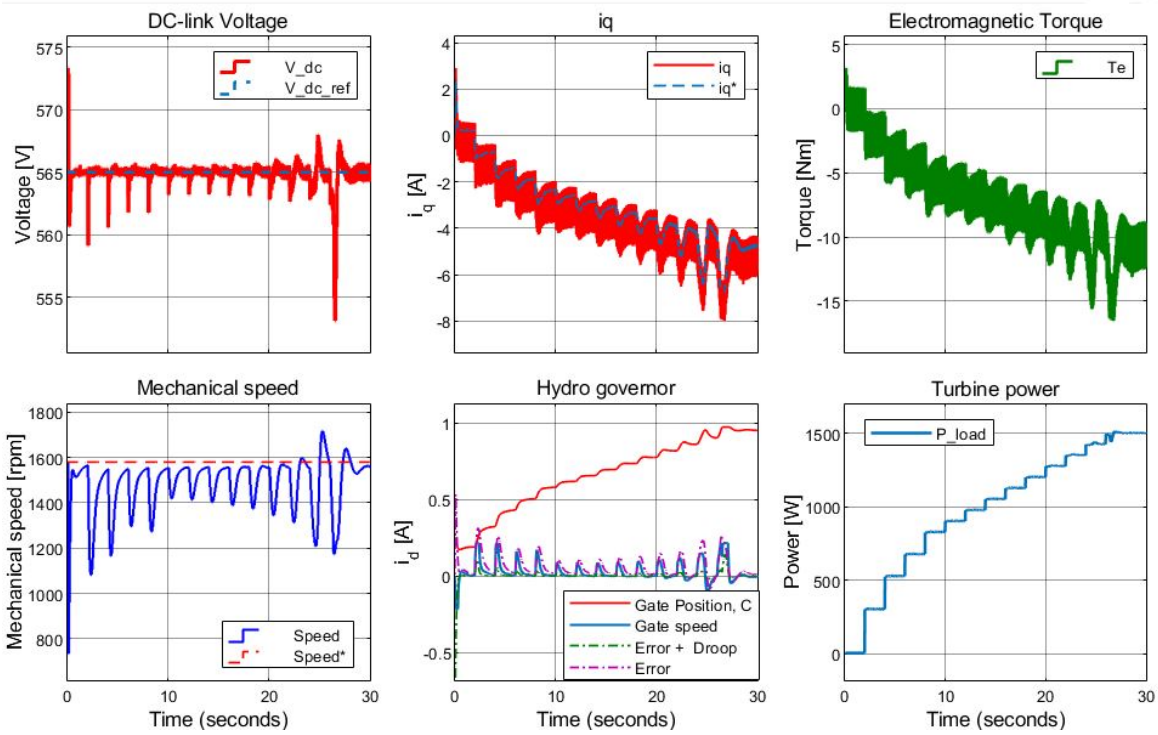

Figure 13.19: Step wise increase from 0 to 1.5 kW for #IM2 (2.2 kW)

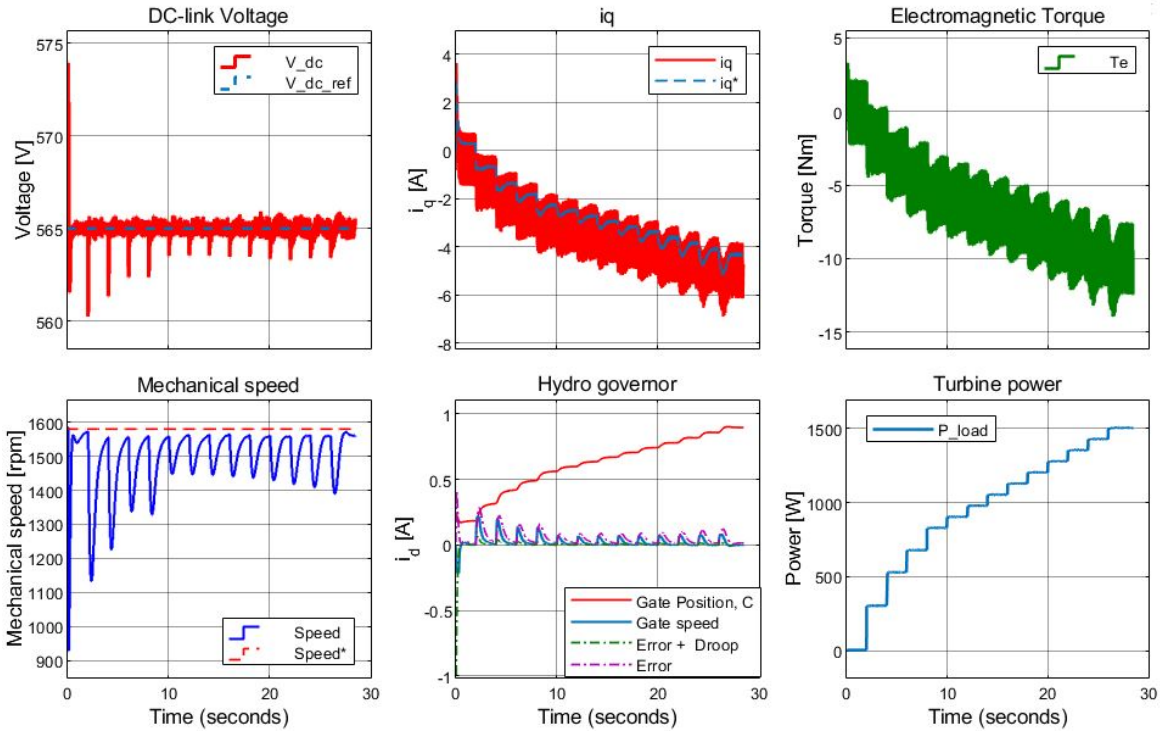

Figure 13.20: Step wise increase from 0 to 1.5 kW for #IM3 (3.0 kW)

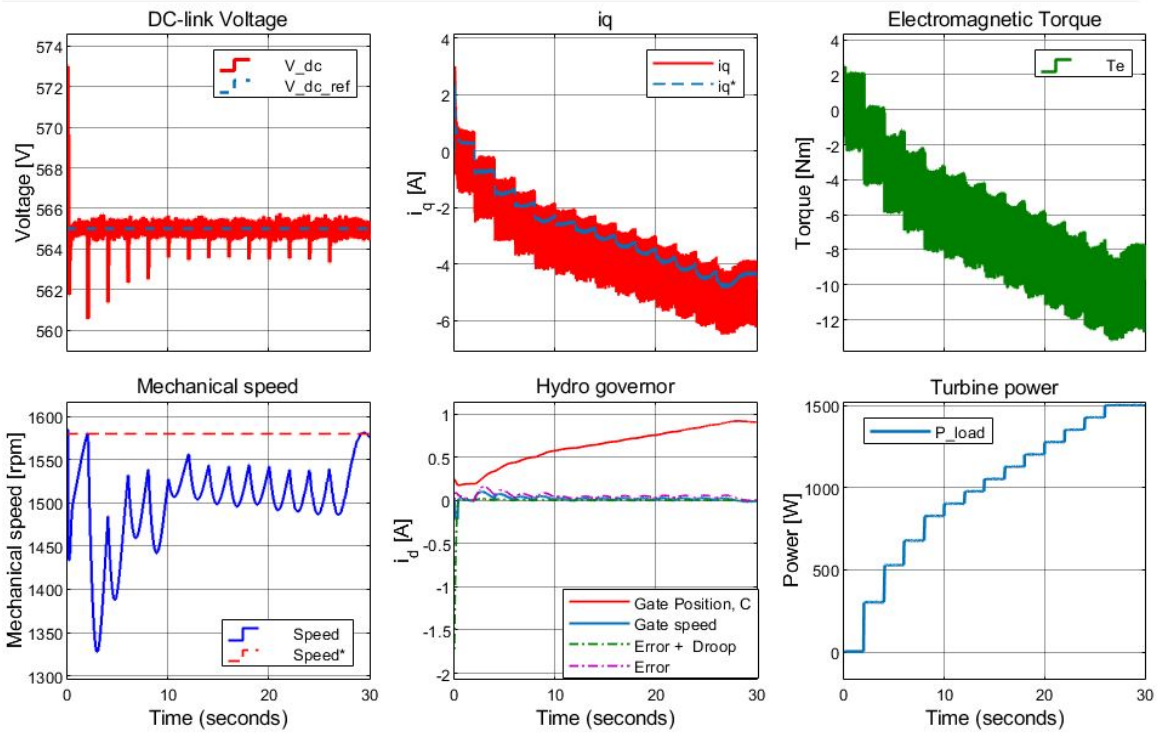

Figure 13.21: Step wise increase from 0 to 1.5 kW for #IM3 (3.0 kW) with a flywheel that fivefolds the total moment inertia: $J_{tot} = 5 \cdot (J_{turb} + J_{gen})$

13.3.3 Larger load steps

If the load steps in the load profile are increased to adding 0.2 per unit power each step throughout the profile, the system will be able to go from 0 to 1 pu in five steps. Here the time between each step is set to be 4.0 seconds. #IM2, #IM3 and #IM5 are investigated.

For #IM2 and #IM3 the speed drops more than for #IM5. It is seen that if the speed drops below 100 rpm the i_q^* current component saturates and the DC-link voltage will drop up to 11.5 % for #IM2 and #IM3. For #IM5 the damping of the speed is slower and the ripple in i_q and thus also the electromagnetic power is high. This makes additional flywheel to an better option if large load steps is required in the system. Table 13.11 shows the measured speed deviations.

Table 13.11: Step-by-step increase of load demand (0-1.5 kW) by steps of 0.2 pu for #IM2, #IM3 and #IM5 (IVC and $i_d^* = \frac{I_n}{2}$)

Loading 1 pu = 1.5 kW	**Step Time**	**Speed drop #IM2**	**Speed drop #IM3**	**Speed drop #IM5**
0.20 pu	4.0 s	1080 rpm	1132 rpm	1348 rpm
0.40 pu	8.0 s	998 rpm	888 rpm	1388 rpm
0.60 pu	12.0 s	786 rpm	990 rpm	1375 rpm
0.80 pu	16.0 s	845 rpm	684 rpm	1370 rpm
1.00 pu	20.0 s	1009 rpm	831 rpm	1359 rpm

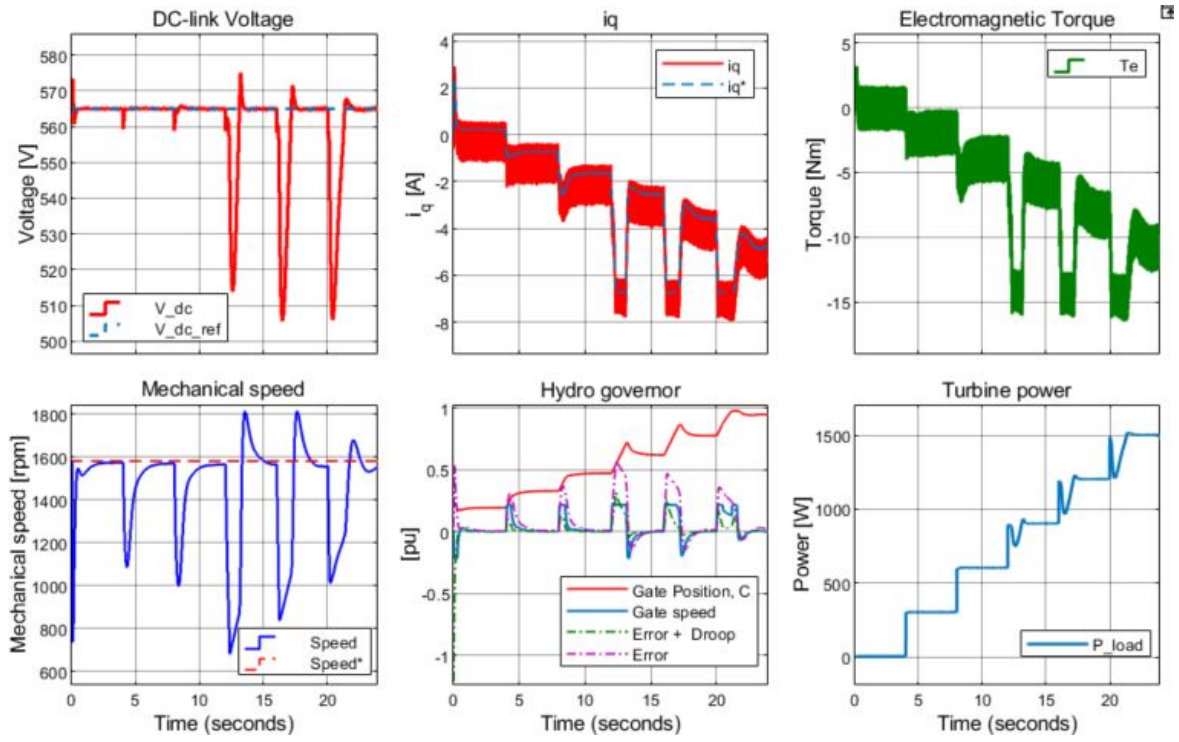

Figure 13.22: Step wise increase from 0 to 1.5 kW for #IM2 (2.2 kW) with load steps of 0.2 pu.

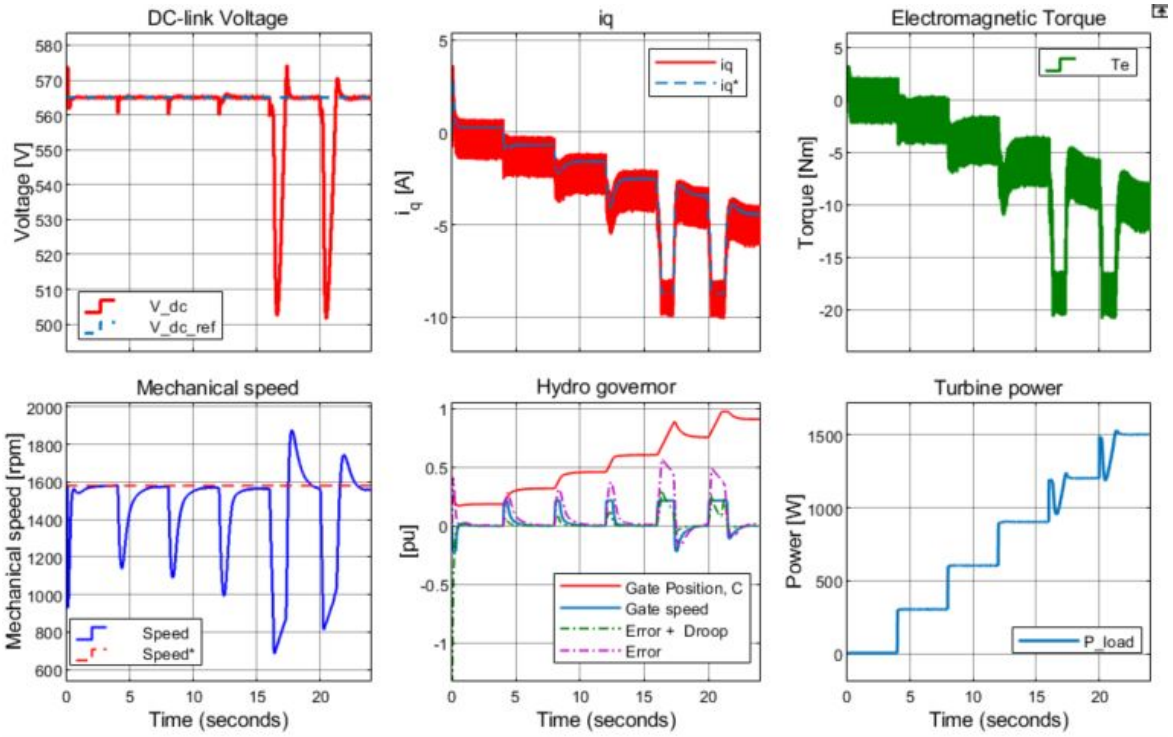

Figure 13.23: Step wise increase from 0 to 1.5 kW for#IM3 (3.0 kW) with load steps of 0.2 pu.

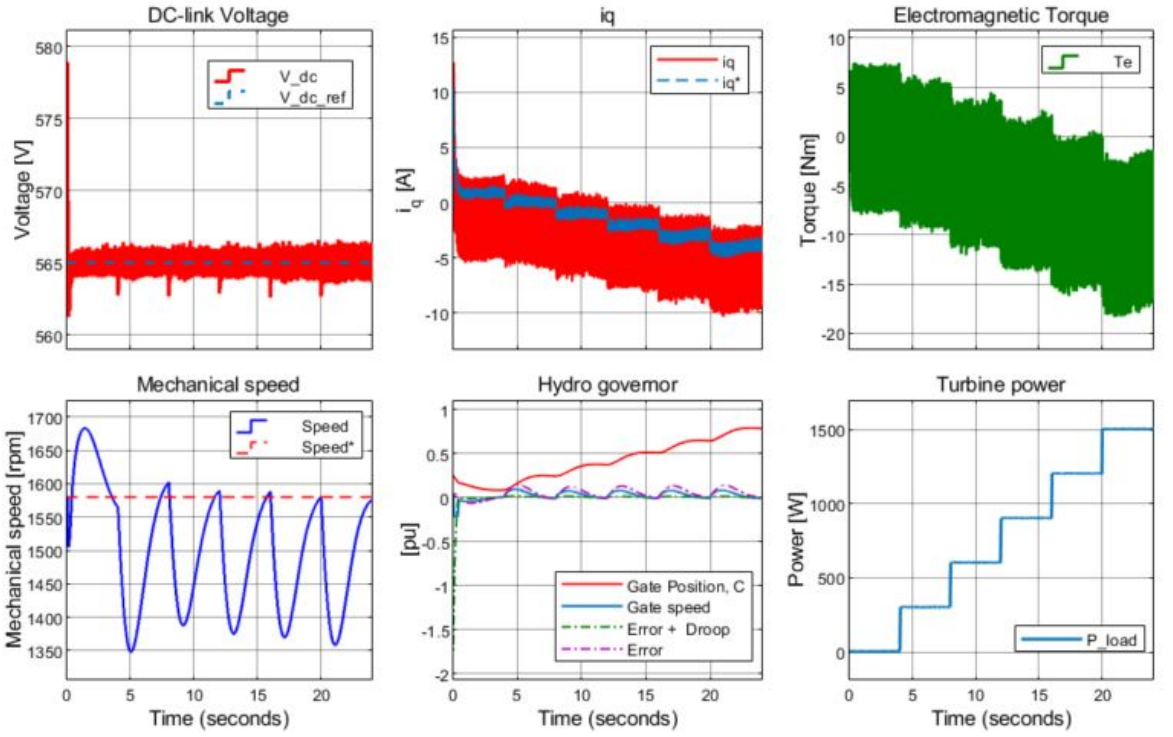

Figure 13.24: Step wise increase from 0 to 1.5 kW for #IM5 (11 kW) with load steps of 0.2 pu.

13.4 Test 4: Load Side Behavior

13.4.1 Resistive load

Test 4 concentrates on the system behaviors at load side. A stiff DC-link voltage at $V_{DC,ref}$ = 656 V is assumed. This is an approximation since the DC-link voltage will vary during larger load steps. The passive LCL-filter components in Table 6.2 is determined in accordance with the design procedure in G.1 based on [24]. A step in the load demand of 1.5 kW is applied at time 0.15 s. The resulting current and voltage profiles are shown in Figure 13.25 and the total harmonic distortion (THD) is showed in Figure 13.26.

Table 13.12: Load voltage and current (RMS) and voltage quality measurements for constant DC-link voltage.

Load **1 pu = 1.5 kW**	$\mathbf{V_{load,\Phi}}$	$\mathbf{V_{load,LL}}$	$\mathbf{V_{VSC,\Phi}}$	$\mathbf{I_{load}}$	$\mathbf{I_{VSC}}$	$\mathbf{f_{load}}$	**THD:** $\mathbf{V_{rms,load,\Phi}}$
0.0 pu	229.7 V	397 V	258 V	0.00 A	0.256 A	49.9 Hz	1.4 %
1.0 pu	229.8 V	398 V	259 V	2.154 A	2.170 A	50.0 Hz	0.75 %

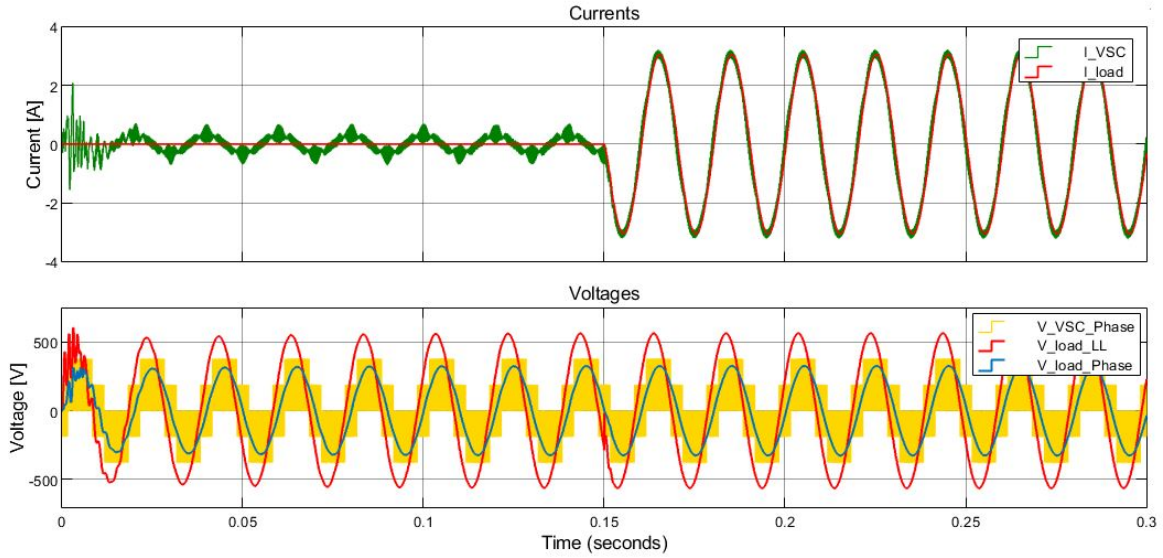

Figure 13.25: Filtered (red) and unfiltered (green) current profiles for one phase (upper). Unfiltered load voltage (yellow), filtered load voltage blue) and filtered line-line voltage (red). Applying a load step of 1.5 kW at 0.15 s. V_{DC} = 565 V = const.

The curves shows that the initialization causes high distortion in the voltage that is quickly damped out by the filter. The no-load THD is at 1.4%. It is seen that a current is flowing through the VSC at no load even though the load current is zero. The current path goes though the inverter side inductor and the grounded filter capacitor. The distortion of the inverter output voltage remains high ($\approx$ 50%). When the load steps, a temporary increase in the distortion is observed, short time afterwards the new steady state is achieved with a THD at 0.75 %. A voltage drop of 29 V across the filter components is achieved. Since the DC-link voltage is stiff for this test, any significant voltage deviations observed. In a real case the drops DC-voltage caused by load steps will propagate to the AC load voltage.

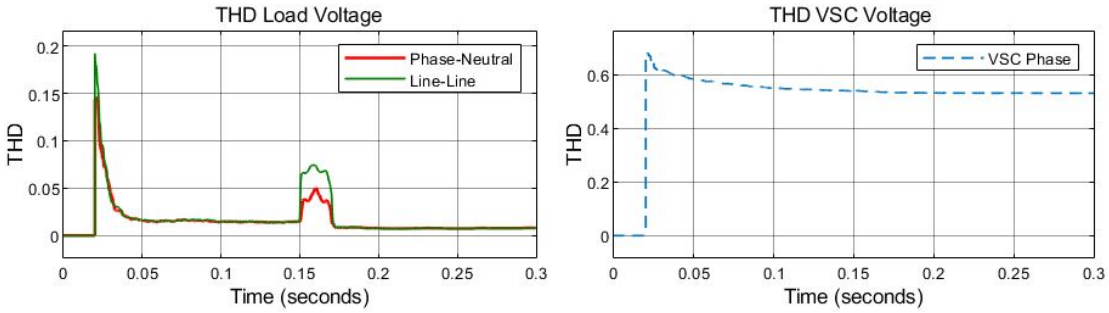

Figure 13.26: Total harmonic distortion in load voltage (left) and unfiltered voltage from VSC (right). Applying a load step of 1.5 kW at 0.15 s. V_{DC} = 565 V = const.

For this ideal case the Norwegian requirements for voltage quality of grid connected low voltage systems at 230 V ± 3.0% RMS and THD < 5.0% are accommodated with good margins. These requirements are taken from *Forskrift om leveringskvalitet i kraftsystemet* [4].

13.4.2 Suggestions for Inductive and Capacitive Loads

In this case the loading has been pure resistive with unity power factor ($\cos\phi$ = 1) [5]. Real cases the load could also be inductive or capacitive with leading or lagging power factor. In a such case the LCL-filter performance might will be slightly different from unity power factor in terms of distortion. In [1] it is found that an inductive power factor increase the filter performance a bit and a similar capacitive power factor increase the distortion of the filter output voltage and hence the filter performance is worse. However it does not affect the systems' ability to meet the given requirements in [4]. This is in accordance with what expected since the LCL-filter design procedure assumes a slightly inductive load.

[5] Apart from any correction due to the harmonic distortion (THD)

13.5 Test 5: Interconnections in the Isolated System as a Whole

In Test 1 - Test 4 above, only parts of the isolated system and its behavior have been included in the simulations and thus tested and investigated. Test 5 simulates the system as a whole (Figure F.1). This is done to include all the connections and relationships between the three control systems: The speed response given by the dynamics of the turbine and governor influences the generators ability to maintain the its excitation and DC-link voltage. This is the main constraints of how fast the system can respond to load changes. The values passive filter components given in Table 6.2 are still used.

13.5.1 Magnetization and DC-link Charge-Up

The initial conditions are similar to the initial conditions in Test 3: The generator is initially running at rated speed. The initial (battery) DC-link voltage at start up is 40 V. Its reference voltage is still 565 V. An additional flywheel is in an approach added to the shaft to increase the total moment of inertia to $5(J_{gen} + J_{turb}) = 0.0319$ kg m^2. The increased moment of inertia that improves the system stability, but leads to longer response time in the speed since more energy is needed to be delivered from the turbine to accelerate the shaft. G_{init} is set to 0.25 pu. The $v_{G,lim}$ is limited to 0.216 pu/s. IVC with $i_d^* = \frac{I_n}{2}$ is used to control the generator.

The load line-line voltage, $V_{LL,load}$ reaches its reference a short time after the DC-link has reached its reference. $V_{LL,load}$ do have a lower overshoot than what V_{DC} has. This is since the load controller scales the modulation index, $m_{a,load}$ down when the DC-link voltage becomes high. Delays in the load controller and filter are the reasons for why the charge up time for the load voltage is a bit longer than the charge-up time for the DC-link voltage. Even though #IM3 by itself has a bit larger moment of inertia the speed drop during magnetization is higher than for #IM2. This is since the energy needed to magnetize the machine increases with the machine power ratings. This is more than the increase of stored energy in the rotating mass. If flywheel 1 with a radius of 36.2 cm is connected to the shaft of #IM3 the moment of inertia will be fivefolded compared to no flywheel connected to the shaft of #IM3. The stored energy in the rotating mass will cause a lower speed drop and the machine are able to magnetize quicker. However for the case with increased inertia more energy is needed from the turbine to accelerate the machine from a given speed deviation. Since the turbine model is equal for all cases and its dynamics have the same limitations it will takes some more time to accelerate the flywheel from 855 rpm to the nominal speed compared to no flywheel. The case with flywheel is favorable since the speed deviation is low and the the charge-up becomes smooth, and the speed overshoot is less. Figure 13.27, 13.28 and 13.29 show system behavior during the charging process. The load-side behaviors during the charge up and magnetization process in terms of RMS-current and voltage, instantaneous current and voltages of phase A and the distortion of load voltage (THD) are showed in Figures 13.30, 13.31 and 13.32. It is seen that there is a voltage drop across the filter and that there is a no-load leakage current of 0.26 A through the filter capacitor.

Table 13.13: Test 3: Speed and load voltage behaviors during charge up. Whole system is interconnected and IVC with $i_d^* = \frac{I_n}{2}$ is used.

Machine	**Nominal speed**	**Speed-drop**	**Speed Overshoot**	**V_{DC} Charge up**	**$V_{LL,Load}$ Charge up**
#IM2	1580 rpm	200 rpm	2140 rpm	1.185 s	1.204 s
#IM3	1585 rpm	162 rpm	2220 rpm	1.356 s	1.414 s
#IM3 + Flywheel 1	1585 rpm	842 rpm	1710 rpm	0.286 s	0.306 s

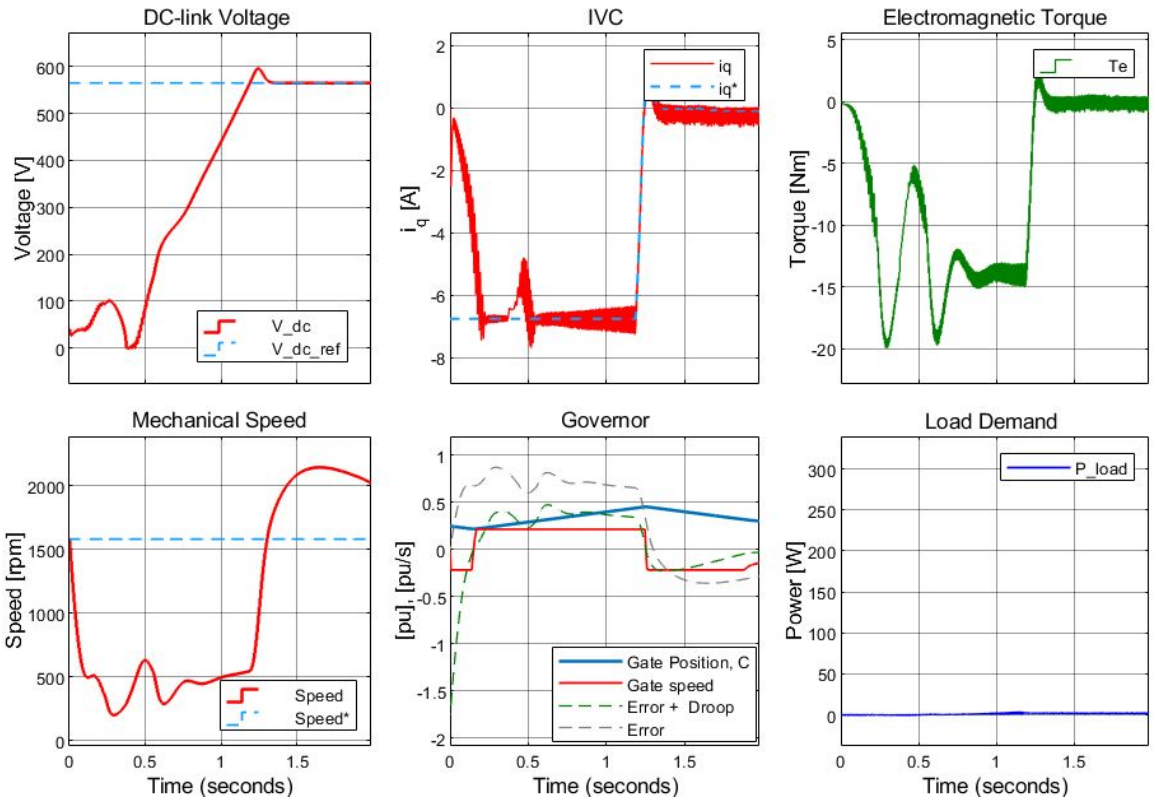

Figure 13.27: Magnetization and charge-up process of generator #IM2 (2.2 kW)

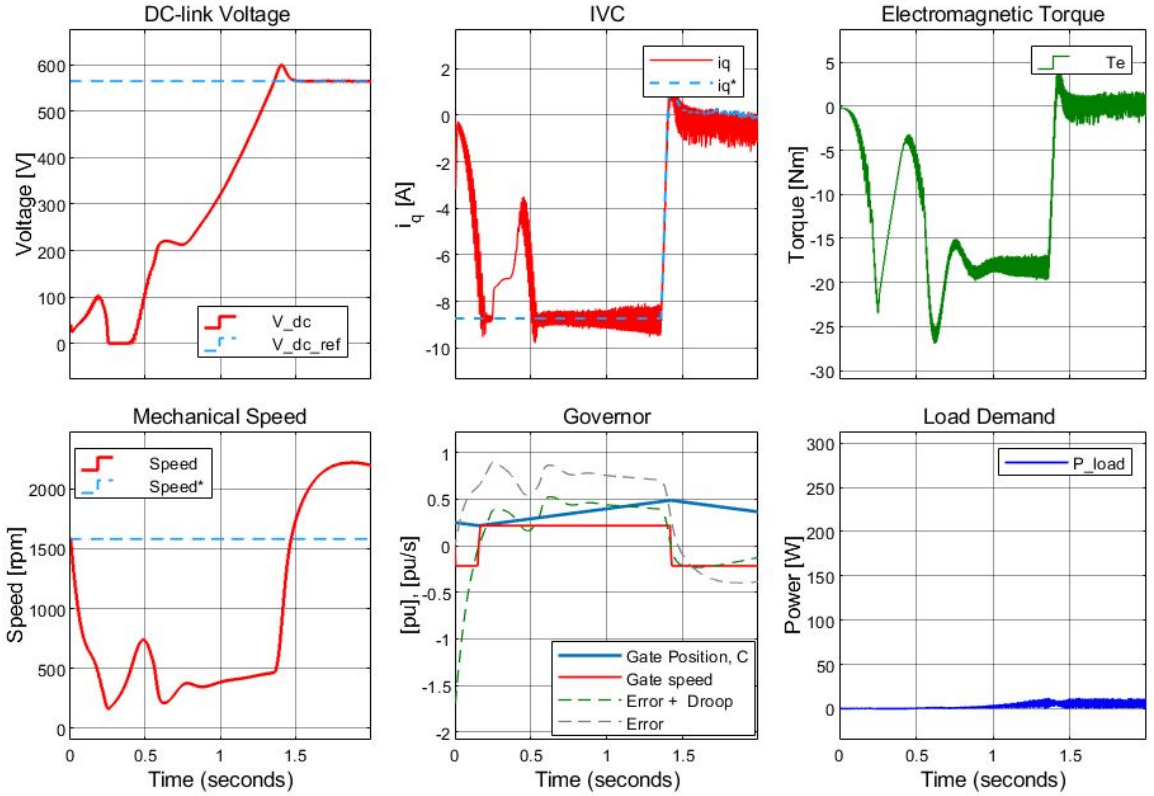

Figure 13.28: Magnetization and charge-up process of generator #IM3 (3.0 kW)

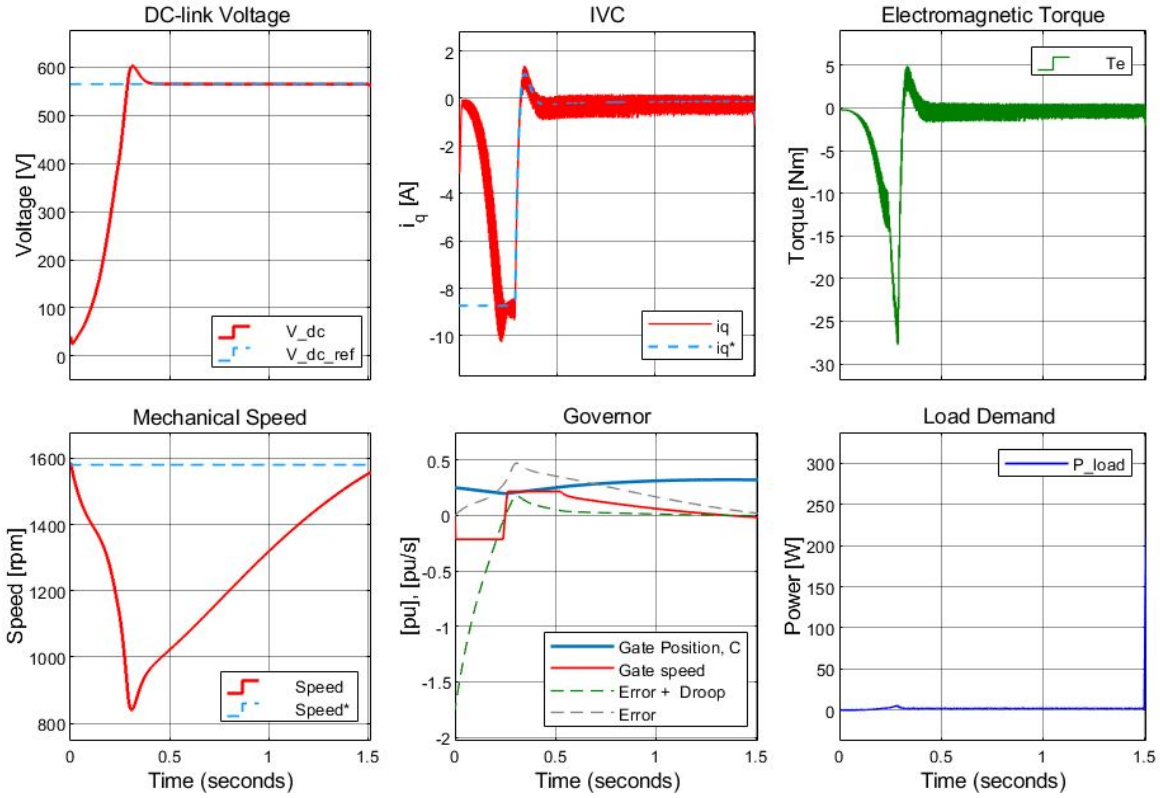

Figure 13.29: Magnetization and charge-up process of generator #IM3 (3.0 kW) with an additional flywheel

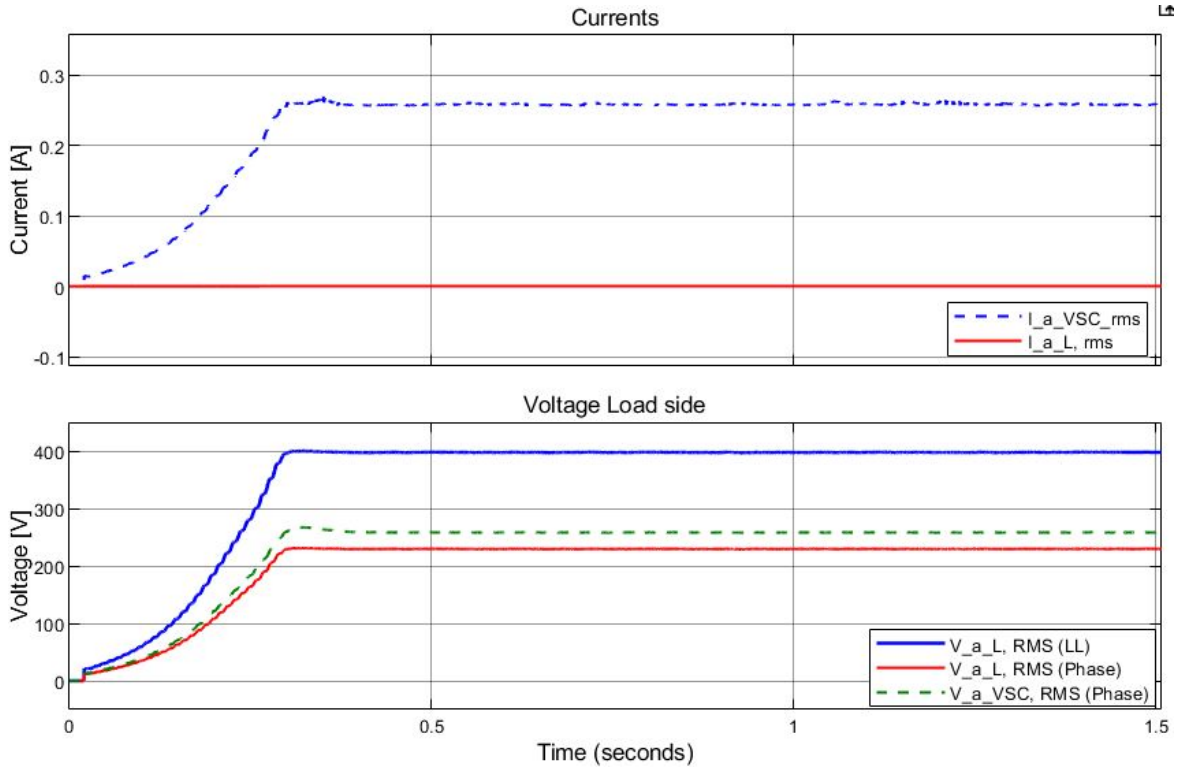

Figure 13.30: RMS currents and voltages at load side during magnetization for #IM3 (3.0 kW) with an additional flywheel.

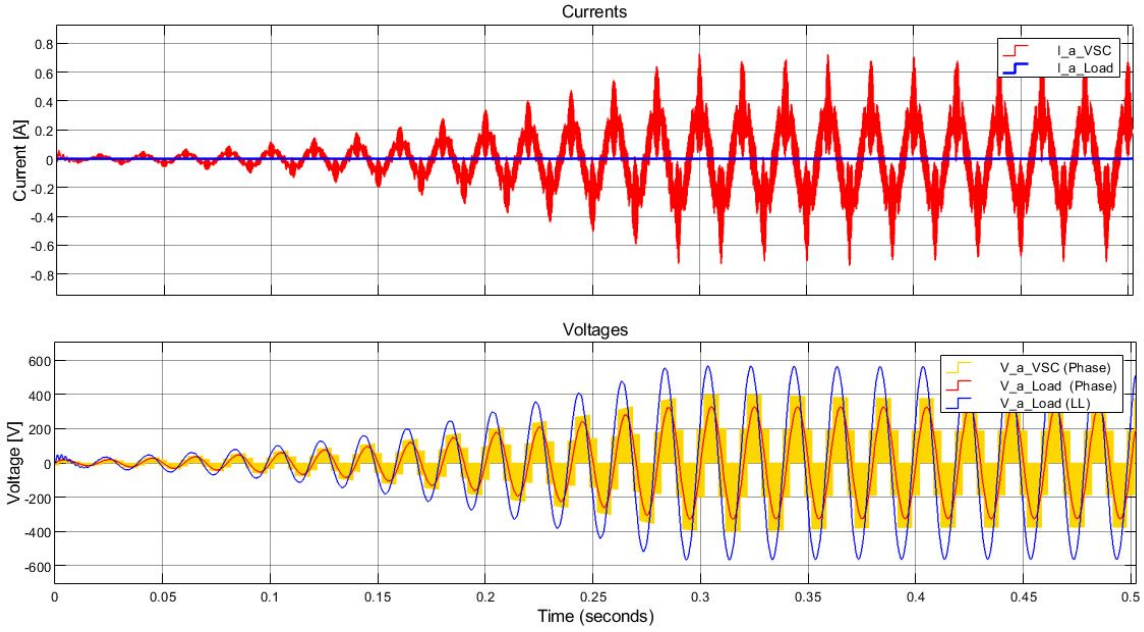

Figure 13.31: Oscillatory progress in current and voltages at load side during magnetization of #IM3 (3.0 kW) with an additional flywheel. (filtered and unfiltered)

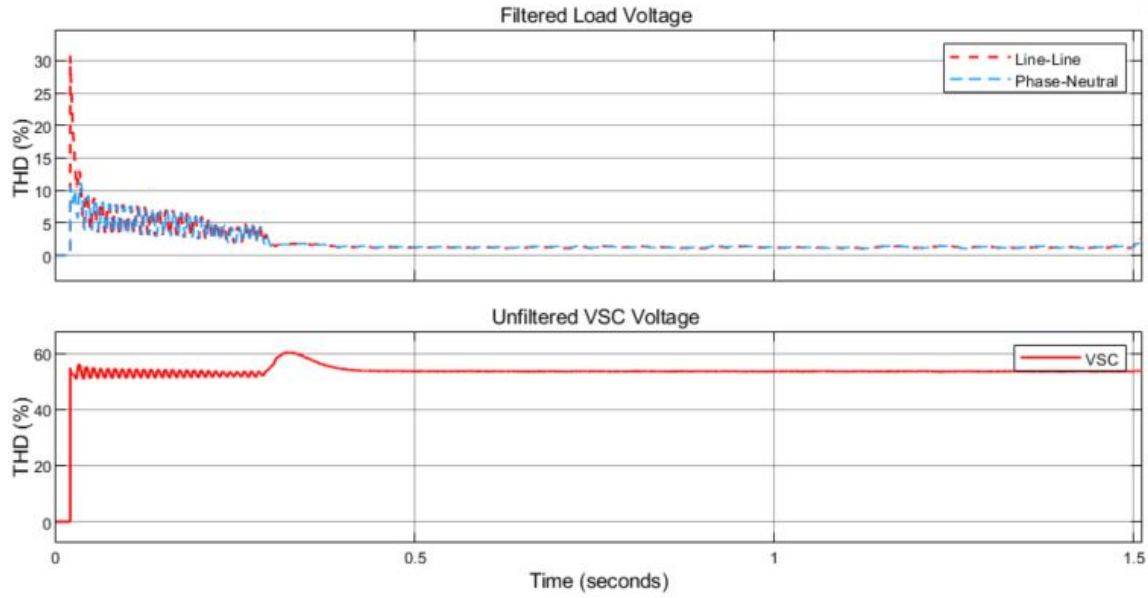

Figure 13.32: Total harmonic distortion (THD) in filtered load side voltages magnetization of #IM3 (3.0 kW) with an additional flywheel. The THD of the output voltage of load side VSC (unfiltered) is shown in the lower plot.

13.5.2 Step-Wise Increase form No-load to Full Load

The same step-by-step load profile as used in Test 3 is applied to the whole system when using #IM2, #IM3 and #IM3 with the flywheel of fivefolded moment of inertia (5 J_{tot}). The speed behaviors are seen in Table 13.14. They show that the AC-side behave similar for those loaded cases as long as the DC-link voltage is maintained. The LCL-filter performance seems in terms of load voltage quality to be good, and in the same ranges as for a stiff DC-link voltage. The DC-link ripple does not have any effect on the resulting load voltage quality. Figure 13.33 show the instantaneously current and voltages at the load side of the DC-link. The filtered voltages and current have a sinusoidal and smooth shape. How well the load RMS-voltage is kept constant is shown in Figure 13.34, the figure also show how the current increases in steps.

Table 13.14: Step-by-step increase of load demand from 0 and up to 1.5 kW for #IM2, #IM3 and #IM3 with a flywheel. IVC is used in the simulations, with $i_d = \frac{I_n}{2}$)

Loading 1 pu = 1.5 kW	**Step Time**	**Speed drop #IM2**	**Speed drop #IM3**	**Speed drop #IM3 + Flywheel**	**Drop in $V_{LL,Load}$**	**I_{Load} RMS**
0.20 pu	2.0 s	1364 rpm	1580 rpm*	1420 rpm	-1.02 %	0.43 A
0.35 pu	4.0 s	1106 rpm	1258 rpm	1346 rpm	-0.753 %	0.75 A
0.45 pu	6.0 s	1250 rpm	1353 rpm	1469 rpm	-0.25 %	0.97 A
0.55 pu	8.0 s	1188 rpm	1348 rpm	1433 rpm	-0.50 %	1.18 A
0.60 pu	10.0 s	1391 rpm	1459 rpm	1509 rpm	-0.25 %	1.29 A
0.65 pu	12.0 s	1376 rpm	1456 rpm	1498 rpm	-0.25 %	1.40 A
0.70 pu	14.0 s	1358 rpm	1454 rpm	1485 rpm	-0.25 %	1.51 A
0.75 pu	16.0 s	1288 rpm	1452 rpm	1497 rpm	-0.25 %	1.61 A
0.80 pu	18.0 s	1194 rpm	1447 rpm	1492 rpm	-0.25 %	1.72 A
0.85 pu	20.0 s	1118 rpm	1439 rpm	1488 rpm	-0.25 %	1.83 A
0.90 pu	22.0 s	1156 rpm	1431 rpm	1486 rpm	-0.25 %	1.94 A
0.95 pu	24.0 s	1200 rpm	1436 rpm	1482 rpm	-0.25 %	2.04 A
1.00 pu	26.0 s	1120 rpm	1422 rpm	1495 rpm	-0.25 %	2.15 A

*In the simulation the speed is still at the overshoot when step is applied.

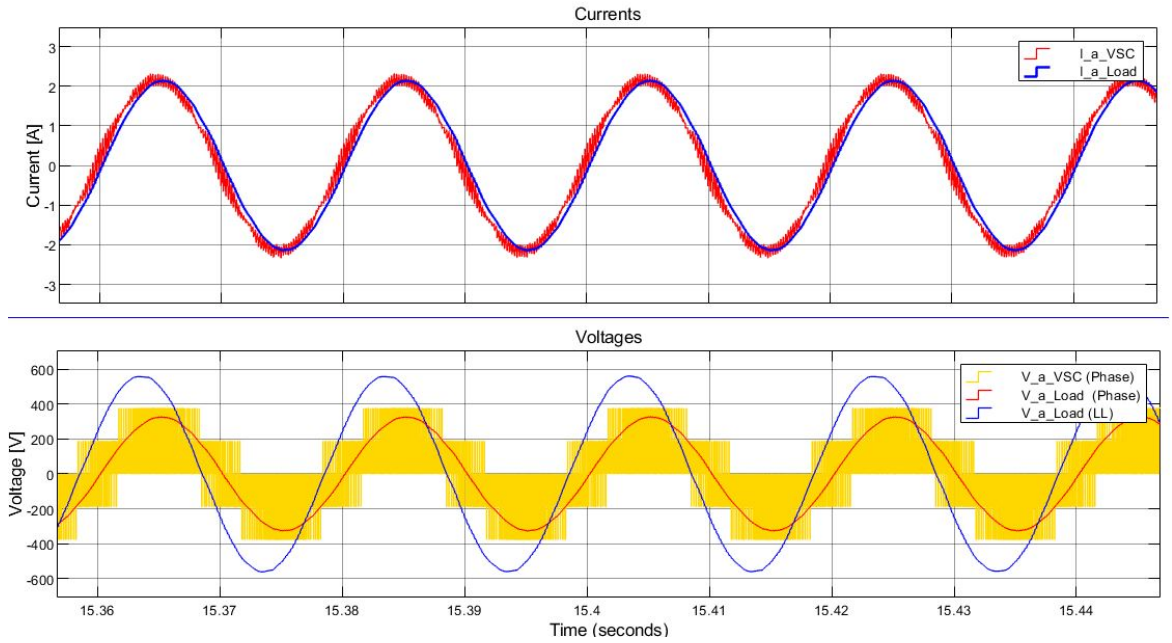

Figure 13.33: Instantaneous current and voltages in AC-grid at a loading of 0.70 pu. (1.05 kW).

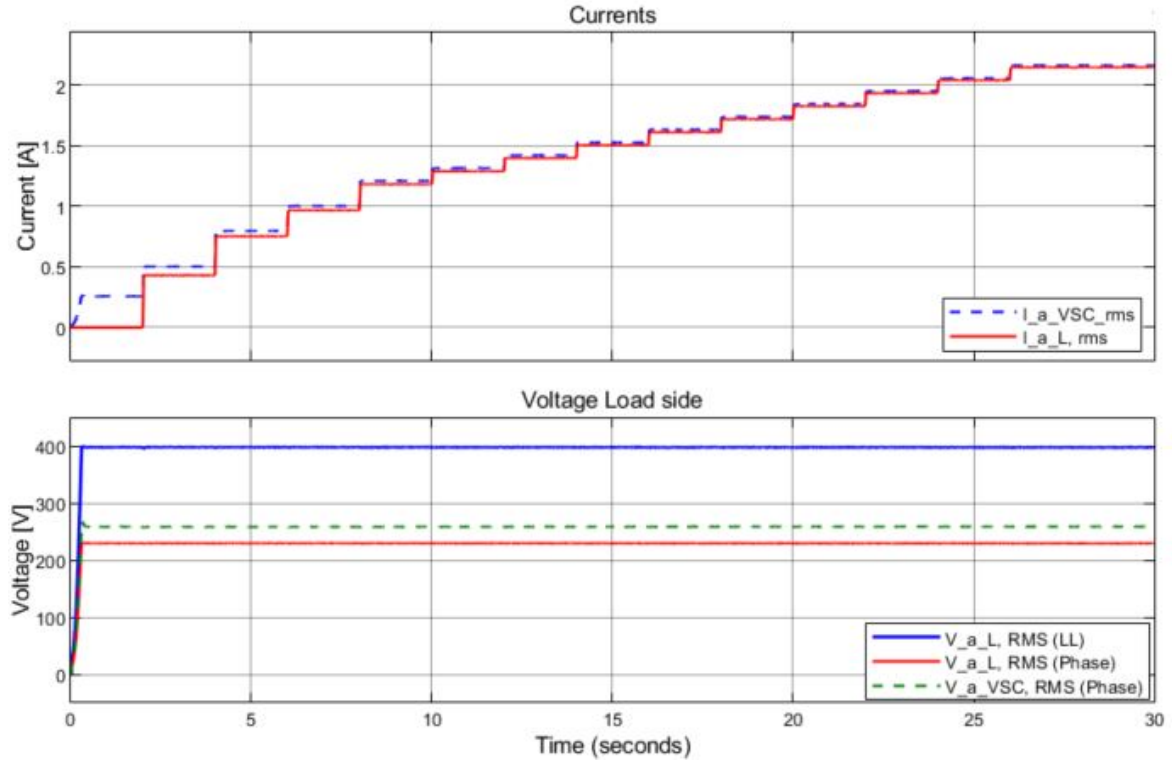

Figure 13.34: RMS - current and voltages at load side. Magnetization and load step of #IM3 (3.0 kW) with an additional flywheel. A voltage drop across the filter is observed. The load voltage is constant. The load steps are reflected by the steps in current.

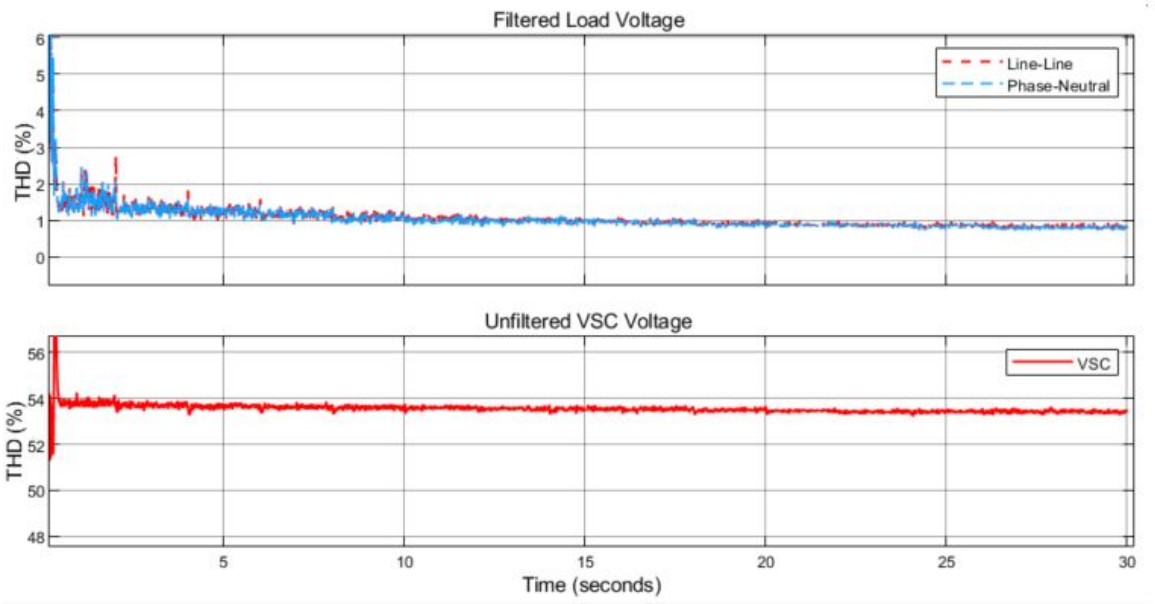

Figure 13.35: THD in the load voltage (filtered and unfiltered). Magnetization and load steps of #IM3 (3.0 kW) with an additional flywheel.

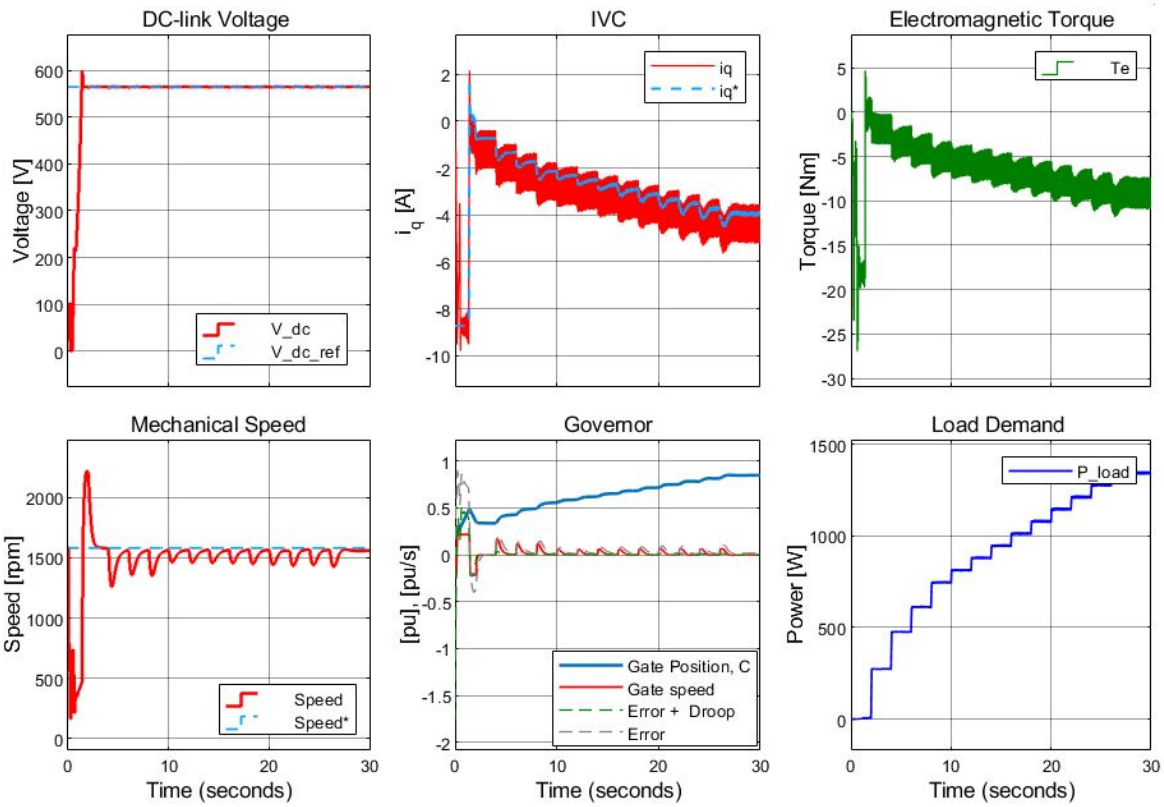

Figure 13.36: System behavior during step wise increase load increase of #IM3 (3.0 kW)

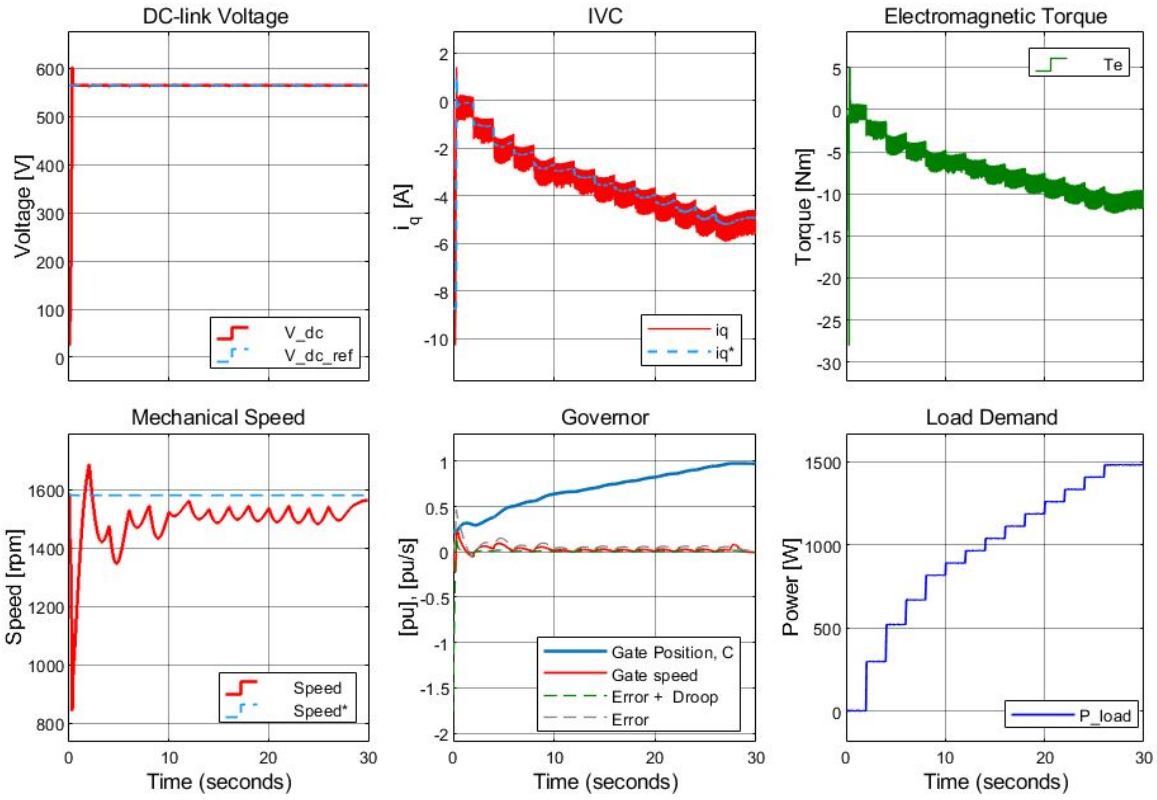

Figure 13.37: System behavior during step wise increase load increase of #IM3 (3.0 kW) with additional fywheel.

13.6 Recap and Conclusions from Simulations

Five different simulation tests have been performed to show some of the most important characteristics of the isolated system. In Test 1, the speed is held constant and it is found that the time needed to magnetize the generator and build up the DC-link voltage increases with the power ratings. The same yields when a 1.5 kW load step is applied, except for #IM1 which is unable to deliver the needed power when including stator losses. Further tuning of the V/f-control-parameters for the larger machines (i.e high rating) are needed to avoid the oscillatory behavior. The torque ripple is smaller in V/f-control than in IVC. IVC has a constant magnetizing current $i_d^* = \frac{I_n}{2}$. Fuzzy logic can be used to control i_d^* properly if both quick response and the efficiency at low loads are of significance.

The second test is also performed with constant speed to reveal the dependency of generator parameters and most importantly, the rotor time constant T_r. It is found that the rotor time constant has an effect on IVC, and too large deviations from the theoretical value can cause either a too low electromagnetic torque or even voltage collapse if T_r is too large.

Test 3 investigates how the system behaves during loaded conditions when including the turbine dynamics. The turbine rating is 2.2 kW and there are limitations in how fast the gate openings controlled by the governor of the turbine can change to achieve greater torque. In other words, the torque cannot change instantaneous but changes over time. When the mechanical torque and the electromagnetic torque are in imbalance, the speed changes. How large the change in speed becomes is mostly depending on the total moment of inertia. A step-by-step procedure to increase the load from 0 to 1.5 kW is done. The effect of an additional flywheel used to increase the moment of inertia is investigated. Increased moment of inertia will increase stability and hence the allowed load step sizes. In the end, another load profile was used. It showed that for #IM2 and #IM3 with no flywheel, the DC-link voltage will drop by up to 11.5 % for some of the step changes due to large speed drop. Hence, the q-component of current was not able to maintain the DC-link voltage. For #IM5, the speed does not drop so much and the machine could maintain the DC-link voltage. #IM5 has both larger moment of inertia and a larger current capability, which makes it better suited to avoid voltage drop in the DC-link. However, in many cases, the use of flywheel on #IM2 or #IM3 would have been a good solution to allow larger load steps. Better control of the magnetizing current, i_d, which in this simulation has been set constant to $\frac{I_n}{2}$, can also increase the allowed step size.

Test 4 was considering the characteristics of the inverter and passive filter connected to constant DC-source. Also here a step change of rated load was applied. Both at no load and at 1.5 kW loading, good performance was found. The requirements of $\leq \pm$ 3.0% deviation from the RMS reference rate 230 V and < 5.0% harmonic distortion (THD) used in Norwegian low voltage grids, are accommodated well at both no-load and at fully rated load. The THD is below 1.5 % for both cases and the AC-voltage is more or less constant at its RMS-reference ($\frac{400}{\sqrt{3}}$ V). A leakage current of 0.256 through the filter capacitor is seen. This additional current component lowers the filter efficiency, especially during no-load and low load conditions.

In Test 5, similar results in terms of load side voltage quality (THD and RMS) are found as achieved in Test 4. The load is changed in the same manner as done in Test 3. Any load rejection will lead to an overshoot in the speed in the same manner as expected in Test 3. The DC-link voltage ripple is of minor importance for the filtered load side voltage. This might change if the DC-link capacitor size is reduced. Too large speed deviations caused by large load steps will influence the DC-link voltage in terms of voltage drop or overshoot. This will propagate to the load side voltage and cause drops or overshoots in the load side voltage. An flywheel used to increase the inertia at a radius of 36.2 cm causes lower speed deviations for a given step change in the load. It will increase the total system

stability significantly. It is found that the load step could be larger if the loading before the step is low compared to the case where the loading before the step is relative high. This is since the available current capability is higher for the low loaded case than for the high loaded case.

The main recommendations based on the simulation results is to use a generator rated for more power than rated load. This is advantageous due to larger current capability and moment of inertia. Using a flywheel increase the allowed load step sizes.

What is not investigated in this thesis is how the power ratings of the turbine will influence the system's ability to handle such load steps load steps. It is expected that for a higher turbine, load steps (up to 1.5 kW) will be relatively smaller with respect to the turbine power rating and thus handled in a better way by the turbine generator set. All simulations assume balanced current conditions at generator and load side. Neither analysis of nor unbalanced conditions or fault behaviors (i.e short circuit) are investigated.

14 Conclusion

The topic of this Master's Thesis has been to study the control systems of an isolated induction generator driven by a hydro turbine. Obtaining a high voltage quality, even for a small scale hydro power plant, is the motivation of the task rather than economic aspects. The induction generator supplies a variable load through a filtered back-to-back converter topology. The maximal load demand is 1.5 kW. MATLAB/Simulink has been used as simulation environment and tool to build, initialize and simulate the system. The structures of the control systems have been shown and explained in detail. The tuning procedure used for the controller parameters that was in need of tuning are also given. This is done with the purpose of giving the reader full insight to how the control system and corresponding results are obtained. The reader should be able to redo the simulation tests based on the starting points and assumptions made throughout the work and obtain equal results.

During the simulation tests, the control methods of the generator, the generator power rating and the total moment of inertia are among the variables chosen. This choice is made in order to be able to make some recommendations to designers of isolated grid systems. These recommendations specify the best choices when selecting appropriate generator size (power rating) and associated control system. In this case, the maximum load demand is set to be 1.5 kW and the generator rating is varied in the range from 1.5 kW to 11 kW. It is found that a generator rating of 2.2 kW or 3.0 kW (#IM2 or #IM3) will be advantageous, preferably with an additional flywheel (radius = 36.2 cm). The flywheel is used to decrease the resulting speed deviation for a given load change. The speed deviation is reduced because of a larger total moment of inertia, J_{tot}, and larger machines will also contribute to increase the moment of inertia. #IM1 with power rating of 1.5 kW is not able to deliver maximum load power and compensate for the electrical losses while staying within the rated operation. A somewhat larger generator is recommended.

The turbine model is relatively simple and relies on several assumptions. It is implemented with the linear hydraulic transfer function with constant water starting time, T_w. T_w is based on assumptions of site conditions and the ratings of a 2.2 kW turgo turbine, estimated to be 0.175 s. This water starting time of 0.175 s is significantly lower than for most commercial hydro power plants. Thus, the turbine response is quicker than for operation of large hydro turbines in commercial hydro power plants. However, it is expected that a hydro turbine with low power rating will have a quicker response than the larger hydro turbine. Limitations in the gate changing speed at ± 0.216 pu/s are included to protect the turbine and achieve stability. The speed limit is larger than what is commonly used for commercial power plant, however the used limit is found to be suitable for such low turbine power ratings.

Both V/f-control and IVC seems to achieve high performance as the generator rotates at constant speed. The charge up time and settling time is a bit shorter for V/f-control than for IVC. For the IVC, the voltage overshoot is a bit lower than for V/f-control during charge up. The larger generators are able to produce the energy needed to charge the DC-link capacitor in a shorter time, this trend is reflected in the charge-up times. The DC-link voltage drops caused by a step change in the load, which is reduced when the generator rating is increased. It will also depend on the DC-link capacitor size, which is not varied in the analysis.

The main observations and conclusions from the analysis and simulation can be summarized as follows:

- The rating of the induction generator must be above maximum load (1.5 kW). Choosing the machines #IM2 or #IM3 at ratings of 2.2 kW and 3.0 kW, respectively, is recommended.

- #IM1 (with power rating 1.5 kW) cannot supply the load demand without being overloaded because of the stator losses. The DC-link voltage and thus also load voltage will decrease from their rated values.
- The scaling of the experimental per unit model gave a basis for comparing different power ratings of the machine.
- An additional flywheel on the shaft will increase the moment of inertia and thus allowing larger load steps in the system. To make the total moment of inertia five times greater for the turbine-generator set while using #IM3, a flywheel with a radius of 36.2 cm can be connected to the machine.
- If the mechanical speed drops below 900 rpm, the generator has difficulties with maintaining the DC-link voltage at the reference.
- For a constant DC-link voltage, the load voltage quality is very good: 230 V (± 0.15%) and a THD at ~1%, which both satisfy the Norwegian voltage quality requirements in [4].
- The tuning of V/f-control functions well for #IM2 and #IM3, but it needs some improvements for the generators with the highest power ratings.
- IVC is the favored control technique because of its simple control in the dq-domain. A drawback is the parameter dependency in terms of T_r.
- The ability to use fuzzy logic for optimized control of i_d^* is an advantage.
- It is chosen to keep i_d^* constant in the simulations to be able to quickly achieve a large electromagnetic torque when the load changes.
- V/f-control has less ripple in the resulting electromagnetic torque than IVC.

14.1 Suggestions for Further Work

In the work of this Master's Thesis some issued have been focused on while other issues still requires further research. Some of the suggestions for the further work are:

- To build a laboratory set-up of the whole system (i.e the model in Figure F.1) to make real measurements of the system. Comparing laboratory results with results from simulations
- Investigate the turbine rating influence on how the system handles larger load step changes
- Develop a control script in FPGA[6] or another suitable software tool that can be used to control the gates
- Further tuning the system parameters such that more of the non-linear limitations and *if/else* conditions becomes unnecessary in the control system. This will make an excellent control system if the stability is sufficient for all allowed operating states.
- Investigate any further improvement in the converters by using SV-PWM
- Further investigate how to reduce the flux current, i_d^* properly. This must be done to increase the efficiency of the induction generator at no-load and low-load.
- Include an evaluation of the economic aspects: The investment costs and maintenance costs will play an important role when designing the system. Thus, a more comprehensive cost-benefits analysis needs to be done.

[6]Acronym for Field Programmable Gate Array

- Investigate the filter performance when the load is either inductive or capacitive.
- Investigate how the system behaves during unbalanced current conditions.
- Investigate how the system will behave during short circuit conditions.

References

[1] Sondre Drevdal Borge.
B2B Converter-Based Control for Induction Generator Supplying Local Variable Loads. Masterthesis, Department for Electrical Power Engineering, NTNU, 2019.

[2] Aurora Andersson and Eirin Bye.
Analysis of Self-Excited Induction Generator for use in Rural Area with Electronic Load Controller and Additional Compensation Methods Master's thesis, Department of Electric Power Engineering: NTNU, 2016.

[3] Eivind Krakk
Voltage Controllers for Induction Machines in Isolated Operation Project Work, Department for Electrical Power Engineering, NTNU, 2019

[4] Lovdata
Forskrift om leveringskvalitet i kraftsystemet - § 3.1-3.10 - Kapittel 3. Krav til leveringspålitelighet og spenningskvalitet
https://lovdata.no/dokument/SF/forskrift/2004-11-30-1557 (12.05.2020)

[5] Prabha Kundur
Power System Stability and Control McGraw-Hill, Inc. Electric Power Research Institute, United States, 1994

[6] Mansor, Sa'ad
Behavior and Operation of Pumped Storage Hydro Plants University of Wales, Bangor, April 2000, Updated: August 2003.

[7] Bryan R. Cobb, Kendra V. Sharp
Impulse (Pelton and Turgo) turbine performance characteristis and their impact on pico hydro installations School of Mechanical, Industrial Manufacturing Engineering, 204 Rogers Hall, Oregon State University, Corvallis, USA, September 2012

[8] Jan Machowski, Janusz, W. Bialek, James R. Bumby
Power System Dynamics, Stability and Control John Wiley & Sons, Ltd, Second edition, 2008, reprinted 2012.

[9] P. Kundur, J.P. Bayne, P.L. Dandeno
Hydraulic Unit Dynamic Performance Under Normal and Islanding Conditions - Analysis and Validation IEEE Transactions on Power and Apparatus and Systems Toronto, Ontario Canada, Nov/Dec 1978.

[10] Working Group on Prime Mover and Energy Supply Models for System Dynamic Performance Studies
Hydraulic Turbine and Control Models for System Dynamic Studies Transactions on Power Systems, IEEE February 1992.

[11] D.G. Ramey and John W. Skooglund
Detailed Hydrogovernor Representation for System Stability Studies Transactions on Power Apparatus and Systems, IEEE, 1970.

[12] Suneco Turbines
SUNECO MICRO Hydro Turbines SINGLE NOZZLE, 2.2 KW HYDRO TURBINE
https://www.micro-hydro-power.com/Micro-Hydro-Turbine-Power-Single-Nozzle-XJ25-2DCT4-Z.htm (04.05.2020)

[13] Johan Björnstedt
Voltage and Frequency Control for Isolated Operated Induction Generators Department of Electrical Engineering and Automation, Lund University, 2007

[14] George McPherson, Robert D. Laramore
An introduction to Electrical Machines and Transformers. John Wiley and Sons, Second edition, 1990

[15] Jens G. Balchen, Trond Andresen and Bjarne A. Foss
Reguleringsteknikk Institutt for teknisk kybernetikk, NTNU, Trondheim, 2016, nytt opplag 2017.

[16] M. Godoy Simões and Felix A. Farret *Alternative Energy Systems Design and Analysis with Induction Generators* Second Edition Taylor & Francis Group, 2008

[17] Mohd. Faisal Khan, Mohd. Rizwan Khan
Analysis of Voltage Buildup and Speed Disturbance Ride Through Capability of a Self-Excited Induction Generator for Renewable Energy Application International Journal of Power and Energy Conversion, May 2016

[18] Tore M. Undeland, Ned Mohan, William P. Robbins
Power Electronics Converters, Applications and Design John Wiley & Sons, Ltd, 2003

[19] Hamid Ouadi, Fouad Giri, Luc Dugard.
Accounting For Magnetic Saturation in Induction Machines Modelling. International Journal of Modelling, Identification and Control, Inderscience, 2011, 14 (1/2), pp.27-36. 10.1504/IJMIC.2011.042337.hal-00406561

[20] A. E. Fitzgerald, Charles Kingsley Jr. Stephen D. Umans
Electric Machinery Chapter 6 Polyphase Induction Machines, Sixth Edition, Mc Graw Hill

[21] D. B. Kothari and I.J. Nagrath
Electric Machines McGraw Hill Education (India) Private Limited, Fourth Edition, 2010

[22] Roy Nilsen.
Electric Drives (*TET4120 Electric Drives Compendium*). Department for Electrical Power Engineering, NTNU, Spring 2018.

[23] John A. Holdsworth, Duncan A. Grant
The Use of Harmonic Distortion to increase the Output Voltage of a Three Phase PWM Inverter IEEE, Transaction On Industry Application, UK, 1984.

[24] A. Rezinik, M. Godoy Simones, Ahmed Al-Durra, S. M Muyeen
LCL Filter Design and Perfomance Analysis for Small Wind Turbine Systems Conference Paper July 2012

[25] G.K. Nisha, Z.V. Lakaparampil and S. Ushakumari
Effect of Leakage Inductance on Torque Controlled Capability of Field Oriented Controlled Induction Machine in Field Weakening region, International Conference on Advances in Engineering and Technology (ICAET'2014) March 29-30, 2014 Singapore

[26] Steven W. Smith
The Scientist and Engineer's Guide to Digital Signal Processing Moving Average Filters, Chapter 15. California Technical Publishing https://www.analog.com/media/en/technical-documentation/dsp-book/dsp_book_Ch15.pdf (09.05.2020)

[27] Jason Sylvestre
SPECTER ENGINEERING
https://www.specterengineering.com/blog/2019/9/7/dc-link-capacitor-selection-for-your-inverter (05.05.2020)

[28] Siemens
IEC Squirrel-Cage Motors Frame sizes 56 to 450. Power range 0.06 to 1250 kW, Catalog D 81.1, SIEMENS AG, 2008

[29] Chee-Mun Ong
Dynamic Simulations of Electric Machinery using MATLAB/simulink Prentice Hall PTR, A Simon Schuster Company, 1998

A Data and Parameters of the Machines

A.1 #IM1: 1.5 kW SCIM - Experimental Data

The data given on the machine card of #M1 is given in Table A.1[7]. The base operation conditions are set be 400 V (Y) and 50 Hz.

Table A.1: Data on the Machine card of #IM1 (1.5 kW)

V	Hz	rpm	kW	cos Φ	A
Δ 230	50	1420	1.50	0.81	6.00
Y 400	50	1420	1.50	0.81	3.45
Δ230	60	1720	1.75	0.82	6.00
Y 400	60	1720	1.75	0.82	3.35

Table A.2 shows the experimental results from DC-test and BR-test (blocked rotor test) from the laboratory work that was done Fall 2019 during the Project Work [3].

Table A.2: Experimental estimated parameters values of #IM1 and per unit values.

	R_s	R'_r	X_{ls}	X'_{lr}	L_{ls}	L'_{lr}
	5.56 Ω	3.90 Ω	3.76 Ω	5.64 Ω	12.0 mH	18.0 mH
Per Unit	0.0830	0.0599	0.0562	0.0843	0.0562	0.0843

A.2 #IM2 - #IM5: Ratings 2.2 kW - 11 kW

Table A.3 shows the given data of #IM2 - #IM5 in the Siemens Motor catalog [28]. A 1.5 kW induction machine found in [28] similar to #IM1 is used to verify the estimated nominal torque, moment of inertia and total mass. The values in Table A.3 are used in the Simulink model.

Table A.3: Machines #M1-#M5.

	P_{nom}	n	τ_{nom}	I_{nom}	cos ϕ	m	J_{gen}
#IM1	1.5 kW	1420 rpm	~10 Nm	3.45 A	0.81	~35 kg	~0.0035 kg/m^2
#IM2	2.2 kW	1420 rpm	15 Nm	5.1 A	0.80	44 kg	0.0048 kg/m^2
#IM3	3.0 kW	1415 rpm	20 Nm	6.6 A	0.82	47 kg	0.0058 kg/m^2
#IM4	5.5 kW	1450 rpm	36 Nm	11.1 A	0.83	76 kg	0.01 kg/m^2
#IM5	11 kW	1455 rpm	72 Nm	21.5 A	0.85	128 kg	0.04 kg/m^2

The lab measurement of #IM1 is used as a basis to determine the parameters of #IM2-#IM5. Table A.4 show the resulting parameters. Note the value of L_m in Table A.4 is the unsaturated (constant) magnetizing inductance used to calculate controller parameters (e.g. T_r in IVC). The magnetizing characteristic is saturated.

[7]The current flowing through the coils in Δ connection is reduced reduced by a factor $\sqrt{3}$ of the line current

Table A.4: Parameters for #M1-#M5

	P_{nom}	R_s	L_{ls}	R_r	L_{lr}	L_m	T_r
#IM1	1.5 kW	5.557 Ω	11.974 mH	3.901 Ω	17.960 mH	407.931 mH	0.109 s
#IM2	2.2 kW	3.759 Ω	8.100 mH	2.639 Ω	12.150 mH	280.6 mH	0.111 s
#IM3	3.0 kW	2.905 Ω	6.259 mH	2.039 Ω	9.388 mH	218.6 mH	0.112 s
#IM4	5.5 kW	1.727 Ω	3.722 mH	1.212 Ω	5.582 mH	131.4 mH	0.113 s
#IM5	11 kW	0.892 Ω	1.921 mH	0.626 Ω	2.882 mH	63.336 mH	0.114 s
Per unit (pu)	1.0	0.0830	0.0561	0.0527	0.0843	1.92	0.112 s

Table A.5 shows the relative size of the maximum load demand compared to the generator rating.

Table A.5: Rated load (P_{load} = 1.5 kW) in generator per unit for #M1-#M5

	$P_{nom,gen}$	$\frac{P_{nom,gen}}{P_{load}}$
#IM1	1.5 kW	1.00
#IM2	2.2 kW	0.68
#IM3	3.0 kW	0.50
#IM4	5.5 kW	0.27
#IM5	11 kW	0.13

A.3 Magnetizing characteristic of #IM1

Data from no-load test of #IM1 in motoring mode are given in Table A.6. Laboratory work done during the Project Work [3] Fall 2019. The data make up a basis for the per unit magnetization characteristic as discussed in Chapter 3.

Table A.6: Data from no-load test of #IM1 in motoring mode.

Slip	**Speed [rpm]**	$\mathbf{V_\Phi}$ **[V]**	$\mathbf{V_{LL}}$ **[V]**	**I [A]**	$\mathbf{P_{no-load}}$ **[W]**	$\mathbf{X_m}$ **[Ω]**
0,33 %	1495	100,3	173,7	0,694	17,2	144,52
0,07 %	1499	110,9	192,1	0,800	21,2	138,63
0,00 %	1500	120,4	208,5	0,867	23,1	138,87
0,07 %	1499	131,8	228,3	0,973	23,8	135,46
0,07 %	1499	140,8	243,9	1,044	28,7	134,87
0,07 %	1499	149,2	258,4	1,103	31,2	135,27
0,00 %	1500	160,5	278,0	1,239	32,3	129,54
0,07 %	1499	171,1	296,4	1,355	37,5	126,27
0,07 %	1499	180,1	311,9	1,438	40,5	125,24
0,07 %	1499	189,0	327,4	1,553	46,8	121,70
0,07 %	1499	200,1	346,6	1,737	48,0	115,20
0,00 %	1500	205,9	356,6	1,792	56,5	114,90
0,00 %	1500	210,4	364,4	1,892	54,5	111,21
-0,07 %	1501	215,4	373,1	1,980	58,5	108,79
0,00 %	1500	220,2	381,4	2,10	61,8	104,86
0,07 %	1499	226,1	391,6	2,27	69,9	99,60
0,00 %	1500	231,2	400,5	2,40	66,9	96,33
0,00 %	1500	235,7	408,2	2,58	73,9	91,36
0,07 %	1499	240,6	416,7	2,74	83,6	87,81
0,00 %	1500	245,2	424,7	2,93	91,7	83,69
0,00 %	1500	250,9	434,6	3,22	103,9	77,92
0,00 %	1500	254,6	441,0	3,45	106,9	73,80
0,07 %	1499	260,9	451,9	3,83	129,3	68,12

B Determination of Water Staring Time, T_w

The water starting time is an essential parameter for the dynamics in the model. When T_w is low, the response time to changes in the system become shorter. Thus the period where transient droop is needed after a sudden change in load is reduced. The water starting time, T_w is an important parameter for the dynamics of the turbine-generator set in the model.

In Table B.1 the rated data of a SUNECO- 2.2 kW turgo turbine are given [7]. These data are used a basis in order to determine the water staring time T_w for a turbine, that are suitable to be a part of the turbine-generator set that contains the IM.

Table B.1: Data for SUNECO - 2.2 kW turgo turbine [7]

Model	XJ25-2.2DCT4-Z
Output power, P_{turb}	2.2 kW
Rated head, H_{rated}	18-25 m
Rated flow, Q_{rated}	8-10 l/s
Efficiency, η_{turb}	70 %
Pipe diameter, d_{pipe}	125 mm

$$T_w = \frac{L}{A} \cdot \frac{Q_{base}}{g \cdot H_{base}} \tag{B.1}$$

The definition of the water starting time given equation 2.2 is repeated above as equation B.1. The rated data given in Table B.1 and the constants in Table B.2 are used to determine the water starting time, T_w by B.1.

Table B.2: Constants and assumption used to determine T_w

Acceleration due to gravity, g	9.81 m/s^2
Water density, ρ	1000 kg/m^3
Length of pipe, L	45 m

The cross-section area of the pipe, A is related to the diameter, d_{pipe} by:

$$A = 2\pi \cdot \left(\frac{d_{pipe}}{2}\right)^2 \tag{B.2}$$

By varying Q_{base} and H_{base} within the rated range given in Table B.1, the resulting values of water starting time T_w are given in Table B.3. It is seen that T_w lies within [0.120 s, 0.208 s]. The operation condition at a flow of Q = 9.6 l/s and at a head of H = 20.5 m is chosen as operation condition for the estimated water starting time used in this task. From Table B.3 it is seen that T_w = 0.175 s

Table B.3: Variety of T_w within rated condition of the 2.2 kW turgo turbine, with pipe length L=45m

Tw [s]	Flow, Q [l/s]																							
Head [m]	8	8,10	8,2	8,30	8,4	8,50	8,6	8,70	8,8	8,90	9	9,10	9,2	9,30	9,4	9,50	9,6	9,70	9,8	9,90	10
18	0,166	0,168	0,170	0,172	0,174	0,177	0,179	0,181	0,183	0,185	0,187	0,189	0,191	0,193	0,195	0,197	0,199	0,201	0,204	0,206	0,208
18,5	0,162	0,164	0,166	0,168	0,170	0,172	0,174	0,176	0,178	0,180	0,182	0,184	0,186	0,188	0,190	0,192	0,194	0,196	0,198	0,200	0,202
19	0,157	0,159	0,161	0,163	0,165	0,167	0,169	0,171	0,173	0,175	0,177	0,179	0,181	0,183	0,185	0,187	0,189	0,191	0,193	0,195	0,197
19,5	0,153	0,155	0,157	0,159	0,161	0,163	0,165	0,167	0,169	0,171	0,173	0,174	0,176	0,178	0,180	0,182	0,184	0,186	0,188	0,190	0,192
20	0,150	0,151	0,153	0,155	0,157	0,159	0,161	0,163	0,164	0,166	0,168	0,170	0,172	0,174	0,176	0,178	0,179	0,181	0,183	0,185	0,187
20,5	0,146	0,148	0,150	0,151	0,153	0,155	0,157	0,159	0,160	0,162	0,164	0,166	0,168	0,170	0,171	0,173	0,175	0,177	0,179	0,181	0,182
21	0,142	0,144	0,146	0,148	0,150	0,151	0,153	0,155	0,157	0,158	0,160	0,162	0,164	0,166	0,167	0,169	0,171	0,173	0,174	0,176	0,178
21,5	0,139	0,141	0,143	0,144	0,146	0,148	0,150	0,151	0,153	0,155	0,156	0,158	0,160	0,162	0,163	0,165	0,167	0,169	0,170	0,172	0,174
22	0,136	0,138	0,139	0,141	0,143	0,144	0,146	0,148	0,150	0,151	0,153	0,155	0,156	0,158	0,160	0,161	0,163	0,165	0,167	0,168	0,170
22,5	0,133	0,135	0,136	0,138	0,140	0,141	0,143	0,145	0,146	0,148	0,150	0,151	0,153	0,155	0,156	0,158	0,159	0,161	0,163	0,164	0,166
23	0,130	0,132	0,133	0,135	0,137	0,138	0,140	0,141	0,143	0,145	0,146	0,148	0,150	0,151	0,153	0,154	0,156	0,158	0,159	0,161	0,163
23,5	0,127	0,129	0,130	0,132	0,134	0,135	0,137	0,138	0,140	0,142	0,143	0,145	0,146	0,148	0,150	0,151	0,153	0,154	0,156	0,157	0,159
24	0,125	0,126	0,128	0,129	0,131	0,132	0,134	0,136	0,137	0,139	0,140	0,142	0,143	0,145	0,146	0,148	0,150	0,151	0,153	0,154	0,156
24,5	0,122	0,124	0,125	0,127	0,128	0,130	0,131	0,133	0,134	0,136	0,137	0,139	0,140	0,142	0,143	0,145	0,146	0,148	0,150	0,151	0,153
25	0,120	0,121	0,123	0,124	0,126	0,127	0,129	0,130	0,132	0,133	0,135	0,136	0,138	0,139	0,141	0,142	0,144	0,145	0,147	0,148	0,150

C Rotor Inertia and Flywheel Inertia

For most induction machines the moment of inertia of the rotor, J_{gen} can be found in the data sheet given by the manufacturer. If the data sheet for the actual machine is missing or the inertia is not given in data sheet, the moment of inertia similar machines at a the same power rating will give a good indication. This is done for #IM1. For #IM2 - #IM6 the moment of inertia are taken from the Siemens motor catalog [28].

The hydraulic turbine also have a moment of inertia, J_{turb}. Usually this is only a fraction of the generator inertia. This fraction is set to $\frac{1}{10}$:

$$J_{turb} = \frac{1}{10} \cdot J_{gen} \tag{C.1}$$

The total moment of inertia of the generator-turbine set, J_{tot} is:

$$J_{tot} = J_{gen} + J_{turb} \tag{C.2}$$

J_{tot} is used in the simulation without any additional flywheel on the shaft.

To increase the system stability with increased moment of inertia, an additional flywheel can be added to the shaft. Assuming a cylindrical shape on the flywheel containing iron with a density of ρ_{Fe} = 7.874 kg/dm^3 = 7874 kg/m^3. The height, h of the cylinder (i.e. thickness of the flywheel disc) is set 1 cm. The moment of inertia of a cylindrical shaped body spinning around its central axis is given by:

$$J_{tot} = \frac{1}{2} m \cdot r^2 \tag{C.3}$$

The mass, m of the flywheel can be found geometrically by:

$$m = \rho_{Fe} \cdot V = \rho_{Fe} \cdot (\pi r^2 h) \tag{C.4}$$

By insert equation C.3 into C.4 and re-arranging equation C.4, the radius of a flywheel with an given inertia J, is given by:

$$r = \sqrt[4]{\frac{2 \cdot J}{\pi \rho_{Fe} h}} \tag{C.5}$$

From C.5 the size (radius) of the flywheel needed to achieve sufficient stability of the turbine-generator set is found.

By insert the dimensions of a physical induction machine's rotor in equations C.3 and C.4, the generator inertia J_{gen} can be found. A quick estimate, shows that the geometry of #IM1 (obtained from project work) agrees with the moment of inertia in Table A.3 found from a similar machine in Siemens motor catalog [28]

D PID-Controllers

One important and widely used control technique in control systems, is the three-term *Proportional-Integral-Derivative (PID-)* control technique. For many purposes the adjustment and configuration of PID-controllers are easily preformed. Implementation of a PID-controller is nowadays usually done by computer based devices, although PID-functionality can also be implemented by mechanical, pneumatically or electrically arrangements [6]. Digital controllers allowing the control system to be more sensitive to small errors and provide fast action during transients. Figure D.1 shows a simple block diagram of a Simulink implementation of a PID-controller. The output $u(t)$ of the controller is the sum all three individual actions made on the error signal, $e(t)$. For some purposes it might be necessary to add unlinearities to the controller. These unlinearities could be limitations in the output signals or criteria for when some of the actions (I or D) is to be active or not.

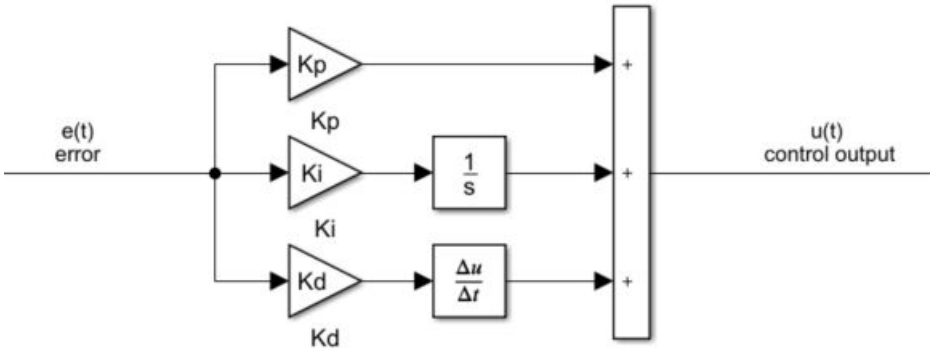

Figure D.1: Block diagram of PID-controller

Proportional gain, K_p produces as showed in equation D.1 a control signal, $u_p(t)$ proportional to the error $e(t)$ of the system. If a step change is applied to the set-point, a low value of K_p will give a stable transient response but the stationary deviation will be high. A higher gain will reduce (not eliminate) the stationary deviation, but it will also give a worse transient response, which resulting in lower system damping and thus stability.

$$u_p(t) = K_p \cdot e(t) \tag{D.1}$$

Integral gain, K_i is introduced to the controller to eliminate the stationary deviation produced by the proportional gain. As showed in equation D.2 the generated control signal $u_i(t)$ is proportional to the integral of error $e(t)$. With an error present the integrator increases the control action and drives the system to the demanded output. When the error disappear, the integral control output does not. It is used to maintain the control action needed for stationary conditions at desired output. Unfortunately the integrator introduces an extra 90° of phase lag to all frequencies. The 90° phase lag will increase the system settling time in addition to amplitude of all oscillations. Hence the integral action has an expense in terms of stability.

$$u_i(t) = K_i \int e(t)dt \tag{D.2}$$

The derivative gain, K_d can be added to reduce the oscillations and thus increase the stability. Equation D.3 shows that the control signal generated by the derivative action, $u_d(t)$ is proportional to the rate of change (derivative) of the error. The derivative action introduces an 90°-phase lead which increases the systems phase margin. Hence the damping of the system is increased. The increased damping allows higher values of K_p and K_i to be used compared to no derivative action in the controller. The stability of the system is increased. Since the error does not change during stationary conditions ($\frac{e(t)}{dt} = 0$), the derivative action does not affect the steady deviation and is therefore always used in conjunction with proportional and/or integral action.

$$u_d(t) = K_d \cdot \frac{e(t)}{dt} \tag{D.3}$$

In the s-domain the transfer function of the PID-controller depicted in Figure D.1 becomes:

$$G(s) = K_p + \frac{K_i}{s} + K_d s = (K_p s + K_i + K_d s^2) \cdot \frac{1}{s} \tag{D.4}$$

In some cases the PID-controller may be represented by K_p and:

- $T_i = \frac{K_p}{K_i}$ - Integral action time (reset time)
- $T_d = \frac{K_d}{K_p}$ - Derivative action time (rate time)

The transfer function of the PID-controller (D.4) can than be rewritten to the commonly used transfer function in D.5:

$$G(s) = K_p \left(1 + \frac{1}{sT_i} + sT_d\right) \tag{D.5}$$

E Three Phase-Model of an Induction Machine

Appendix E is (with a few modifications) cited from the project work [3] and included as an appendix in the Master Thesis because it outlines the mathematics used by Simulink in the Asynchronous Machine Block by the transformation from the three phase-domain to the dq0-domain. The transformation to the dq0-domain is also used in IVC.

This Appendix outlines the equations in the dq0-reference domain that the performance of the Simspace block Asynchronous Machine is based on. It is used to model the generator in the Simulink model. Both the stationary and synchronous reference frame can be used for simulations. In this case the synchronous (i.e. rotor flux) reference frame has been used in the modeling of the machines. In addition the vector control techniques uses dq0-modeling in the control. The outline is based on methodology from [29].

By using the principle of magnetic coupling (flux linkage) between any winding in the induction machine, the stator voltage equations in the abc-frame can be written as:

$$v_a^s = r_s i_a^s + \frac{d\lambda_a^s}{dt} \tag{E.1a}$$

$$v_b^s = r_s i_b^s + \frac{d\lambda_b^s}{dt} \tag{E.1b}$$

$$v_c^s = r_s i_c^s + \frac{d\lambda_c^s}{dt} \tag{E.1c}$$

Rotor voltage equations for a squirrel cage induction machine in abc-frame can be written as:

$$v_a^r = r_r i_a^r + \frac{d\lambda_a^r}{dt} = 0 \tag{E.2a}$$

$$v_b^s = r_r i_b^r + \frac{d\lambda_b^r}{dt} = 0 \tag{E.2b}$$

$$v_c^r = r_r i_c^r + \frac{d\lambda_c^r}{dt} = 0 \tag{E.2c}$$

Note that these rotor voltages are short circuited ($v^s = 0$) for SCIMs. The voltage equations uses the flux linkages given by the compact flux linkage equation (E.3) that can be written:

$$\begin{bmatrix} \lambda_{s,abc} \\ \lambda_{r,abc} \end{bmatrix} = \begin{bmatrix} \mathbf{L_{ss,abc}} & \mathbf{L_{sr,abc}} \\ \mathbf{L_{rs,abc}} & \mathbf{L_{rr,abc}} \end{bmatrix} \cdot \begin{bmatrix} \mathbf{i_{s,abc}} \\ \mathbf{i_{r,abc}} \end{bmatrix} \tag{E.3}$$

The submatrices for the stator to stator inductances and the rotor to rotor inductances are constant and given by:

$$\mathbf{L_{ss,abc}} = \begin{bmatrix} L_{ls} + L_{ss} & L_{sm} & L_{sm} \\ L_{sm} & L_{ls} + L_{ss} & L_{sm} \\ L_{sm} & L_{sm} & L_{ls} + L_{ss} \end{bmatrix} \tag{E.4}$$

$$\mathbf{L_{rr,abc}} = \begin{bmatrix} L_{lr} + L_{rr} & L_{rm} & L_{rm} \\ L_{rm} & L_{lr} + L_{rr} & L_{rm} \\ L_{rm} & L_{rm} & L_{lr} + L_{rr} \end{bmatrix} \tag{E.5}$$

The mutual inductance between stator to rotor "windings" and rotor to stator windings are dependent on the instantaneous rotor angle (θ_r):

$$\mathbf{L_{sr,abc}} = [\mathbf{L_{rs,abc}}]^{\mathbf{T}} = L_{sr} \cdot \begin{bmatrix} \cos\theta_r & \cos\theta_r + \frac{2\pi}{3} & \cos\theta_r - \frac{2\pi}{3} \\ \cos\theta_r - \frac{2\pi}{3} & \cos\theta_r & \cos\theta_r + \frac{2\pi}{3} \\ \cos\theta_r + \frac{2\pi}{3} & \cos\theta_r - \frac{2\pi}{3} & \cos\theta_r \end{bmatrix} \tag{E.6}$$

Where L_{ls} and L_{lr} are the leakage inductance from a stator or rotor windings respectively. L_{ss} and L_{rr} are the self inductances from each stator and rotor winding. L_{sm} and is mutual inductances between two stator windings and L_{rm} and is mutual inductances within the rotor. L_{sr} is the peak value of the mutual inductance between a stator winding and rotor. By neglecting the reluctive drops in the iron are neglected, these inductances can be expressed in terms of the winding turns N_s and N_r and the air gap permanance P_g. Equations E.1 and E.2 show that a three phase induction machine can be described by six first order differential equations. The mutual inductacnes between the winding couples them together Equation (E.3-E.6) [29].

E.1 Transformation to dq0-reference frame

A mathematical transformation from the three phase abc-reference frame into a $dq0$-reference frame is often used in studies of power systems and electrical machines. The purpose of a such transformation is to facilitate the solution of the system equations when some coefficients are time varying. Induction machines have position dependent mutual inductances between the stator windings and rotor given in Equation E.6. Since the machine is rotating the mutual inductances are also dependent on time. This makes $dq0$-transformations advantageous in order to facilitate the solution in applications such as designing control system for induction machines.

An arbitrary $dq0$-reference frame consist of two orthogonal and rotating axes (d and q), where the q-axis is said to lead the stator a-axis by an angle $\theta(t)$. Thus the arbitrary dq0-reference frame rotates at an angular speed $\omega(t)$. Likewise the rotor a-axis leads the stator a-axis by an angle $\theta_r(t)$ and rotates at a speed $\omega_r(t)$. Figure E.1 shows the stationary stator reference frame (abc_s), the rotor frame (abc_r) which rotates at an velocity $\omega_r(t)$ and the $dq0$-frame rotating at a velocity ω.

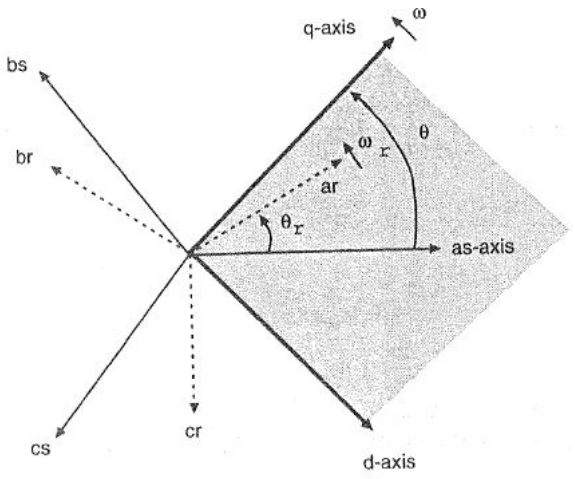

Figure E.1: An arbitrary $dq0$-reference frame rotating at a speed ω. Figure 6.4 in [29].

The transformation to the $dq0$ reference frame is mathematically done by multiplying the abc-quantities (i.e voltages or current) by the $dq0$-transformation matrix, $\mathbf{T_{dq0}}(\theta)$ defined in Equation E.7.

$$\begin{bmatrix} x_d \\ x_q \\ x_0 \end{bmatrix} = \frac{2}{3} \cdot \begin{bmatrix} \cos\theta & \cos\theta - \frac{2\pi}{3} & \cos\theta + \frac{2\pi}{3} \\ \sin\theta & \sin\theta - \frac{2\pi}{3} & \sin\theta + \frac{2\pi}{3} \\ \frac{1}{2} & \frac{1}{2} & \frac{1}{2} \end{bmatrix} \cdot \begin{bmatrix} x_a \\ x_b \\ x_c \end{bmatrix} \tag{E.7a}$$

$$\mathbf{x_{dq0}} = \mathbf{T_{dq0}}(\theta) \cdot \mathbf{x_{abc}} \tag{E.7b}$$

The 0-component in Equation E.7 is a zero sequence component, that can be considered as an dc-component that comes into significance during unsymmetrical conditions (i.e faults). Under symmetrical conditions the 0-component sums up to zero. It should also be noted that there are several other definitions of d- and q-axis orientations that are used in the literature. In most cases arbitrary rotating $dq0$-reference frames as given above is not used, instead it could be locked to one of the axis at stator, rotor or magnetic field. Different analysis favor different $dq0$-transformations: For an induction machine there are mainly two $dq0$-reference systems that stand out: The synchronous reference frame ($\omega = \omega_e$) and the stationary reference frame ($\omega = 0$, $\theta = 0$), which means that the q-axis is locked to stator a-axis. The first is often used for power system studies, induction machine loads along with other types of power system component, while the stationary frame is most used for transient studies of adjustable speed drives and their converters [29]. The stationary reference frame is often referred to as Clarke's transformation. For unbalanced conditions and discontinues in the induction machine performance, a rotor locked $dq0$-frame is often used.

E.2 Arbitrary dq0-domain

The $dq0$-transformations below transform Equations E.1 and E.2 into differential a set differential equations with constant inductances by using Equation E.7.

The stator voltage equations in an arbitrary $dq0$-domain becomes:

$$v_{qs} = r_s i_{qs} + \omega\lambda_{ds} + p\lambda_{qs} \tag{E.8a}$$

$$v_{ds} = r_s i_{ds} - \omega\lambda_{qs} + p\lambda_{ds} \tag{E.8b}$$

$$v_{0s} = r_s i_{0s} + p\lambda_{0s} \tag{E.8c}$$

Rotor voltage equations in an arbitrary dq0-domain:

$$v'_{qr} = r'_r i'_{qr} + (\omega - \omega_r)\lambda'_{dr} + p\lambda'_{qr} \tag{E.9a}$$

$$v'_{dr} = r'_r i'_{dr} - (\omega - \omega_r)\lambda'_{qr} + p\lambda'_{dr} \tag{E.9b}$$

$$v'_{0r} = r'_r i'_{0r} + p\lambda'_{0r} \tag{E.9c}$$

where the flux linkages are given by the time independent:

$$\begin{bmatrix} \lambda_{qs} \\ \lambda_{ds} \\ \lambda_{0s} \\ \lambda'_{qr} \\ \lambda'_{dr} \\ \lambda'_{0r} \end{bmatrix} = \begin{bmatrix} L_{ls} + L_m & 0 & 0 & L_m & 0 & 0 \\ 0 & L_{ls} + L_m & 0 & 0 & L_m & 0 \\ 0 & 0 & L_{ls} & 0 & & 0 \\ L_m & 0 & 0 & L'_{lr} + L_m & & 0 \\ 0 & L_m & 0 & 0 & L'_{lr} + L_m & 0 \\ 0 & 0 & 0 & 0 & & L'_{lr} \end{bmatrix} \cdot \begin{bmatrix} i_{qs} \\ i_{ds} \\ i_{0s} \\ i'_{qr} \\ i'_{dr} \\ i'_{0r} \end{bmatrix} \tag{E.10}$$

The electromagnetic torque is given by Equation E.11:

$$\tau_e = \frac{3}{2} \cdot p_p \cdot L_m(i'_{dr} i_{qs} - i'_{qr} i_{ds}) \tag{E.11}$$

E.3 Stationary dq0-domain

To get the system equations the stationary dq0-domain the system equations of an arbitrary dq0-domain in Equation E.1 and E.2 is obtained, by the dq0- transformation in Equation E.7. Then finally $\omega = 0$ is inserted to get the stationary domain equations:

Stator voltage equations in stationary dq0-domain:

$$v_{qs} = r_s i_{qs} + p\lambda_{qs} \tag{E.12a}$$
$$v_{ds} = r_s i_{ds} + p\lambda_{ds} \tag{E.12b}$$
$$v_{0s} = r_s i_{0s} + p\lambda_{0s} \tag{E.12c}$$

Rotor voltage equations in stationary dq0-domain:

$$v'_{qr} = r'_r i'_{qr} - \omega_r \lambda'_{dr} + p\lambda'_{qr} \tag{E.13a}$$
$$v'_{dr} = r'_r i'_{dr} + \omega_r \lambda'_{qr} + p\lambda'_{dr} \tag{E.13b}$$
$$v'_{0r} = r'_r i'_{0r} + p\lambda'_{0r} \tag{E.13c}$$

E.4 Rotor flux oriented dq0-domain

To get the system equations the rotor-flux $dq0$-domain the system equations of an arbitrary $dq0$-domain in Equation E.1 and E.2 is obtained, by the dq0- transformation in Equation E.7. Then finally $\omega = 0$ is inserted to get the rotor flux oriented dq0-domain:

Stator voltage equations in rotor flux oriented domain dq0-domain :

$$v_{qs} = r_s i_{qs} + \omega_e \lambda_{ds} + p\lambda_{qs} \tag{E.14a}$$
$$v_{ds} = r_s i_{ds} - \omega_e \lambda_{qs} + p\lambda_{ds} \tag{E.14b}$$
$$v_{0s} = r_s i_{0s} + p\lambda_{0s} \tag{E.14c}$$

Rotor voltage equations in rotor flux dq0-domain:

$$v'_{qr} = r'_r i'_{qr} + (\omega_e - \omega_r)\lambda'_{dr} + p\lambda'_{qr} \tag{E.15a}$$
$$v'_{dr} = r'_r i'_{dr} - (\omega_e - \omega_r)\lambda'_{qr} + p\lambda'_{dr} \tag{E.15b}$$
$$v'_{0r} = r'_r i'_{0r} + p\lambda'_{0r} \tag{E.15c}$$

F System Overview

F.1 Physical System

Figure F.1 shows an overview of how the the physical components are connected in the Simulink model. What components the control signals are acting on are also showed. The inner structures of the blocks are included in the chapters of the Master Thesis.

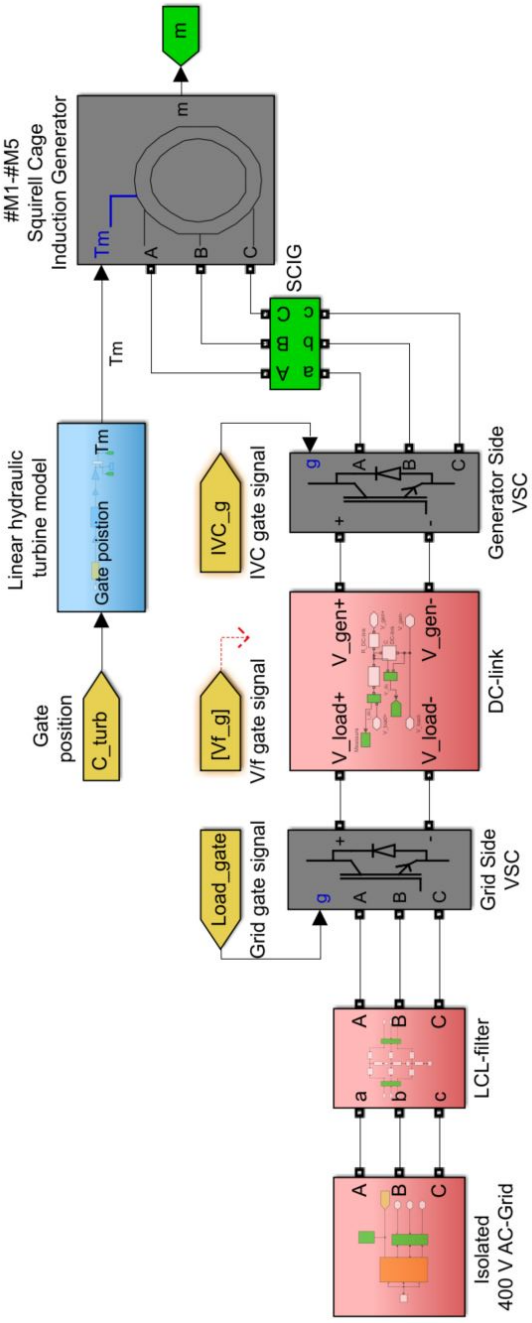

Figure F.1: Overview of model of the physical system and its components in Simulink

F.2 Control Systems

The governor for the hydraulic turbine, V/f-control and indirect vector control (IVC) to control the generator VSC and the Voltage controller for the grid side VSC are individual control systems. Either V/f-control or IVC are applied to the generator side VSC in a simulation.

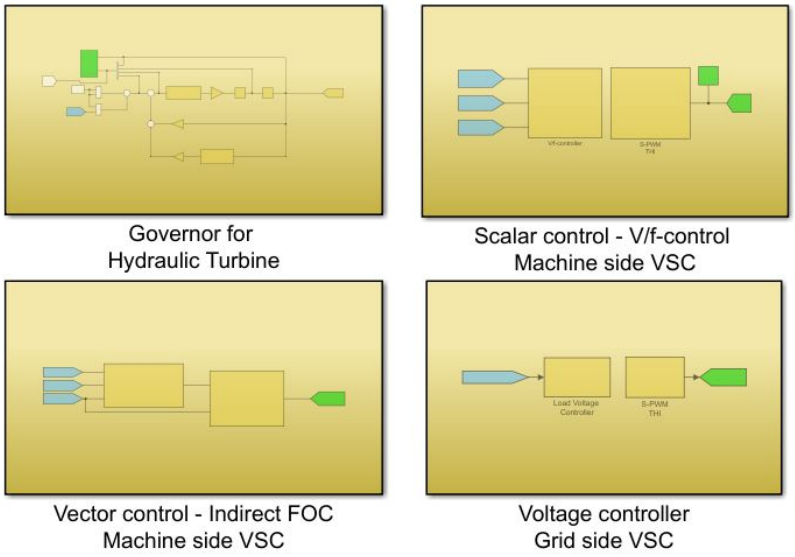

Figure F.2: Overview of the four different control systems used in this task

G MATLAB

This Appendix show the MATLAB functions of some design and control processes that are not fully covered in details in the Thesis. The design of the passive filter is a part of the initializing of the system. S-PWM and generation of gate signals are the functionality of the MATLAB-fucntion block showed in Figure 5.4.

G.1 Design of Passive LCL Filter

```
function [C, L1,L2, R]=filterLCL(Sn, f_grid, f_sw, V_dc_ref,
    V_grid)

%% Based on methodology from:
%  LCL-filter Design and Performance Aanalysis for Small Wind
    Turbine Systems,
%  A. Reznik M. G. Simoes, A. Al-Durra and S. M. Muyeen. (2012).

%% Fixed parameter
Sn=Sn*sqrt(2)/0.81;
x= 0.05; % Power factor variation seen from load.
Imax = Sn*sqrt(2)/(3*V_grid); % Maximum output current of the
    inverter
ka=0.2; % Desired attenuation ( nsket  dempning)

dI_L_max = 0.05*Imax; % Maximum current ripple at rated load

w_sw = 2*pi*f_sw;
w_grid = 2*pi*f_grid;

%% Base values:

En = sqrt(3)*V_grid;  % Line-line voltage (rms). Base voltage

Zb = En^2/Sn; % Base Impedance
Cb = 1/(w_grid*Zb);  % Base capcitance

%% Step 1 - L1
L1 =  V_dc_ref/(6*f_sw*2*dI_L_max);
%% Step 2 - C
C = x*Cb;
%% Step 3 - L2
r=0;
k_it =100;
count = 0;
delta_r = 1e-5;

while k_it > ka
    count = count+1;
    r = r+delta_r;
    k_it = 1/abs(1+r*(1-L1*C*w_sw^2));
```

```
end

L2 = r*L1;

%% Step 4 - w_res - Resonance frequency
w_res = sqrt((L1+L2)/(L1*L2*C));
f_res = w_res/(2*pi);
    if (f_res < (0.5*f_sw)) && (f_res >(10* f_grid))
        fprintf('Resonance in filter OK \n  \n');
    else
        fprintf('ERROR:  \n Resonance in filter NOT OK\n \n ');
    end
% Must satisfy 10*f_grid < f_res < 0.5 * f_sw

%% Step 5 - R
R = 1/(3*w_res*C);

end
```

G.2 S-PWM with 3^{rd}-Order Harmonic Injection

```
function [sin_w_a,sin_w_b,sin_w_c, t_out, w_out] = fcn(t,m, f,
    t_prev, w_prev)

t_out = t;
w_out = w_prev+(2*pi*f*(t-t_prev));

phi = 2*pi/3;

wa = w_out;
wb = w_out-phi;
wc = w_out+phi;

% To increase the utilization of the DC-voltage a third harmonic
    component
% is added to the reference signal. The third harmonic component
    is canceld
% in the line to line voltage.
sin_w_a=m*(2/sqrt(3))*(sin(wa)+(sin(3*wa)/6));
sin_w_b=m*(2/sqrt(3))*(sin(wb)+(sin(3*wb)/6));
sin_w_c=m*(2/sqrt(3))*(sin(wc)+(sin(3*wc)/6));
end
```

G.3 Generation of Gate Signals

```
function [au, al, bu,bl,cu,cl] = gateSignalGeneration(a_ref,b_ref,
    c_ref,tri)

if(a_ref >= tri)
    au = 1;
    al = 0;
else
```

```
7       au = 0;
8       al = 1;
9   end
10
11  if(b_ref >=  tri)
12      bu = 1;
13      bl = 0;
14  else
15      bu = 0;
16      bl = 1;
17  end
18
19  if(c_ref >= tri)
20      cu = 1;
21      cl = 0;
22  else
23      cu = 0;
24      cl = 1;
25  end
26
27  end
```

Eivind Krakk

Master's thesis

NTNU
Norwegian University of
Science and Technology